

Thermal stability investigations on Ag⁺ ion conducting superionic glasses and glass-ceramic nanocomposites

THESIS

Submitted in partial fulfillment of the requirements for the degree of

DOCTOR OF PHILOSOPHY

By

NEHA GUPTA

2007PHXF009P

Under the Supervision of

Dr. ANSHUMAN DALVI

Department of Physics



BIRLA INSTITUTE OF TECHNOLOGY & SCIENCE

PILANI (RAJASTHAN) INDIA

2012

Dedicated To
My Loving Family

CERTIFICATE

This is to certify that the research work in this thesis entitled “*Thermal stability investigations on Ag⁺ ion conducting superionic glasses and glass-ceramic nanocomposites*” being submitted by **Neha Gupta** in the Physics group, BITS, Pilani for the award of the degree of Doctor of Philosophy (Ph.D.), is a bonafide piece of research work carried out by her under my guidance and supervision and is fit to be considered for the award of the degree of Ph.D. No part of the thesis has ever been submitted in part or in full time to any other university or institution for the award of any other degree or diploma.

Date:

Supervisor

Dr. Anshuman Dalvi

Assistant Professor

Department of Physics,

BITS, Pilani,

Acknowledgements

Looking back, I am surprised and at the same time very grateful for all I have received throughout these years. It has certainly shaped me as a person and has led me where I am now. All these years of PhD studies were full of such gifts. It is true that it would not have been possible to write this doctoral thesis without the help and support of the kind people all around me, to only some of whom it is possible to give **particular** mention here. So, I thought I should add here

“THANK YOU, *to whom it concerns!!!*”

First and foremost I want to thank my supervisor **Dr. Anshuman Dalvi** for all the hope he has put on me, before I knew I could do any research at all. It has been an honor to be his first Ph.D. student. He has taught me, both consciously and unconsciously, how good experimental physics is done. I appreciate all his contributions of time, ideas, and funding to make my Ph.D. experience productive and stimulating. The joy and enthusiasm he has for his research was infectious and motivational for me, particularly during tough times in the Ph.D. pursuit. I am also thankful for the excellent example he has provided as a successful physicist and professor. I have heartfelt gratitude to Mrs. Swapna Dalvi and Sharva Dalvi for their love and care when I am far away from my home.

I would like to gratefully acknowledge Prof. Bijendra Nath Jain, vice chancellor of BITS Pilani, and Prof. L. K. Maheshwari, ex-vice chancellor for giving me the opportunity to join the institute. I also express my gratitude to Prof. G. Raghurama (Director, BITS Pilani), Prof. R.N. Saha (Deputy Director, Research & Educational Development and Administration, BITS Pilani) and Prof. G. Sundar (Deputy Director, Off Campus program, BITS Pilani) for providing necessary facilities in the institution.

I owe my deep gratitude to Prof. A. K. Das (Dean R & C) for providing me encouragement for the preparation of the work. I would like to thank Dr. S. N. Karbelkar, Head of Physics department, and my Doctoral Advisory Committee (DAC) members, Dr. Navin Singh and Dr. Debashis Bandyopadhyay for their support, insightful comments, and hard questions. Also, I wish to express my gratitude to all the faculty members in Physics department for their kind help time-to-time.

I convey my cordially gratitude to Dr. A.M. Awasthi, S. Bhardwaj and Dr. N. P. Lalla from UGC-DAE Consortium for Scientific Research, Indore (M.P.) and Dr. P. Senthil Kumar from Delhi University for their valuable help in the X-ray diffraction measurements and useful discussions. I am also grateful to Dr. V.P.S. Awana from National Physical Laboratory (NPL) for X-ray diffraction measurements.

I would like to thank Dr. D. Deva and Ms. Barkha Awasthi from DST unit on Nano Technology center, IIT Kanpur, for their precious help in SEM measurements.

It was my pleasure to meet Dr. K. Hariharan, and Dr. S. Chandra in the National conference on Solid State Ionics. I thank them and complete ionic community for effective suggestions and encouraging me during presentation of my work at various stages.

I would express my deep gratitude to Mr. Chhajuram and Mr. Vinod (central workshop) for helping me during the fabrication part of instruments in workshop. My genial thanks to Mr. Rajiv gaur and Mr. Shrikant Sharma for constant help at time.

My gratitude is also for Department of Science and Technology (DST) for funding my trip to Singapore to present my work in International conference on Materials for Advanced Technology (ICMAT).

I would also like to thank the many people who have taught me: my school teachers (especially Yasmin Jahaan), my graduate teachers (especially Dr. Vandana Gupta, Dr. V. K. Gupta), and Dr. A. K. Dutta, Dr. A. Mishra and Late Dr. Ashwin Kumar, my post graduate teachers for their kind assistance with giving wise advice and helping with various applications. I wish to express here my special thank to who helped me gave me time to time support and encouragement

I thank all research scholars of Physics department (*PHYTONS*): Siddheshwar Chopra, Rasmita Sahoo, Manish Kumar, Munendra Jain, Munesh Rathore, Vikas Sharma, Amar Singh, Sunita Joshi, C. Karthik, Kapil, Monika, Keerti, Jitendra, Ravi, Surendra and Tej for the stimulating discussions, and for all the fun we have had in the last four years.

At same time I would like to express my especial thanks to my friends Prashant Dabas (IIT, Madras), Anji Reddy Polu (Dr. H.S.G. University, Sagar, M.P.) for their fruitful discussions.

During this work, it was my pleasure to interact with M.Sc. project students in the Materials Physics Laboratory. I thank all of them specially S. Karthikeyan, Y. Srikanth, Mohan Krishna, Nitish Yadav, Bhaskar Mittal, Rajat Batra and Aparajita Singh for corporation and discussions.

Apart from that I wish to thank my friends Saurabh Parmar, Manmeet Kaur Dhaliwal, Taniya Mojumder, Shipra Singh and Garima Gupta for helping me get through the difficult times, and for all the emotional support, camaraderie, entertainment and care they provided.

I would like to thank my parents *Mrs. Usha* and *Mr. Ganpati Gupta* who through my childhood and study career had always encouraged me to follow my heart and inquisitive mind in any direction this took me. My parents provided me with a loving home, one where an academic mind was celebrated. Here I should mention my gratitude to my brothers Naman, Bhupendra Bhaiya, Abhishek Bhaiya, Brajesh Bhaiya and Pawan Bhaiya and my sister *Megha* for their exciting and strong support. If we ever had a family motto that would have been – *If there's a will, there's a way* – a philosophy of life I have been carrying with me every day. They have

given me their explicit support throughout, as always, for which my mere expression of thanks likewise does not suffice.

I deeply acknowledge the BITS, Pilani for the financial assistance throughout the PhD tenure.

Date:

Neha Gupta

ABSTRACT

Superionic glasses are the promising candidates as electrolytes for all-solid-state battery applications. Since glasses are thermally unstable due to crystallization, a systematic understanding of thermal properties is inevitable prior to any application. Somehow, thermal stability investigations on various glassy systems have got considerable attention only in last few years. Secondly, glass-ceramic nano composites obtained from glasses have also attracted the scientific community only recently due to their better stability and interesting electrical and structural properties. Thus a thorough investigation on thermal stability of superionic glasses is indeed essential and in view of this the present investigation is undertaken. A fundamental well known system Ag^+ ion conducting glassy superionic system $\text{AgI-Ag}_2\text{O-V}_2\text{O}_5$ is chosen to realize the applicability of different thermal stability formulations proposed by various workers, (e.g. crystallization kinetics using Kissinger, Matusita-sakka methods and glass transition kinetics using Moynihan formulation) using differential scanning calorimetry. Thus the parameters like activation energy of structural relaxation (E_s) at T_g and crystallization (E_c), enthalpy content (ΔH), Hruby coefficient (k_{gl}) could be obtained and their trend with composition is analyzed. Alternatively, some of these parameters could also be obtained by analyzing the carefully measured electrical conductivity-temperature cycles above the T_g and T_c at various (30-300K/h) heating rates. Thus, in the present work it is demonstrated that σ -T cycles, if used accurately and effectively, can be further developed as an alternative method to study the thermal stability of the glasses. The parameters have been systematically calculated and found to be exhibiting very interesting trends with the composition. Effect of (i) mixed cation i.e. CuI substitution in place of AgI (ii) mixed glass modifier Cu_2O in place of Ag_2O and (iii) mixed glass formers (MoO_3 in place of V_2O_5), on the thermal properties is thoroughly investigated. As a consequence of repeated heating and cooling or deliberate annealing of AgI-based glasses near crystallization temperature, glass-ceramic nanocomposites were obtained. These were also characterized by conductivity-temperature cycle, XRD, SEM and DSC. Interestingly, the glass-ceramic samples do exhibit high thermal stability and some of them even exhibit comparable ionic conductivity to those of AgI-based glasses of same composition. Further, found to be stable under battery conditions.

TABLE OF CONTENTS

	Page No.
<i>Certificate</i>	iii
<i>Acknowledgements</i>	iv
<i>Abstract</i>	vii
<i>List of Figures and Tables</i>	
<i>List of Abbreviations</i>	
Ch. 1 – INTRODUCTION	1 – 22
1.1 General	1
1.2 Classification of superionic conductors	4
1.2.1 Crystalline solids	4
1.2.2 Solid polymers	5
1.2.3 Superionic glasses	6
1.2.4 Superionic composites	9
1.3 Superionic glasses: an overview	11
1.4 Development of materials and applications	15
1.4.1 Novel method of preparation of superionic glasses	15
1.4.2 Applications of superionic glasses	16
1.5 Theoretical aspects	16
1.5.1 Models proposed for ionic motion in glasses	16
1.5.1.1 Cluster bypass model	17

1.5.1.2	Diffusion path model	18
1.5.1.3	Structural model	18
1.5.1.4	Dynamic structural model	19
1.6	Statement of the problem	20
1.7	The glassy system for the present study	21
Ch. 2	– Experimental techniques	23 – 43
2.1	Sample preparation	23
2.2	Structural studies	24
2.2.1	X-ray diffraction	24
2.2.2	Scanning electron microscopy	26
2.3	Thermal Analysis	27
2.3.1	Differential scanning calorimetry	27
2.4	Electrical characterization	37
2.4.1	Impedance spectroscopy	37
2.4.2	Electrical conductivity setup	40
2.5	Mobility measurements	41
2.6	Electrochemical cell characterization	42
Ch. 3	– CuI-AgI-Ag₂O-V₂O₅ System: Effect of mixed alkali	44 – 66
3.1	Structural investigations	44
3.1.1	X-ray diffraction	44

3.1.2 Scanning electron microscopy	47
3.2 Differential scanning calorimetry	48
3.2.1 Glass transition and crystallization kinetics	52
3.3 Electrical conductivity	57
3.4 Electrochemical cell characteristics	65
3.5 Conclusions	65
Ch. 4 – AgI-Ag₂O-Cu₂O-V₂O₅: Role of glass modifier variation	67 – 84
4.1 Structural investigations	67
4.1.1 X-ray diffraction	67
4.1.2 Scanning electron microscopy	70
4.2 Differential scanning calorimetry	72
4.2.1 Glass transition and crystallization kinetics	74
4.3 Electrical conductivity and ionic mobility	78
4.4 Electrochemical cell characteristics	83
4.5 Conclusions	84
Ch. 5 – AgI-Ag₂O-V₂O₅-MoO₃ system: Variation of glass former	85 – 98
5.1 Structural investigations	85
5.1.1 X-ray diffraction	85
5.1.2 Scanning electron microscopy	86
5.2 Differential scanning calorimetry	88

5.2.1	Glass transition and crystallization kinetics	90
5.3	Electrical conductivity	94
5.4	Electrochemical cell characteristics	96
5.5	Conclusions	97
Applied Aspect:		
Ch. 6 – A novel method developed during the work		99 – 106
6.1	The method	99
6.1.1	SISOVOMO system	99
6.1.2	CI-SISOVO system	104
6.2	Conclusions	106
Ch. 7 – SUMMARY AND CONCLUSIONS		107 – 112
7.1	Conclusions	107
7.2	Future scope	111
References		113-123
<i>List of Publications</i>		
<i>List of Presentations</i>		
<i>Biography of the Supervisor</i>		
<i>Biography of the Candidate</i>		

LIST OF FIGURES AND TABLES

List of Figures:	Page No.
Fig. 1.1 Ionic conductivity in AgI and PbF ₂ (Hull, 2004)	2
Fig. 1.2 Unit cell of AgI and PbF ₂	3
Fig.1.3: Cluster by pass model explanation	17
Fig.1.4: Schematic of diffusion path model (after Minami, 1985)	17
Fig.1.5: Ionic transport with structural model	19
Fig.1.6: Dynamic structural model explanation	19
Fig. 2.1a: Diffraction from multiple planes of a crystal	24
Fig. 2.1b: Extended view of x-ray diffraction peak.	24
Fig. 2.2: Schematic diagram of a typical scanning electron microscope	26
Fig. 2.3: Schematic diagram of a typical differential scanning calorimeter	28
Fig. 2.4: A typical differential scanning calorimeter scan for glassy sample	28
Fig. 2.5: A crystallization peak in a DSC curve at extended scale	28
Fig. 2.6: Schematic diagram of electrical conductivity measurement setup (300K-1000K)	40
Fig. 2.7: Sample holder for electrical conductivity measurement (293K-500K)	41
Fig. 2.8: set up for mobility measurement. Where r.k. is the reversing key, pA is Keithley electrometer interfaced with computer.	42
Fig. 2.9: Schematic presentation of electrochemical cell characterization set up	43
Fig.3.1: X-ray diffraction patterns for as prepared glasses (a and d), glassy samples annealed at 140 ⁰ C (b and e), and at 170 ⁰ C (c and f). Symbols denote	45

(○) $\text{Ag}_8\text{I}_4\text{V}_2\text{O}_7$ (●) AgI (▲) $\text{Ag}_4\text{V}_2\text{O}_7$ peaks.	
Fig.3.2: X-ray diffraction patterns for glass ceramic samples obtained at various crystallization temperatures. Symbols denote (○) $\text{Ag}_8\text{I}_4\text{V}_2\text{O}_7$ (●) AgI (★) $\text{Ag}_4\text{V}_2\text{O}_7$ peaks	46
Fig: 3.3: Scanning electron microscopy images for 30CI-SISOVO (a) as prepared glasses, samples annealed at (b) 90°C (T_{c1}), (c) 140°C (T_{c2}) and (d) 170°C (T_{c3}).	47
Fig. 3.4: DSC scans for different compositions of CI-SISOVO (I st) glassy and (II nd) annealed glassy samples.	49
Fig. 3.5: DSC scans at various heating rates for 10CI-SISOVO sample. T_{p1} , T_{p2} and T_{p3} correspond to major precipitation of AgI, $\text{Ag}_4\text{V}_2\text{O}_7$ and $\text{Ag}_8\text{I}_4\text{V}_2\text{O}_7$, respectively	51
Fig. 3.6: DSC scans at various heating rates for 30CI-SISOVO sample. The peaks correspond to T_{p1} : AgI, T_{p2} : $\text{Ag}_4\text{V}_2\text{O}_7$ and T_{p3} : $\text{Ag}_8\text{I}_4\text{V}_2\text{O}_7$	51
Fig. 3.7: $\ln q$ versus inverse of temperature for 10 and 30CI-SISOVO.	52
Fig. 3.8: The activation energy for structural relaxation at T_g as a function of CuI content in CI-SOSOVO	52
Fig.3.9: Modified Kissinger plot for (a) 10CI-SISOVO sample and (b) 30CI-SISOVO sample	53
Fig.3.10: The E_c values (obtained from Eq. (2)) as a function of CuI content	54
Fig. 3.11: $\ln(-\ln(1-\alpha))$ versus $\ln q$ for 10CI-SISOVO sample for the crystallization of $\text{Ag}_4\text{V}_2\text{O}_7$	55
Fig. 3.12: Electrical conductivity as a function of temperature at a typical heating rate of $1^\circ\text{C}/\text{min}$. Symbols denote: (●) first and (○) second heating cycles	58
Fig. 3.13: Electrical conductivity - temperature plot on an extended scale. Conductivity at peak (σ_p), after crystallization (σ_{XL}) and extrapolated at peak temperature (σ_{exp}) are shown for 50 SISOVO, 10CI-SISOVO and 15CI-SISOVO samples	59
Fig. 3.14a Crystallite by pass model to understand the conductivity behavior during crystallization (for nucleation dominated crystallization process)	60
Fig. 3.14b Crystallite by pass model to understand the conductivity behavior during crystallization (for growth dominated crystallization process)	60

Fig. 3.15: Electrical conductivity at 300K (a) and activation energy ($T \leq T_g$) (b) as a function of CuI content. Symbols denote: room temperature conductivity (●) before I st heating cycle and (○) after I st heating cycle; (▲) activation energy measured during I st heating cycle; (Δ) for II nd heating cycle	62
Fig. 3.16: (a) Transient current versus time plot on an extended scale for 30CI-SISOVO sample (b) d^2 versus $V\tau$ plot for 10 and 30 CI-SISOVO samples	64
Fig. 3.17: Ionic Mobility as a function of CuI content in the samples	64
Fig. 3.18: Constant load characteristics for external loads for Ag/I ₂ electrochemical cells with 30 CI-SISOVO glass-ceramic sample as electrolyte	65
Fig.4.1: X-ray diffraction patterns for as prepared glasses (a and d), glass ceramics (b, c). Symbol denote (●) AgI (○) Ag ₄ V ₂ O ₇ and (☆) Ag ₈ I ₄ V ₂ O ₇	68
Fig.4.2: X-ray diffraction patterns for 20 SICOSOVO, (a) as prepared and glass ceramics obtained after annealed at (b) 100 °C and (c) 170 °C. Symbol denote (●) AgI and (○) Ag ₈ I ₄ V ₂ O ₇	69
Fig. 4.3: Scanning electron microscopy scans for 10SICOSOVO (a) glass and glass-ceramics annealed at (b) 100 ⁰ C (c) 170 ⁰ C and 30SICOSOVO (d) glass and (e) annealed at 140 ⁰ C	71
Fig. 4.4: DSC scans for different compositions of SICOSOVO glassy samples (a and b) and glass ceramic samples (c and d).	72
Fig. 4.5: DSC scans at various heating rates for 10SICOSOVO sample. T _{p1} , T _{p2} and T _{p3} correspond to major precipitation of AgI, Ag ₄ V ₂ O ₇ and Ag ₈ I ₄ V ₂ O ₇ , respectively.	74
Fig. 4.6: DSC scans at various heating rates for 20SIOSOVO sample	74
Fig. 4.7: ln q versus inverse of temperature for 10, 20 and 30 SICOSOVO	75
Fig. 4.8: The activation energy for structural relaxation at T _g as a function of Cu ₂ O content in SICOSOVO	75
Fig. 4.9: Modified Kissinger plot for 10, 15, 20 and 30 SICOSOVO samples corresponding to precipitation of AgI	76
Fig. 4.10: The E _c values as a function of Cu ₂ O content	76
Fig. 4.11: DSC scans at various heating rates for 50AgI-27.5Ag ₂ O-22.5V ₂ O ₅ sample	78
Fig. 4.12: The activation energy for structural relaxation as a function of Ag ₂ O	78

content in AgI-Ag ₂ O-V ₂ O ₅ system	
Fig. 4.13 (a) Electrical conductivity as a function of Cu ₂ O content at room temperature. (b) Activation energy as a function of Cu ₂ O content	79
Fig. 4.14: Electrical conductivity as a function of inverse of temperature for (a) 10SICOSOVO, (b) 20SICOSOVO and (C) 30SICOSOVO samples. Symbols: (●) glassy samples and (○) glass-ceramic samples.	80
Fig. 4.15: (a) Transient current versus time plot on an extended scale for 30SICOSOVO sample. (b) Ionic Mobility as a function of Cu ₂ O content in the samples	82
Fig. 4.16: Constant load characteristics for external loads for Ag/I ₂ electrochemical cells with 30SICOSOVO sample as electrolyte	83
Fig. 5.1: The XRD patterns for 30SISOVOMO sample (a) as prepared glass and (b) glass-ceramic composites. Symbols denote: (○)Ag ₈ I ₄ V ₂ O ₇ and (●) Ag ₄ V ₂ O ₇	86
Fig. 5.2: The XRD patterns for 15SISOVOMO sample (a) as prepared glass and (b) glass-ceramic composites. 25SISOVOMO sample (c) as prepared glass and (d) glass-ceramic composites. Symbols denote: (○)Ag ₈ I ₄ V ₂ O ₇ and (●) Ag ₄ V ₂ O ₇	86
Fig. 5.3: SEM results for glassy and glass ceramic samples for 10 (a and b) and 30 (c and d) SISOVOMO	87
Fig. 5.4: DSC scans at a heating rate of 10 ⁰ C/min for the glassy system 50 AgI- 33.33Ag ₂ O-16.67[(V ₂ O ₅) _{1-x} -(MoO ₃) _x] (x = 0.1-0.3)	88
Fig. 5.5a: DSC scans for 30SISOVOMO at the various heating rates, viz. 5, 10, 15 and 20 ⁰ C/min	90
Fig. 5.5b: DSC scans for 10SISOVOMO at the various heating rates, viz. 5, 10, 15 and 20 ⁰ C/min	90
Fig. 5.6: Moynihan plots for 10, 20 and 30 SISOVOMO samples	91
Fig. 5.7: The E _s values (obtained from Moynihan plots) as a function of MoO ₃ content	91
Fig.5.8: ln{-ln(1-α)} versus ln q plots for 10, 20 and 30 SISOVOMO for T=106 ⁰ C	92
Fig. 5.9: Order parameter (n) with MoO ₃ content	92
Fig. 5.10: Modified Kissinger plot for 10, 20 and 30 SISOVOMO	93

Fig. 5.11: The E_c values obtained from Modified Kissinger Equation as a function of MoO_3	93
Fig. 5.12: Electrical conductivity versus inverse of temperature for various compositions at a heating rate of $1^\circ\text{C}/\text{min}$. The conductivity at peak and after crystallization are shown as σ_c and σ_{XL} , respectively for one of compound. Symbols denote (●) First cycle and (○) second cycle	95
Fig. 5.13: The electrical conductivity (at 333K) and activation energy for second heating cycle as a function of MoO_3 content	96
Fig. 5.14: Constant load characteristics for external loads for Ag/I_2 electrochemical cells with 30SISOVOMO sample as electrolyte	97
Fig. 6.1: DSC plots and conductivity versus temperature cycles at a typical heating rate of $5^\circ\text{C}/\text{min}$ for 10, 20 and 30 SISOVOMO	100
Fig. 6.2: Electrical conductivity versus inverse of temperature at various heating rates 0.5, 1, 3, 5 and 7 K/min for 20 SISOVOMO. The dotted line joins conductivity peak positions that shift towards higher temperatures	101
Fig. 6.3: Derivative of σ - $1/T$ cycles for the determination of the peak temperature (T_p). Inset: Electrical conductivity vs inverse temperature on an extended scale in the range $T_{sat} \geq T \geq T_c$	102
Fig. 6.4: (a) Electrical conductivity vs inverse temperature on an extended scale in the range $T_{sat} \geq T \geq T_c$ (b) Derivative of σ - $1/T$ cycles for the determination of the peak temperature (T_p) at various heating rates for 20SISOVOMO	102
Fig. 6.5: Moynihan (a) and Kissinger (b) plots for 20 SISOVOMO obtained from σ - T cycles	103
Fig. 6.6: Electrical conductivity versus inverse of temperature at various heating rates 0.5, 1, 3, 5 and 7 K/min for 10 CI-SISOVO. The dotted line joins conductivity peak positions that shift towards higher temperatures	104
Fig.6.7: Derivative of σ - $1/T$ cycles for the determination of the peak temperature (T_p) at various heating rates for 10 CI-SISOVO	105
Fig. 6.8: Moynihan (a) and Kissinger (b) plots for 10 CI-SISOVO obtained from σ - T cycles	106

List of Tables:	Page No.
Table 1.1: Differentiation between categories of superionic crystalline solids	5
Table 1.2: some synthesized polymer based electrolytes compositions which exhibit maximum conductivity	6
Table 1.3: Some Ag ⁺ ion conducting superionic oxide glasses with their conductivity (at 300K) and activation energies	8
Table 1.4: Some examples of different types of superionic composites	10
Table 1.5: Some examples of mixed glass formers, mixed alkali and mixed cation effects	12
Table 1.6: Description of some electrolytes with their open circuit voltage and cell type	16
Table 2.1: Impedance plots corresponding to different combination of resistance and capacitor	39
Table 3.1: Characteristics temperatures and total enthalpy release during crystallization in the CI-SISOVO system	50
Table 3.2: The Avrami parameter calculated by Augis - Bennett relation at various rates as a function of CuI content (5-20 °C/min) for the crystallization of three different compounds viz., AgI, Ag ₄ V ₂ O ₇ and Ag ₈ I ₄ V ₂ O ₇	56
Table 3.3: The Avrami parameter calculated by Matusita Sakka equation as a function of temperature	56
Table 4.1: Thermal stability parameters as a function of Cu ₂ O content	73
Table 4.2: The Avrami parameter calculated by Augis - Bennett relation at various rates as a function of CuI content (5-20 °C/min) for the crystallization of three different compounds viz., AgI, Ag ₄ V ₂ O ₇ and Ag ₈ I ₄ V ₂ O ₇	77
Table 5.1: Characteristics temperatures, total enthalpy release during the crystallization and E _s and E _c values obtained from Moynihan and modified Kissinger equation, respectively, in the SISOVOMO system	89
Table 6.1: Different thermal parameters obtained from Differential scanning calorimetry and conductivity-temperature cycles with MoO ₃ content	104
Table 6.2: Different thermal parameters obtained from Differential scanning calorimetry and conductivity-temperature cycles with CuI content	106
Table 7.1: Summary of thermal stability parameters and conductivity for best conducting glassy and glass-ceramic samples out of three chosen system	108

LIST OF ABBREVIATIONS

SIC	Superionic conductor
SPE	Solid polymer electrolyte
PEO	Polyethylene oxide
σ	Conductivity
SISOVO	AgI-Ag ₂ O-V ₂ O ₅
CI-SISOVO	CuI-AgI-Ag ₂ O-V ₂ O ₅
SICOSOVO	AgI-Cu ₂ O- Ag ₂ O-V ₂ O ₅
SISOVOMO	AgI-Ag ₂ O-V ₂ O ₅ -MoO ₃
DSC	Differential scanning calorimetry
SEM	Scanning electron microscopy
T _g	Glass transition temperature
T _p	Peak temperature
T _c	Crystallization temperature
T _m	Melting temperature
Q	Heating rate
R	Gas constant
E _c	Activation energy for crystallization
E _s	Activation energy for structural relaxation
ΔH	Enthalpy change
ΔS	Entropy change
n	Order parameter
μ	Mobility
T	Relaxation time
T _{rg}	Kauzman temperature
k _{gl}	Hruby constant

CHAPTER 1

INTRODUCTION

1.1 General

Ionic conduction in solids has attracted the scientific community as early as the beginning of 19th century, with the discovery of PbF_2 and Ag_2S compounds by Faraday (1839). The former (PbF_2) is found to be a F^- ion conductor and the latter one (viz., Ag_2S) exhibited Ag^+ ion conduction as later confirmed by various methods. If one examines the conductivity- temperature behavior of PbF_2 , it is observed that there is a gradual increase in the ionic conductivity with temperature on further heating till $T_c \sim 700^\circ\text{C}$. Above this temperature the conductivity reaches a value $\sim 4 \Omega^{-1}\text{cm}^{-1}$ and exhibits no appreciable change till 1158°C (a temperature close to melting point) (Benz, 1975; Derrington, 1973). It was further realized that the high ionic conductivity in PbF_2 is mainly due to anion diffusion in the fluorite structure. The principal defects at lower temperature ($T < T_c$) are the anion Frenkel defects and the interstitial position (cube center sites), but at the temperature $T \geq T_c$ (in $\beta\text{-PbF}_2$) the ion conduction is dominated by Frenkel disorder accompanied by creation of new vacant sites available for anion motion (Gillan, 1979).

After a gap of almost 90 years, anomalous ionic conductivity was discovered in AgI (Tubandt et al., 1921). The conductivity- temperature cycle for AgI below 147°C is normal ionic, interestingly, at 147°C , there is a sudden jump in the conductivity by almost three orders of magnitude. On further increasing the temperature, conductivity almost get saturated and in fact, decreases slightly at the melting point ($\sim 558^\circ\text{C}$). To understand this phenomenon, several studies have been performed. Strock (1934-1936) proposed a liquid like model for AgI which is later on reinforced by Geller, 1977 and Funke, 1976. According to these studies, below 147°C , the structure of AgI is wurtzite (Zinc Blend structure) and above that, it transforms into a body centered cubic cell of iodine ions with availability of 6 octahedral, 12 tetragonal and 24 trigonal bipyramidal (total 42) sites for two Ag^+ ions in a unit cell. Silver ions remain completely disordered in this unit cell. Such a phase ($\alpha\text{-AgI}$) has been considered as sublattice melted or

sublattice disordered. Later on, it is found that the change in entropy at 147 °C in AgI is comparable to its value at melting (O'Keeffe and Hyde, 1976).

Similar to AgI, investigations on various compounds (e.g. Ag₂Se) have been performed and several materials with α -phase have been discovered (Tubandt, 1932).

In 1964, a novel salt of Ag₃SI (formed by a simple reaction $\text{AgI} + \text{Ag}_2\text{S} \rightarrow \text{Ag}_3\text{SI}$) was found to exhibit high ionic conductivity of $10^{-2} \Omega^{-1}\text{cm}^{-1}$ at room temperature (Takahashi and Yamamoto, 1964, 1966). This compound was successfully used as electrolyte in Ag/I₂ solid state electrochemical cell that could draw the current upto $\sim 1\text{mA}/\text{cm}^2$.

This noted work of Takahashi lead the foundation of a very new and exciting field of research and development, viz., Solid State Ionics.

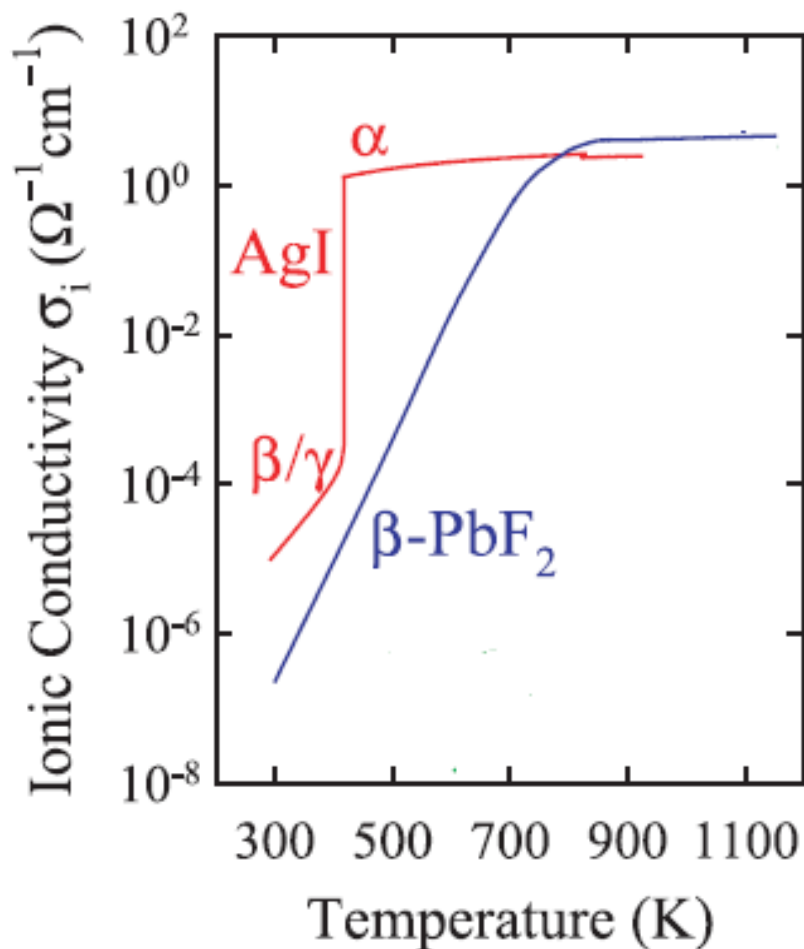


Fig. 1.1: Ionic conductivity in AgI and PbF₂ (Hull, 2004)

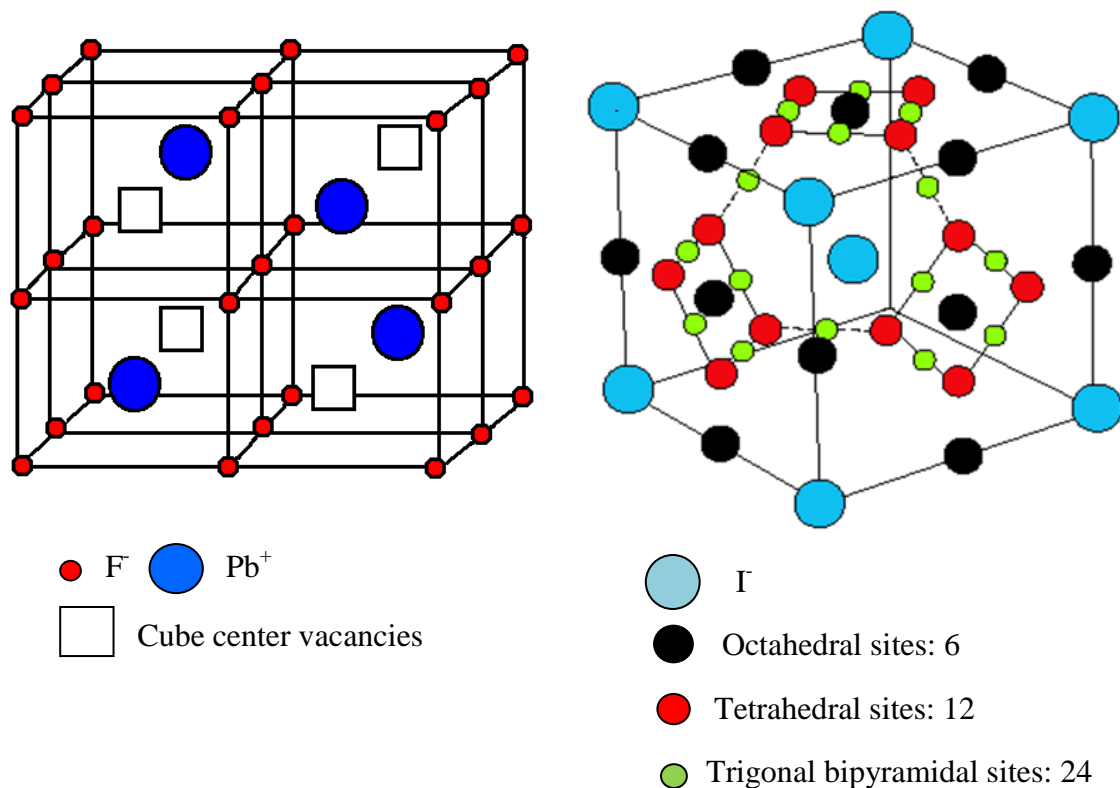


Fig. 1.2: Unit cell of AgI and PbF₂.

In 1967, a compound viz. MAg_4I_5 ($M = Rb, K, Cs$ etc) has been developed by Owens and Argue whose conductivity was found to be $\sim 0.21 \Omega^{-1}cm^{-1}$. This compound was the first fast ionic conductor even much below the room temperature ($-100^\circ C$). Similar work has also been done by Bardley and Greene (1967) group in parallel. Similar to AgI, these systems were found to be cationically disordered and there are 56 lattice sites available for 16 Ag^+ ions in per unit cell in case of $RbAg_4I_5$ (Geller 1967).

Hereafter, a new class of materials is identified and named as Superionic conductors (SICs) or fast ionic conductors (FICs) or solid electrolytes. These are ionic solids with high ionic conductivity ($\sigma > 10^{-3} \Omega^{-1}cm^{-1}$) comparable to those of molten salts at temperatures much below to their melting point. In these the ions are principle charge carriers and electronic conductivity is negligible with low activation energy of ion conduction. Due to these properties SICs has drawn attention of physicists, chemists and material scientists for possible use in solid state ionic devices. As a result, last three decades have witnessed fundamental as well as applied research and development in the field of solid state ionics.

1.2 Classification of superionic conductors

Since, number of Ag^+ , Li^+ , Na^+ , F^- and O^{2-} ion based superionic conductors are developed. Based on the physical properties the superionic conductors are categorized under four categories:

- (a) Crystalline solids
- (b) Solid polymers electrolytes
- (c) Glasses
- (d) Composites.

1.2.1 Crystalline solids: These are class of superionic conductors in which availability of lattice sites are more than the free ions. The high temperature phases of various compounds (e.g. $\alpha\text{-AgI}$, $\alpha\text{-CuI}$ and $\alpha\text{-Li}_2\text{SO}_4$ and RbAg_4I_5) are some of the examples of this category.

Boyce and Huberman (1979) have categorized these crystalline solids in three sub-categories:

- (i) **Type I:** The materials that achieve the superionic conductivity with sudden change at the transition temperature normally through a first order phase transition. In these materials, mobile ions are completely disordered and immobile ions form a new unit cell through sublattice melting.
- (ii) **Type II:** The transitions in this class of materials take place gradually and the lattice of immobile ions doesn't change its structure, however mobile sublattice disordering occurs at the transition temperature.
- (iii) **Type III:** These compounds do not exhibit any structural changes and phase transition but interestingly, the high ionic conductivity is achieved in a smooth fashion. Moreover, these materials are non-stoichiometric in nature, which exhibit no change over a range of compositions.

The compounds fall under these categories are listed in Table 1.1:

Table 1.1: Differentiation between categories of superionic crystalline solids.

Category	Material	Structure before transition	Transition temperature (in °C)	Structure after transition	Mobile ion	References
Type I	AgI	Wurtzite	147	BCC (I)	Ag ⁺	Strock (1934) Boyce (1977)
	Ag ₂ Se	Orthorhombic	133	BCC (Se)	Ag ⁺	Rahlfs(1936) Sakuma et al (1977)
	Li ₂ SO ₄	Monoclinic	575	FCC (SO ₄)	Li ⁺	Forland et al (1957)
	CuI	Zincblend	408	FCC (I)	Cu ⁺	Matsubara(1975) Krug et al(1952)
Type II	PbF ₂	Fluorite	430	-	F ⁻	Faraday (1839)
	CaF ₂	Fluorite	1150	-	F ⁻	Willis (1965)
	Na ₂ S	Antifluorite	1000	-	Na ⁺	Dworkin et al (1968)
	K ₂ S	Antifluorite	777	-	K ⁺	“
Type III	Na-β-Al ₂ O ₃	Hexagonal	-	-	Na ⁺	Yao and Kummer (1967)
	Li ₂ Ti ₃ O ₇	Ramsdellite	-	-	Li ⁺	Lundberg et al (1964)
	H _x WO ₃	Distorted pervoskite	-	-	H ⁺	Whittingham et al (1972)
	Li _x WO ₃	Distorted pervoskite	-	-	Li ⁺	“

1.2.2. Solid Polymers: Solid polymer electrolytes (SPEs) are obtained by the complexation of salt with certain donor polymers.

Fenton (1973) has investigated the polymer electrolytes but its technological applications were initiated by Armand's group (1978-1979). Armand et al. have shown that alkali metal salt in polyethylene oxide (PEO), provide a significant high ionic conductivity to make them suitable as electrolyte in solid state ionic devices. Subsequently, intensive work begun on other prospects like synthesis of new polymers, structural studies and electrical transport. These solid polymers electrolytes (SPEs) are useful due to several reasons as follows:

Improved safety, shape flexibility, manufacturing integrity and a better mechanical strength.

Till date, several types of solid polymer electrolytes have been synthesized and characterized based on different polymers such as polyethylene oxide (PEO), polypropylene oxide (PPO), polyvinyl chloride (PVC), polyvinylidene fluoride (PVdF) and polymethyl methacrylate (PMMA) etc.

To synthesize these solid polymer electrolyte films, ionic salts (e.g. Ag_2SO_4 , LiBF_4 etc.) are dissolved in polymer of high molecular weight (e.g. PEO, PPO etc.) using solution casting technique. In these SPEs, polymers act as solid solvent such that ionic salt are dissolved in the matrix of the polymers. The conduction mechanism in these polymers is associated with local structural relaxation and local segmental motion which may be interpreted on the basis of hopping mechanisms between coordinating sites available in the SPEs. Some important solid polymer electrolytes with their ionic conductivity are tabulated in Table 1.2.

Table 1.2: some synthesized polymer based electrolytes compositions which exhibit maximum conductivity.

Compositions	Ionic conductivity room temperature ($\Omega^{-1}\text{cm}^{-1}$)	References.
PEM : LiSO_3CF_3	2×10^{-5}	Bannister et al. (1984)
PEO: LiClO_4	1×10^{-6}	Gorecki et al. (1986)
PVP : H_3PO_4	$\sim 10^{-7}$	Armand (1988)
PVP : H_2SO_4	3.9×10^{-3}	Lassegues et al. (1992)
PEO:AgSCN (O/Ag)=(8/8)	1.3×10^{-6}	Sekhon et al. (1995)
PEO: NaPF_6 (Na^+/EO) ~ 0.065	3.5×10^{-6}	Hashmi et al. (1995)
70PEO:30 KNO_3	1.3×10^{-7}	Sreekanth et al. (1999)
PVP- MeAg_3I_4	6×10^{-3}	Pappenfus et al. (2004)
98(90PEO:10 AgNO_3):2PVP	$\sim 10^{-5}$	Chandra et al. (2006)
PMMA+ LiClO_4	6.7×10^{-9}	Shukla et al. (2009)
PPG + AgCF_3SO_3	7.1×10^{-5}	Suthanthiraraj et al. (2010)
PEO- NH_4ClO_4	5.8×10^{-5}	Tarafdar et al. (2010)
PCL + NH_4SCN	1.01×10^{-4}	Woo et al. (2011)
PVA + PEG-Mg (NO_3) ₂	9.63×10^{-5}	Polu et al. (2011)
PEO:P(VdF-HFP)- LiClO_4 :nano fiber	4.5×10^{-4}	Kumar et al. (2012)

1.2.3. Superionic glasses: The investigations on superionic glasses were initiated with the discovery of $\text{AgI-Ag}_2\text{SeO}_4$ glassy system (D. Kunze, 1973). The maximum electrical conductivity was found to be $3 \times 10^{-2} \Omega^{-1}\text{cm}^{-1}$ at the room temperature (300K) for the composition $75\text{AgI-}25\text{Ag}_2\text{SeO}_4$, which was 3 orders of magnitude higher than that of the conductivity of AgI at room temperature.

These superionic glasses are formed from three very important constituents:

- (i) **Glass network former:** Generally, glass formers are metal oxides (M_xO_y) and exhibit very poor ionic conductivity (e.g. SiO_2 , B_2O_3) due to covalent bonding.

Zachariasen (1932) studied the atomic arrangement in oxide glasses and concluded that there are four ultimate conditions for oxide structure which allow the formation of glassy phase.

- a. An Oxygen atom should not link with more than two glass forming atoms.
- b. The coordination number of glass forming atoms should be small than that of oxygen atoms.
- c. The oxygen polyhedra should share corners with each other, not the edges or faces.
- d. The oxygen polyhedra should be linked in three dimension network.

On the basis of these rules, he suggested that there are two types of glass formers (a) conditional and (b) unconditional.

(a) Conditional glass former:- TeO_2 , SeO_2 , MoO_3 , V_2O_5 etc which can form glassy phase only in the presence of other compound.

(b) Unconditional glass former:- B_2O_3 , P_2O_5 , As_2O_3 , Sb_2O_3 etc which can form glass structure alone.

(ii) **Glass modifier:** The glass modifiers are also metal oxides of dominant ionic and partial covalent nature which strongly intermingle with glass formers. Due to mixing of glass modifier (e.g. Na_2O , Li_2O , Ag_2O etc.), into glass former, bridging oxygen of glass formers leads to breaking of bonds, that results into increase in the number of non-bridging oxygen. These create more disorder in materials and provide the pathways for the ions to move. A glass modifier dissolved in a glass former is called a glass matrix.

(iii) **Ionic/dopant salt:** when ionic salt is mixed with glass modifier and glass network, number of charge carriers increase in the system. A salt MX dispersed into glass matrix normally dissolves in the form of cation (M^+) and anion (X^-). These dissolved ions are loosely bonded with the glass matrix and conductivity further exhibits appreciable rise due to increase in the charge carriers.

Ever since the discovery of first Ag^+ ion conducting glass by Kunze, cation (Li^+ , Na^+ etc) and anion (O^{2-} , F^- etc) conducting glasses have been developed and studied (Tuller, 1980). Out of these, Ag^+ ion based glasses exhibit highest ionic conductivity at room temperature.

Some selected AgI- oxysalt glasses are listed in Table 1.3.

Table 1.3: Some Ag⁺ ion conducting superionic oxide glasses with their conductivity (at 300K) and activation energies.

Composition	Conductivity (in $\Omega^{-1}\text{cm}^{-1}$) at room temperature	E (eV)	Investigations	References
AgI-Ag ₂ SeO ₄ (75:25)	3×10^{-2}	0.20	Rapid quenching, σ - T cycles	Kunze, 1973
AgI-Ag ₂ MoO ₄ (75:25)	1×10^{-2}	0.22	σ - T cycles, σ - composition	T. Minami et al, 1977
AgI-Ag ₂ CrO ₄ (80:20)	1.5×10^{-2}	0.15	σ - composition, electrochemical cell	Chiodelli et al, 1974
AgI-Ag ₃ AsO ₄ (80:20)	1.4×10^{-2}	0.20	σ - T cycles, construction of Cell, DTA, Dielectric studies	Grant et al, 1978
AgI-Ag ₂ O-P ₂ O ₅ (67.67:25:8.33)	2×10^{-2}	-	σ - T cycles, σ - composition	Minami et al, 1977
AgI-AgPO ₃ (57.5:42.5)	1×10^{-3}	0.25	σ - T cycles σ - AgX (X=Cl,I and Br)	Malugani et al,1979
AgI-Ag ₂ O-B ₂ O ₃ (75:15:15)	9.7×10^{-3}	0.22	σ - T cycles, Cell studies, XRD,DTA, Activation Energy	Magistris et al, 1979
AgI-Ag ₂ O-B ₂ O ₃ (55.5:22.5:22.5)	$\sim 10^{-3}$	-	μ -T, IR, σ - T cycles	Shaju and Chandra et al 1994
50AgI-33.33Ag ₂ O-16.67V ₂ O ₅	10^{-3}	-	Crystallization studies, σ - T cycles (above T _g and T _c)	Adams et al 1995
50AgI-33.33Ag ₂ O-16.67V ₂ O ₅	2.3×10^{-3}	0.34	XRD, DSC, self diffusion of Ag ⁺ ion	Kumar et al, 1996
AgI-Ag ₂ O-TeO ₂ (60:20:20)	10^{-2}	0.27	σ -composition, XRD, models for ion transport	Damrawi, 1999
AgI-AgCl-(Ag ₂ O:B ₂ O ₃) (0.525:0.175:30)	4.4×10^{-3}	-	μ -T, σ - T cycles, Cell studies, transference number	Agrawal et al, 2002
CuI-AgI-Ag ₂ O-CrO ₃ (26.25:8.75:32.5:32.5)	9.55×10^{-4}	-	XRD, electrical transport	Suthanthiraraj et al, 2002
AgI-Ag ₂ O-V ₂ O ₅ (67:22.33:10.67)	1×10^{-2}	0.20	Mechanochemically synthesized XRD,DSC, σ - T cycles Theoretical model	Dalvi et al, 2004
CdI ₂ -Ag ₂ O-V ₂ O ₅ -B ₂ O ₃	10^{-4}	-	Transport number, thermoelectric power, cell	Padmasree and Kanchan, 2008
50AgI-23.33Ag ₂ O-9.99Cu ₂ O-6.67V ₂ O ₅	1×10^{-2}	0.19	σ - T cycles, Cell studies, thermal stability XRD,DSC	Present work

1.2.4 Superionic composites: Superionic composites consist of multiple phases and known as heterogeneously doped materials or dispersed solid electrolytes. These may be categorized in four parts:

On the basis of structure, these superionic composites are categorized in 4 parts:

a. Crystal-crystal composites: These composites can be further categorized in two parts,

- (i) **Mixed crystal effect:** Solid solution formation (e.g. $\text{AgCl}_x\text{Br}_{1-x}$) enhances the ionic conductivity due to lattice loosening/weakening.
- (ii) **Dispersoids:** Dispersion of fine insulator particles of (e.g. Al_2O_3 , ZrO_3 etc.) in host ionic conductor (e.g. CuI , AgI etc.).

Firstly, intensive work on composites started in 1973, when C. C. Liang reported the enhancement in the conductivity of LiI by dispersing of fine alumina particles. Subsequently, various composites are discovered with enhancement in conductivity. Various models were also suggested for the significant rise in conductivity (Jow et al, 1979; Maier, 1986; and Shahi et al, 1981). But the majority of the models suggested that enhancement in the conductivity is due to existence of a space charge region at the interface of host and dispersoid in two phase composites. This space charge region is responsible for creation of defects in the system. The conductivity enhancement in these composites depends on the size of dispersed ionic conductor or fine insulating particles. It has been found that the smaller the particle size, the larger the conductivity enhancement. This enhancement in the conductivity is due to increased surface area of dispersoid.

b. Glass-ceramic composites: To prepare this type of composites, (i) either freezing of highly conducting high temperature phase unstable superionic materials (e.g. α - AgI) or (ii) dispersing of insulator particles (Al_2O_3 , SiO_2 etc.) in an ion conducting glassy system has been done (Nowinski et al, 1989) or (iii) by heat treatment. Three orders of enhancement in the conductivity is reported in Ag^+ ion conducting composite system in which α - AgI was frozen in the glass systems $\text{AgI-Ag}_2\text{O-M}_x\text{O}_y$ where $\text{M}_x\text{O}_y = \text{B}_2\text{O}_3, \text{WO}_3, \text{P}_2\text{O}_5, \text{CeO}_2$ etc. (Tatsumisago et al 1991). In an interesting study on large AgI content $\text{AgI-Ag}_2\text{O-MoO}_3$ glasses, conductivity of glass-ceramic composite samples is found to be higher than that of respective amorphous/glassy state (Tatsumisago et al 2001).

- c. Crystal-polymer composite:** In this type of composites, enhancement in the conductivity is due to dispersion of organic or inorganic filler (PEO-PMMA, Al₂O₃) in polymer electrolytes. It is also reported in literature that dispersion of these filler has not only enhanced the ionic conductivity but also improved the mechanical strength of the polymer electrolytes.
- d. Glass-polymer composite:** To improve the mechanical stability and ionic conductivity of polymer electrolytes, ion conducting glass can be dispersed in polymer electrolytes. These high ion conducting glasses dispersed at time of preparation of polymers.

Some important work on composites is given in Table 1.4.

Table 1.4: Some examples of different types of superionic composites.

Category	Material	Ionic conductivity room temperature ($\Omega^{-1}\text{cm}^{-1}$)	Reference
Crystal-Crystal composite	60LiI-40Al ₂ O ₃	1.2×10^{-5}	Liang (1973)
	0.7AgI-0.3Al ₂ O ₃	6.0×10^{-4}	Shahi et al (1981)
	75AgI-25AgBr	3.2×10^{-4}	Shahi et al (1982)
	PbF ₂ -SiO ₂		Hariharan et al (1995)
	0.7AgBr-0.3Al ₂ O ₃	3.1×10^{-3}	Yamada et al (2006)
Glass-ceramic composite	82 α -AgI(13.5 Ag ₂ O-4.5B ₂ O ₃)	4.2×10^{-2}	Tatsumisago et al (1991)
	(66.67AgI-14.29Ag ₂ O-19.04MoO ₃)10.5Al ₂ O ₃ (wt %)	7.0×10^{-3}	Arof (1994)
	(50AgI-33Ag ₂ O-17B ₂ O ₃)- α Al ₂ O ₃ (50:50)	10^{-3}	Foltyn et al (2008)
	40(41.5Li ₂ O-24.5LiCl-34P ₂ O ₅)-60Al ₂ O ₃	1.4×10^{-4}	Yun et al (1987)
	40AgI-60(Ag ₂ O-P ₂ O ₅)- α Al ₂ O ₃		Nowinski et al (1989)
	(55.5AgI-22.25Ag ₂ O-22.25B ₂ O ₃) 30SnO ₂ (wt %)	1.0×10^{-3}	Shaju et al (1995)
Crystal-polymer composite	(PEO-LiI)-0.05Al ₂ O ₃	10^{-3}	Nagasubramanian et al (1993)
	(PEO-AgSCN)-10Al ₂ O ₃	8.8×10^{-4}	Sekhon et al (1996)
	PEO-LiBF ₄ -MgO	1×10^{-5}	Kumar et al (2001)
	PEO-NaClO ₄ -Na ₂ SiO ₃	1×10^{-3}	Hashmi et al (1998)
	90(PEO-NaI)-10Al ₂ O ₃	6.5×10^{-5}	Przyluski et al (1989)
	(5PVC-20PEMA)-8LiClO ₄ (wt%)	4.3×10^{-3}	Rajendran et al (2010)
Glass-polymer composite	PEO (Na ₂ O-3B ₂ O ₃)	10^{-10}	Magistris et al (1994)
	(PEO-LiBF ₄) Lithium borosulphate glass	10^{-7}	Kumar et al (1994)
	PEO-LiClO ₄ :(Li ₂ O-Al ₂ O ₃ -TiO ₂ -P ₂ O ₅)	5×10^{-4}	Zhang et al (2002)

Recently, new interesting composites of glass with ionic liquid become a subject of interest. Various studies on these composites have been performed.

A new Li^+ ion conducting ternary composite electrolyte SiO_2 -(BMIM) BF_4 -LiTf where ([BMIM] BF_4) is 1-butyl-3-methylimidazolium tetrafluoroborate, and LiTf is lithium trifluoromethanesulfonate) has been studied (Echelmeyer et al, 2009). When ionic liquid and Lithium salt are dissolved in amorphous silica glass network, conductivity enhances and maximum conductivity was found to be $0.5 \times 10^{-2} \Omega^{-1} \text{cm}^{-1}$ at room temperature.

1.3. Superionic glasses: an overview

Since the investigations in the present thesis involve studies on fundamental Ag^+ ion conducting superionic glasses, this section discusses an overview of glassy superionic conductors. Ion conducting glasses have been studied with deep scientific interest for last three decades in view of their possible applications in solid state ionic electrolyte e.g. batteries, fuel cells, electrochromic devices (Minami, 1987; Hariharan et al, 1988). Important experimental investigations in last three decades on superionic glasses are presented here. The theoretical aspects are presented in respective section.

In particular, AgI-oxysalt glasses are known to show high ionic conductivity up to $\sim 10^{-2} \Omega^{-1} \text{cm}^{-1}$ at room temperature (Tuller et al, 1980; Minami et al, 1988). In order to improve the ionic conductivity and other properties of these glasses, various structural modifications have been done.

- (i) **Mixed glass former effect:** The effect of the presence of two mixed glass formers (Magistris et al, 1983; Agrawal et al, 2002) is studied. Magistris et al have shown that lower AgI contents borophosphate glasses exhibit conductivities higher than the analogous glasses containing only boron or phosphorus.
- (ii) **Mixed alkalis effect:** This effect on electrical conductivity has also been studied for various glassy systems (Hariharan et al, 2006; Mundy et al, 1986; Kanchan et al, 2010). To study the mixed alkali effect Mundy et al have chosen Na_2O - Rb_2O - GeO_2 system. They found that conductivity decreases and reaches till minimum and again increase with increase of Rb_2O content.

(iii) **Mixed cation effect:** The effect of the presence of two different cations (e.g. Ag^+ and Cu^+ ion in silver oxysalt glasses) has also been investigated (Hariharan et al, 1992 Suthanthiraraj et al, 2010). Interestingly, addition of CuI provides AgI in the system by an exchange reaction according to Pearson's theory. Moreover, due to low cost, non hygroscopic nature and similar chemical properties to that of AgI, CuI has been used by various workers as a possible dopant in silver oxysalt matrix. It was found that conductivity increases with CuI substitution in AgI-oxysalt glasses. Similarly, combination of different dopants like, PbI_2 (Padmashree et al, 2009), NaI (Sekhon et al, 1999) and CdI_2 (Chitradevi et al, 2006) in the silver oxysalt matrix has also been developed.

Few examples on each category are given in Table 1.5

Table 1.5: Some examples of mixed glass formers, mixed alkali and mixed cation effects.

Effect	System	References
Mixed glass former effect	$\text{AgI-Ag}_2\text{O-V}_2\text{O}_5\text{-P}_2\text{O}_5$	Prasad et al, 1990
	$\text{Ag}_2\text{O-MoO}_3\text{-P}_2\text{O}_5$	Deb et al, 2010
	$\text{Ag}_2\text{O-B}_2\text{O}_3\text{-P}_2\text{O}_5$	Deb et al, 2010
	$\text{AgI:Ag}_2\text{O-V}_2\text{O}_5\text{-TeO}_2$	Sharma et al, 2010
Mixed Alkali effect	$\text{Na}_2\text{O-2CaO-SiO}_2$	Rolling et al, 2000
	$(\text{Li}_2\text{O-Na}_2\text{O})\text{-B}_2\text{O}_3$	Selvaraj et al, 1984
	$\text{Li}_2\text{O-Na}_2\text{O-P}_2\text{O}_5$	Bergo et al, 2007
	$\text{Ag}_2\text{O-Na}_2\text{O-B}_2\text{O}_3$	Sekhon et al, 1999
Mixed Cation effect	$\text{CuI-AgI-Ag}_2\text{O-P}_2\text{O}_5$	Murugesan et al, 2002
	$\text{PbI}_2\text{-AgI-Ag}_2\text{O-P}_2\text{O}_5$	Swenson et al 1999
	$\text{CdI}_2\text{-AgI-Ag}_2\text{O-MoO}_3$	Chitradevi et al, 2006
	$\text{CuI-AgI-Ag}_2\text{O-V}_2\text{O}_5$	Present work

These mixed glass former, mixed alkali and mixed cation effects are responsible for structural changes and thus lead to appreciable change in properties of the glass.

To study the structural modifications in the superionic glasses various techniques have been used such as neutron diffraction, EXAFS, x-ray diffraction and EPR techniques. Thermal investigations has also been used for structural investigations above glass transition and crystallizations in superionic glasses.

There are interesting investigations on structure of $(\text{AgI})_x-(\text{Ag}_2\text{O}-2\text{B}_2\text{O}_3)_{1-x}$ glassy system using EXAFS, Neutron diffraction and EPR techniques. These results show that increase of AgI amount in glass matrix results into increased intermediate-range. These intermediate-ranges occur due to network of boron and oxygen. Thus the enhancement in the conductivity is due to creation of new pathways through these intermediate ranges instead of presence of AgI clusters (Swenson et al, 1997).

Using frequency and temperature-dependent conductivity data for AgI-AgPO₃ glasses, it has been calculated that the number density of mobile ions as well as the ionic relaxation mechanism are independent of temperature and composition. This result is important in order to clarify the role of AgI for the ion transport in these glasses (Roling et al, 1997).

The systematic σ - T cycles have been performed on mechanochemically synthesized AgI-Ag₂O-M_xO_y (M_xO_y = MoO₃, CrO₃, V₂O₅) superionic glasses. These samples exhibit interesting trends for σ - T cycles above T_g and T_c (Dalvi et al 2003-2005). In a series of investigations by Dalvi et al. (Dalvi et al 2003,2004,2005), Ag⁺ ion conductivity of mechanochemically synthesized samples, viz. AgI-Ag₂O-M_xO_y (M_xO_y = V₂O₅, MoO₃, CrO₃) has also been thoroughly studied using crystallization kinetics by differential scanning calorimetry (DSC).

Solid state electrochemical cells of type Ag|aSIC|I₂ are fabricated using mechanochemically synthesized amorphous superionic conductors (aSIC), AgI-Ag₂O-M_xO_y (M_xO_y = B₂O₃, V₂O₅, CrO₃) as electrolytes. The conductivity of these systems is in the range of 10⁻² – 10⁻³ Ω⁻¹cm⁻¹ and the transport number of Ag⁺ ions is near unity (Dalvi et al, 2002).

Various studies have been performed in order to scrutinize the electrical transport below T_g. It is demonstrated by Adams et al. that σ - T cycles measured at a typical heating rate do infer interesting thermal events (e.g., T_g, T_c). Through these systematic σ - T cycles and high-temperature X-ray diffraction (XRD) studies, they attributed the anomalous rise in conductivity above T_g in the AgI-Ag₂O- V₂O₅ (Adams et al, 1995) system to glass-crystallite interface effect.

It is also realized that prior to any application, study of thermal properties is unavoidable and very essential as the high temperature can heavily influence the performance of battery. The excessive temperature rise and sharp temperature gradient within a battery could also result in the battery failure (Shi et al, 2006). In view of this, some interesting studies have been performed on thermal properties of ion conducting glasses recently.

Recently, AgI–Ag₂O–P₂O₅ glassy system (Nowinski et al, 2006) and Na⁺ ion conducting phosphate glass (Reynoso et al, 2003) have also been investigated using crystallization kinetics. Investigation of thermal properties using DSC technique has been found to be useful to understand structural properties as well. For example, amorphous AgI aggregation model has been validated by Hanaya et al, 2005. using calorimetric studies. Very recently, thermal stability and crystallization kinetics parameters have been obtained in Li⁺ ion conducting glasses Li₂O–SiO₂–TiO₂ by (Moricova' et al, 2010).

In a broad prospective, based on DSC investigations, there are several parameters given by various researchers to scrutinize the thermal stability of glasses. For example, temperature corresponding to maximum rate of crystallization T_p, melting temperature T_m, glass forming tendency (T_c - T_g), Kauzmann temperature T_{rg}, Hruby constant k_{gl}, activation energies for structural relaxation E_s and crystallization E_c, are mainly used for various glassy systems (Moynihan et al, 1974; Kissinger et al, 1957; Hruby et al, 1972; Kauzmann et al, 1948). Recently, it is shown by Aly et al. that MoO₃ addition in PbO–Sb₂O₃–As₂O₃ glasses significantly affects the thermal stability parameters.

Non isothermal crystallization kinetics using DSC has also been used on some AgI glassy systems e.g. AgI–Ag₂O–B₂O₃ (Taniguchi et al, 1995), AgI–Ag₂O–P₂O₅ (Nowinski et al, 2006) and also to point out significant differences between melt quenched and mechanochemically synthesized Ag⁺ ion conducting AgI–Ag₂O–M_xO_y (M_xO_y = V₂O₅, CrO₃ etc) (Dalvi et al, 2004) and AgI–Ag₂O–CrO₃ (Dalvi et al, 2003) superionic glasses. The significant high ionic conductivity in mechanochemically synthesized (MCS) systems than those of respective conventionally melt-quenched (MQ) samples is attributed due to high disorder in former.

1.4. Development of materials and applications

1.4.1 Novel methods of preparation of glassy superionic conductors

In order to prepare high ionically conducting, electrochemically stable and chemically homogeneous glassy superionic conductors (SICs), new and better preparation methods are also of primary concern. Many new methods have been developed and used in the last few years to prepare glassy SICs. Using mechanochemical synthesis (high energy ball milling) Li^+ (Morimoto et al, 1999) and Ag^+ (Dalvi et al, 2003-2005) ion based glasses have been prepared. Sol gel processing technique and microwave assisted synthesis have also been used to prepare some glasses (Mustarelli et al, 1996).

Microwave assisted synthesis or microwave processing another relatively new technique in the field of solid state ionics. So far, this route has been used to prepare some LiMn_2O_4 (Nakayama et al, 2003) CuBi_2O_4 (Bhat et al, 2000) electrode materials, and few Ag^+ (Vaidhyanathan et al, 1994; Gupta et al, 2008) ion based superionic glasses. Microwave processing offers significant advantages over conventional thermal techniques such as very short reaction times owing to very high heating rates to prepare glassy materials. It can limit the grain size and produce the materials of superior properties. For the microwave synthesis, it is important that at least one of the constituents of the mixture couples with it.

Mechanochemical synthesis technique is used by metallurgists for uniform mixing, synthesis of nanocomposites and amorphous alloys. It is also a relatively new technique in the field of solid state ionics. In this technique, mechanical energy is used for chemical conversion of solids. Morimoto et al (1999) have synthesized Li^+ ion based amorphous $\text{Li}_2\text{S-SiS}_2$ superionic system using this technique and electrical conductivity was found to be as high as ($\sim 10^{-4} \Omega^{-1}\text{cm}^{-1}$) that of glass prepared by conventionally quenching. Apart from these, a series of AgI based superionic conductors are prepared using the mechanochemical synthesis and a comparative study have been carried out with those of the samples prepared by conventional melt quenching (Dalvi et al, 2001-2005).

Some of the superionic conductors, viz. $\text{AgI-Ag}_2\text{O-M}_x\text{O}_y$ ($\text{M}_x\text{O}_y=\text{V}_2\text{O}_5, \text{CrO}_3$ etc.) (Nowinski et al, 2008) have been prepared and characterized.

1.4.2 Applications of superionic glasses

The development of electrochemical devices using superionic glasses as a solid electrolyte is an interesting work in the field of solid state ionics. In view of this, glassy materials and thin films of these glasses have been thoroughly studied to achieve the high ionic conductivity at ambient temperature. These glasses are widely used in various fields. Some of them are:-

Solid state batteries, Sensors, Fuel cells, Supercapacitors, Electrochromic displays, Solid , electrolytes thermometers, Thin Film batteries, Heterogeneous catalysis, Biomedical application.

Table 1.6: Description of some electrolytes with their open circuit voltage and cell type.

No.	Solid Electrolytes	OCV	Cell type	References
1	AgI-Ag ₂ O-V ₂ O ₅	0.686	Ag/V ₂ O ₅	Minami et al (1988)
2	AgI-Ag ₂ O-ZnO-MoO ₃	0.682	Ag/KI ₃	Arof et al., 1995
3	AgI-Ag ₂ O-SeO ₂ -MoO ₃	0.687	Ag/I ₂ +C	Baskaran et al., 1995
4	(AgI:AgCl)-Ag ₂ O-B ₂ O ₃	0.684	Ag/I ₂ +C	Agrawal et al., 1996
5	AgI-Ag ₂ O-SeO ₂ -As ₂ O ₃	0.684	Ag/I ₂ +C	Venkateswarlu et al., 1998
6	AgI-Ag ₂ O-M _x O _y (M _x O _y = V ₂ O ₅ , CrO ₃ B ₂ O ₃)	0.685-7	Ag/I ₂ +C	Dalvi et al., 2002
7	CdI ₂ -Ag ₂ O-V ₂ O ₅ -B ₂ O ₃	0.678	Ag/I ₂ +C	Padmasree et al (2006)
8	Ag ₂ O-P ₂ O ₅ -LiCl	0.668	Ag/I ₂ +C	Das et al., 2010
9	CuI-AgI-Ag ₂ O-V ₂ O ₅	0.682	Ag/I ₂ +C	Present work

1.5. Theoretical Aspects

1.5.1 Models proposed for ionic motion in glasses:

Mostly, point defects are responsible for ionic motion in crystals and various models very well explain ionic conductivity in crystalline solids, but such models cannot be applied to glassy systems because of their “liquid like” complex structure. In view of this, various models are proposed to understand the ionic motion in superionic glasses. Some of them are discussed here.

1.5.1.1 Cluster bypass model:

This model is first proposed by Goodman in 1975 and later modified by Phillips, 1981; Rao and Rao, 1982. However, the conduction process in glass was first time explained by Ingram (1988). In this model, it was assumed that there are ordered micro domains/clusters of diameter $\sim 25\text{-}50 \text{ \AA}$ in ionically conducting glasses. When residual liquid is cooled below T_g , the highly disordered phase is obtained due to solidifying of surrounding clusters. This highly disordered phase is referred as connecting tissues which provides pathways for the conducting ions as shown in Fig 1.3.

With the help of this model ion conduction can be explained in some AgI based glasses with an argument that nature of these clusters may not be crystalline in nature, but in the form of small island. Moreover, this model explains the ion transport in mixed alkali systems using the phenomenon of grain boundary. Goodman suggested that there is natural tendency for foreign alkali cations to plate out onto the surfaces of the clusters which blocks the preferred pathways and the diversion of the current onto clusters.

This model is also supported by some experimental techniques like Neutron diffraction (Tachez et al, 1986) and EXAFS (Benasai, 1991, Rocca et al 1992). For example, EXAFS studies on AgI-AgPO_3 and $\text{AgI-Ag}_2\text{O-B}_2\text{O}_3$ glasses confirm the dispersion of α - AgI like amorphous clusters of size $\sim 25\text{-}30 \text{ \AA}$.

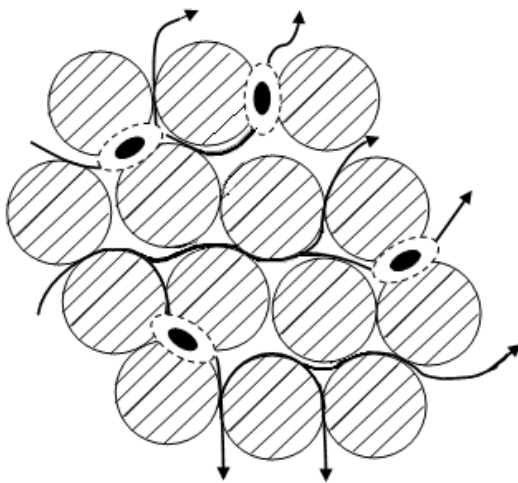


Fig. 1.3: Cluster by pass model explanation

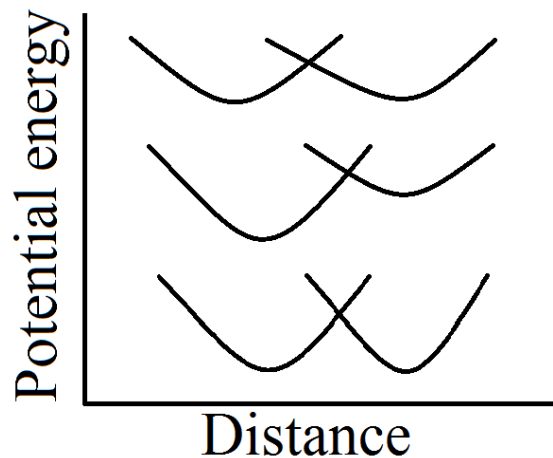


Fig. 1.4: Schematic of diffusion path model (after Minami, 1985)

Interestingly, the non Arrhenius behavior in some AgI rich glasses e.g. $\text{Ag}_7\text{I}_4\text{AsO}_4$, Grant et al, 1978) observed below T_g . According to this model, it is argued that these glasses contain clusters of amorphous AgI. The increase in conductivity may be due to increase in the concentration of mobile ions within connective tissues. The aggregation of AgI into the clusters should have an effect of removing the AgI from the connective tissues and lowering overall conductivity.

1.5.1.2 Diffusion path model

This model was developed for AgI-based iodoborate glasses by Minami in 1985. According to this model, there are two types of Ag^+ ions in these glasses. Ag^+ ions which are associated with iodide ions do contribute in the conduction process. There is large potential difference due to presence of multiple anions, viz. oxygen and iodine. The Ag^+ ions are surrounded by oxygen ions form deep and narrow potential well, while, those surrounded by iodide ions form wide and shallow well (Fig 1.4). In the disordered structure of glass, the large potential energy barriers are result of coexistence of two oxide ions, whereas, interaction of two iodide ions results in smallest potential energy barrier. Therefore, Ag^+ ions associated with oxide ions are less mobile. The interconnection of wide and narrow wells up to longer distance forms a favorable path for ionic transport. These paths are called **diffusion paths**.

The EXAFS studies (Delba et al 1983) on these silver iodoborate glasses confirms the diffusion path model as studies have confirmed the two types of Ag^+ ions.

1.5.1.3 Structural model

This model was proposed by Minami et al (1980) for $\text{AgI-Ag}_2\text{O-MoO}_3$ glasses. On the basis of electrical conductivity and FTIR results, it was proposed that Mo-O bond get weaker in glassy state compare to those of in polycrystalline state due to presence of partial covalence bond between Ag^+ and non bridging oxygen ions.

Similar to diffusion path model, there are also two types of Ag^+ ions, one of those surrounded by iodide ions whereas, other one are surrounded by MoO_4^{2-} ions. Ag^+ ions which are surrounded by molybdenum ions are less mobile. Although those of surrounded by Iodide ions are more mobile and dominate the ionic conduction in the glass. The schematic representation of this model is shown in Fig. 1.5.

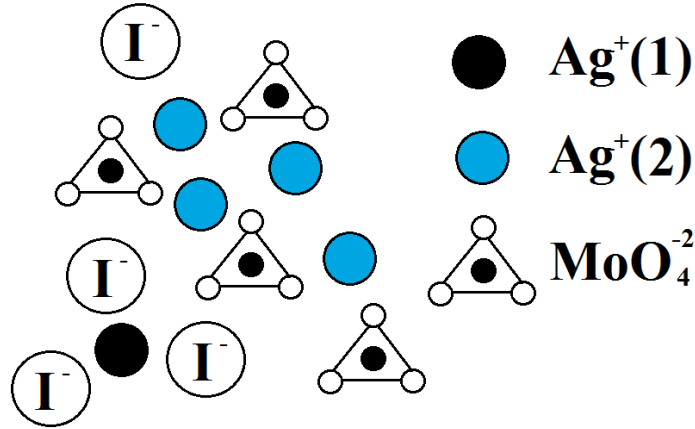


Fig. 1.5: Ionic transport with structural model

1.5.1.4 Dynamic structural model

This model was proposed for ionic motion for glasses with mixed alkali effect. According to this model, the local environment of any cation in mixed alkali glasses is largely unaffected by addition of a second cation, as confirmed by EXAFS (Greaves et al, 1990) and Far infrared spectroscopic (Rouse et al, 1978) studies. Thus, the mobile ions create and maintain their own distinctive environments. It is shown that if an ion “A” will be jump to a vacancy it inclined to the vacancy which is created by another ion of the same species and decline to that is created by different species “B” (Fig. 1.6). This effect is also called site memory effect which provides a universal mechanism for creating conducting pathways in glasses.

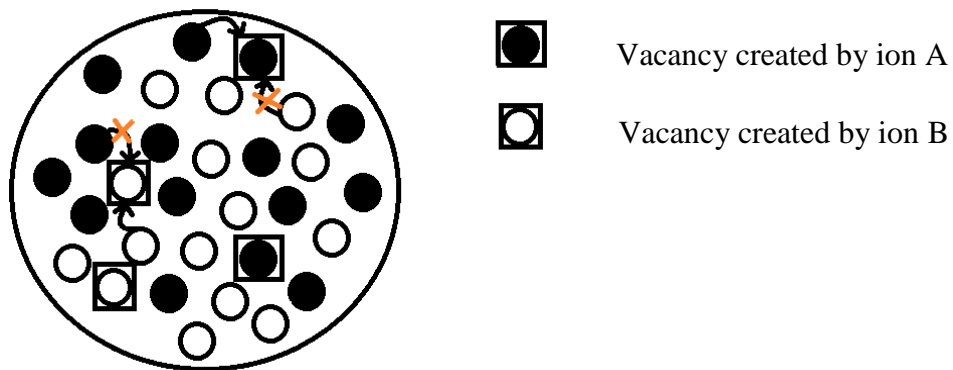


Fig.1.6: Dynamic structural model explanation.

1.6 Statement of the problem

Thus it can be inferred from the literature that investigations, for example, (i) thermal stability (ii) understanding of electrical transport above T_g and T_c is either missing or has not got considerable attention. Moreover, the fundamental characterizations of glass-ceramic nanocomposites have also not been done properly. Thus present work has undertaken the following issues to develop the understanding in Ag^+ ion conducting fundamental superionic glasses in view of the above unrevealed issues.

1. Thermal stability investigations on these superionic glasses using differential scanning calorimetry and electrical conductivity-temperature cycles.
2. Understanding of the electrical transport in glasses above T_g and T_c .
3. Preparation of glass-ceramic nanocomposite from Ag^+ ion conducting glasses and their (i) electrical, (ii) structural, (iii) thermal and (iv) electrochemical characterization.

In order to achieve these broad goals a well known basic system $AgI-Ag_2O-V_2O_5$ has been chosen for investigations due to its complex structure, wide glass forming region, non hygroscopic nature and interesting electrical transport characteristics in wide temperature range. The advantages of choosing this system are that this is non hygroscopic and easy to handle.

Three types of systems chosen for the present study where $AgI-Ag_2O-V_2O_5$ is basic are as follows,

1. **$CuI_x-AgI_{1-x}-Ag_2O-V_2O_5$: CI-SISOVO**
2. **$AgI-(Cu_2O)_x-(Ag_2O)_{1-x}-V_2O_5$: SICOSOVO**
3. **$AgI-Ag_2O-(V_2O_5)_{1-x}-(MoO_3)_x$: SISOVOMO**

To fulfill the first goal, thermal stability parameters have been calculated and glass transition and non-isothermal crystallization kinetics have been performed on all these samples. For the second goal, conductivity - temperature cycles have been carried out for a wide range of temperatures ($T < T_g$; $T_g \leq T \leq T_c$; $T_c \leq T$). The electrochemical button type cells are also prepared using these glasses and glass-ceramics as electrolytes.

1.7 The glassy system for the present study:

The fundamental, well investigated AgI-Ag₂O-V₂O₅ glass has been chosen as a basic system for the thesis. An overview of the system is discussed below.

AgI-Ag₂O-V₂O₅ (SISOVO): an overview

Out of the various explored Ag⁺ ion conducting glasses, AgI-Ag₂O-V₂O₅ glassy system (abbreviated as SISOVO) has been the subject of interest due to its complex structure and interesting electrical transport characteristics in wide temperature range. Moreover, SISOVO is a non hygroscopic system and easy to handle at and below room temperature as well. Various studies have indicated that AgI content in SISOVO do affect the electrical conductivity significantly (Adams et al, 1996; Kraswoski et al, 2000). It is demonstrated that the glass modifier to former ratio (Ag₂O:V₂O₅) affects the electrical conductivity and crystallization in SISOVO (Kraswoski et al, 2000).

The most important feature of the SISOVO system is its electrical conductivity behaviour with temperature for $T_g \leq T \leq T_c$. It has been shown by various investigators that if the conductivity is measured at some typical ramps, the thermal events at glass transition temperature (T_g) and crystallization temperature (T_c) are clearly visible in the σ -T cycles (Adams et al, 1996; Kraswoski et al, 2001). Interestingly, the electrical conductivity exhibits anomalous rise above the T_g followed by a drastic fall at the crystallization. The main phase found in the precipitated compound is those of Ag₈I₄V₂O₇, Ag₄V₂O₇ and AgI (Adams et al, 1996; Dalvi et al, 2004). Thus it is also found that annealing of SISOVO above T_c leads to the formation of interesting glass-ceramic composites (Krawoski et al, 2001). On the basis of diffusion and conductivity measurements, it is shown in SISOVO system that identical processes are responsible for conductivity and diffusion mechanisms (Suresh Kumar et al). The conductivity relaxation in these glasses is found to be highly non exponential and show strong dependence on composition than the temperature (Bhattacharya et al, 2003).

Effect of mixed modifier AgI-Ag₂O-V₂O₅-P₂O₅ has also been investigated in SISOVO system. Moreover, it is very well explained by the differential thermal analysis and Raman studies that

the structural properties of the glass network are strongly affected by Ag_2O to $\text{P}_2\text{O}_5\text{-V}_2\text{O}_5$ ratio (Garbarczyk et al, 2000). These studies suggest that SISOVO exhibits a complex structure.

In addition to various studies on SISOVO, the effect of presence of two cations (e.g. Ag^+ and Cu^+) has been investigated in other AgI based glasses as well (Hariharan et al, 1992; Suthanthiraraj et al, 2002). Moreover, mixed glass former effect (Magistrit et al, 1983; Agrawal et al, 2002) and mixed modifier effect has also been studied (Sekhon et al, 1999) in various AgI based glassy superionic conductors.

CHAPTER 2

EXPERIMENTAL TECHNIQUES

This chapter discusses in detail the structural, electrical, thermal and electrochemical characterization techniques which are thoroughly used in the present study. Some theoretical aspects of these techniques are also discussed.

2.1. Sample Preparation

Glasses:

The glassy samples were prepared by conventional melt quenching. The mixture of the chosen compositions is kept well above the melting point for sufficient time to ensure homogeneity of the melt. The melt is poured between two clean copper blocks (area $\sim 170 \text{ cm}^2$) and rapidly quenched to room temperature. These films thus obtained after quenching the melt were thoroughly ground and fine powder was used for various investigations.

The systems with following compositions were chosen for the present study:



It is ensured that these compositions lie well within the glass forming region. Though for the studies on glass-ceramics, compositions at the boundary of phase diagrams were also prepared and characterized.

Glass-ceramics:

These glassy samples are annealed above complete crystallization temperatures (at $\sim 170^\circ\text{C}$) for $\sim 4-5$ hrs to obtain the glass-ceramic samples.

2.2. Structural studies

2.2.1. X-ray diffraction

The samples prepared by melt-quenching technique were analyzed by X-ray diffractometer (RIGAKU) with a typical CuK_α radiation of wavelength of 1.54 Å. The samples in the pellet form with thickness of ~1 mm were used for characterization. For all the compositions of a particular system, the amount used for XRD is kept constant for a comparative study. The average particle size was obtained using Debye-Scherrer formula (Cullity, 1978)

$$t = \frac{0.9\lambda}{B \cos \theta_B}$$

Which can be determined in the following way:

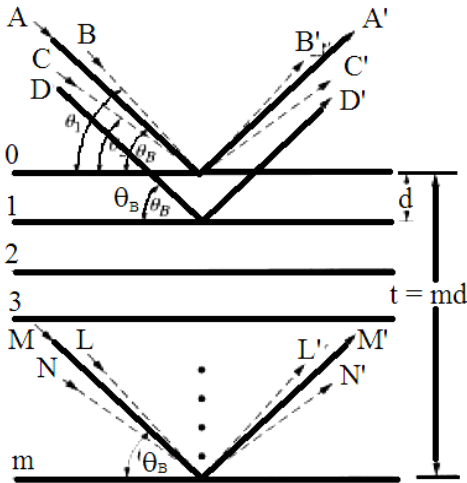


Fig. 2.1a: Diffraction from multiple planes of a crystal.

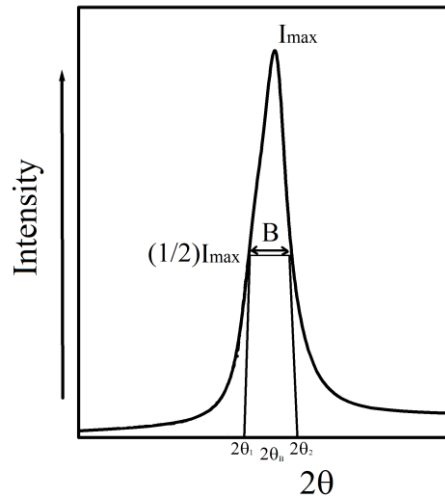


Fig. 2.1b: Extended view of x-ray diffraction peak.

Bragg condition is given by

$$\lambda = 2d \sin \theta_B \quad (2.1)$$

If two rays (beams B and C in Fig. 2.1a) incident on a crystal plane with angle θ_1 and θ_2 , respectively then,

$$2t \sin \theta_1 = (m + 1)\lambda \quad (2.2)$$

And,

$$2t \sin \theta_2 = (m-1)\lambda \quad (2.3)$$

From equations (2.2) and (2.3),

$$t(\sin \theta_1 - \sin \theta_2) = \lambda \quad (2.4)$$

So,

$$2t \sin\left(\frac{\theta_1 - \theta_2}{2}\right) \cos\left(\frac{\theta_1 + \theta_2}{2}\right) = \lambda \quad (2.5)$$

Since θ_1 and θ_2 are very close to θ_B , then we can use the following approximation,

$$\left(\frac{\theta_1 + \theta_2}{2}\right) = \theta_B \quad (2.6)$$

And,

$$\sin\left(\frac{\theta_1 - \theta_2}{2}\right) = \left(\frac{\theta_1 - \theta_2}{2}\right) \quad (2.7)$$

From equations 2.5, 2.6 and 2.7,

$$2t \left(\frac{\theta_1 - \theta_2}{2}\right) \cos \theta_B = \lambda \quad (2.8)$$

$$t = \frac{\lambda}{B \cos \theta_B} \quad (2.9)$$

Where B is full width at half maximum for a peak corresponding to diffraction, and given by

$$B = \sqrt{W_s^2 - W_{si}^2}$$

Where W_s and W_{si} are the FWHM values of the sample and silicon standard respectively.

After incorporating the correction factor,

$$t = \frac{0.9\lambda}{B \cos \theta_B} \quad (2.10)$$

where, t is the size of the particles in meters, λ is the wavelength of the X-rays in meters, θ the angle in degrees, and B is the full width at half maxima in radians for corresponding diffraction peak appears at 2θ .

2.2.2. Scanning electron microscopy

Scanning electron microscope (SEM) uses electrons instead of light to form an image. Whereas, field emission scanning electron microscope (used in present study) is an upgraded version of SEM, in which field emission cathode (e.g. LaB_6) is used in place of tungsten filament in electron gun. This field emission cathode provides narrower probing beams for low as well as high electron energy and provides a clearer and ultra high magnification of images. In field emission scanning electron microscopy (FESEM), electrons are accelerated by a voltage ($\sim 30\text{kV}$) and the electron beam is formed. To focus this electron beam, multiple lens/electron lens are used so that dimension of beam focusing on the sample should be $\sim 5\text{-}100\text{nm}$. With the help of apertures, size of beam and electron probe current can be varied. When the beam is made incident on the sample various type of (viz., backscattered, Auger, x-ray, secondary) electrons/photons emit due to scattering of electron of beam from the sample. The schematic diagram of SEM is presented in Fig. 2.2.

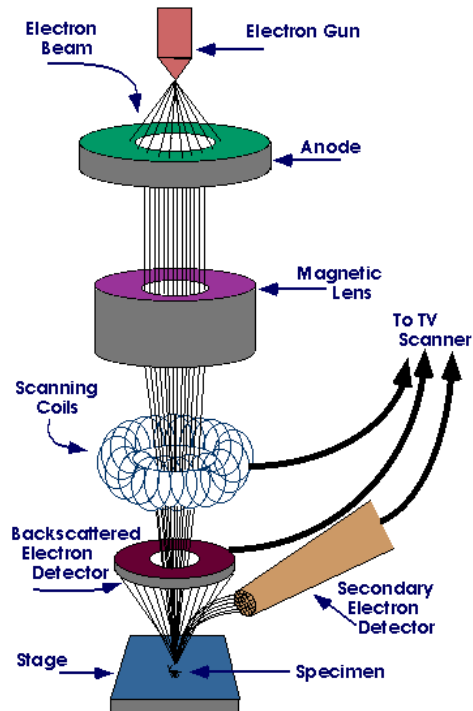


Fig. 2.2: Schematic diagram of a typical scanning electron microscope.

In SEM, the image construction is accomplished by mapping the intensity of one of the secondary or back scattered electrons signals from the specimen on to a viewing screen through the back scattered electron.

Samples are prepared by gold coating through ion sputtering unit, the samples used in present work were examined using a ZEISS ultra 60 modal SEM. Maximum magnifications of 500000X and minimum of 10X could be achieved using this microscope. The images are obtained in a computer which is interfaced with this microscope.

2.3 Thermal Analysis

2.3.1 Differential scanning calorimetry (DSC)

Differential scanning calorimetry is a technique to study the thermal events and phase transitions in a sample. However, calorimetric information like enthalpy (ΔH) and entropy (ΔS) changes can also be obtained and analyzed at phase transition temperatures.

The schematic diagram for DSC is shown in Fig. 2.3. In this technique, a pair of pans are used, one for the sample and another one for the reference kept empty. The separate heaters are located below both of the pans and these pans are heated with exactly same heating rates. However, at the phase transitions the sample either emits or absorbs heat. To maintain a constant heating rate, heater attached to a sample pan acts to deliver extra heat. This extra heat delivered to the sample is carefully measured. In other words, DSC scans measure the amount of energy absorbed/released during the phase transition by a sample. These DSC scans exhibit the exothermic and endothermic changes according to absorption or release of energy.

In the present investigations, Differential scanning calorimetry (SHIMADZU DSC-60) is principally used to examine the glass transition and crystallization kinetics. Measurements were also cross checked with another instrument (MDSC-2910, TA instruments).

The difference between the output of the two heaters (at a given temperature) is plotted as a function of temperature. This difference is a constant if same does not undergo a phase transition. A typical thermogram of a glassy sample is shown in Fig. 2.4. The glassy sample apparently exhibits glass transition (T_g), crystallization (T_c) and melting temperature (T_m).

As shown in Fig. 2.4, in the DSC patterns of a glass at glass transition (T_g), sample absorbs energy. Further at the onset of crystallization the sample starts releasing energy. For clarity Fig.

2.5 shows a typical exothermic crystallization peak. The onset is the crystallization temperature T_c , whereas, T_p represents the temperature where the rate of crystallization is maximum.

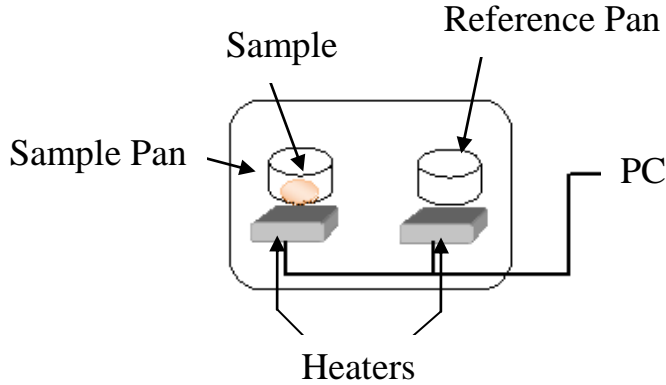


Fig. 2.3: Schematic diagram of a typical differential scanning calorimeter.

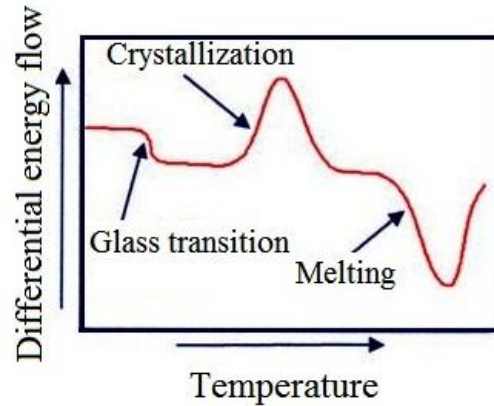


Fig. 2.4: A typical differential scanning calorimeter scan for glassy sample.

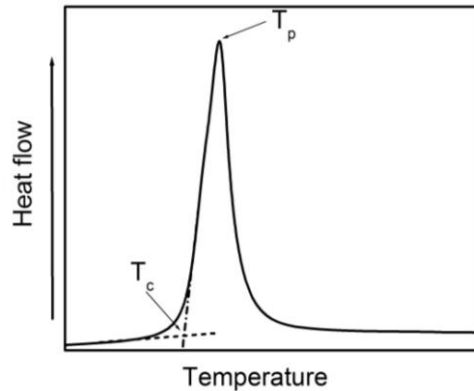


Fig. 2.5: A crystallization peak in a DSC curve at extended scale.

These experiments are performed in dry nitrogen atmosphere.

(a) Structural relaxation at glass transition temperature

The glass transition temperature (T_g) represents the temperature below which the molecular relaxation times are very large to establish equilibrium. Thus glass is in frozen viscous state below T_g . At T_g , there is decrease in the viscosity and system relaxes easily giving rise to rapid increase in the enthalpy and free volume. It is a thermodynamically reversible (more viscous ↔ less viscous state) transition.

Moynihan et al (1974) have given the following expression for the structural relaxation at T_g ;

$$\frac{d \ln q}{d(1/T_g)} = -\frac{E_s}{R} \quad (2.11)$$

where q is the heating rate, T_g the glass transition temperature, E_s the activation energy for structural relaxation and R the gas constant. Thus a plot of $\ln q$ versus inverse of T_g should be a straight line and the slope of this line leads to the activation energy for structural relaxation involved in the motion of structural units at T_g .

The significance of E_s is closely related to free volume change associated with T_g . At $T < T_g$, the system is highly viscous. For $T_g \leq T \leq T_c$, the viscosity decreases due to which the free volume increases. This increased free volume in the system providing pathways for ions. If the energy associated to structural relaxation increases, then an ion has to cross a comparatively higher energy barrier to overcome from the frozen viscous state. Thus, change in free volume decreases with increase in E_s .

Also, higher the activation energy for structural relaxation samples are relatively higher rigid, compact and mechanically stronger.

(b) Crystallization Kinetics

To study the thermodynamic aspects and thermal stability of the system, crystallization kinetics studies using DSC are very useful. There are two types of kinetics;

- (i) Isothermal crystallization kinetics: All the thermal stability parameters are measured at constant temperature well within the crystallization region ($T \geq T_c$).
- (ii) Non-isothermal measurements: DSC scans are performed at various heating rates to perform the non-isothermal measurements.

Thermal stability parameters viz., amorphous to crystalline transition temperatures (T_c), enthalpy (ΔH), activation energies for structural relaxation (E_s) and crystallization (E_c) and the order parameter (n), which will be discussed later in this section, of the crystallization process can be determined by both the measurements.

In present study we have used non-isothermal kinetics and DSC scans are measured at various heating rates to calculate all the thermal quantities. Thus non isothermal crystallization kinetics is discussed here in detail.

Generally, it is found that as we increase the heating rate, glass transition (T_g) and crystallization peak temperatures (T_p) shift towards high temperature monotonically. This observation gives rise to the theory of non isothermal kinetics.

Thus, Kissinger (1956, 1957) suggested that it is possible to calculate kinetics constants directly from DSC data by making a number of measurements at different heating rates. If α is the fraction of crystallized sample at a constant temperature T , the rate of crystallization (assuming the first order law is obeyed) is given by

$$\left(\frac{\partial\alpha}{\partial t}\right)_t = k_T(1-\alpha) \quad (2.12)$$

The magnitude of the rate constant k_T of the transformation has the following Arrhenius dependence on temperature.

$$k_T = Ae^{-\frac{E_c}{RT}} \quad (2.13)$$

Where R is the gas constant, T the temperature and A and E_c are constants that are properties of the material. The constant E_c , is known as the activation energy, and interpreted as the energy barrier opposing the crystallization reaction. When the temperature is changing with time, the reaction rate is given by

$$\frac{d\alpha}{dt} = \left(\frac{\partial\alpha}{\partial t}\right)_T + \left(\frac{\partial\alpha}{\partial T}\right)_t \frac{dT}{dt} \quad (2.14)$$

At a particular time the number and positions of the particles constituting systems are also fixed, thus

$$\left(\frac{\partial\alpha}{\partial T}\right)_t = 0 \quad (2.15)$$

So the total rate of the (crystallization) reaction according to Eqs. (2.5) and (2.6) may be expressed as

$$\frac{d\alpha}{dt} = A(1-\alpha)e^{-\frac{E_c}{RT}} \quad (2.16)$$

This expression holds for any value of temperature, whether constant or variable, so as long as α and T are measured at the same instant. When the reaction rate is maximum, its derivative with respect to time is zero, hence

$$\frac{d}{dt} \left(\frac{d\alpha}{dt} \right) = 0 \quad (2.17)$$

$$\frac{d}{dt} \left(A(1-\alpha)e^{-\frac{E_c}{RT}} \right) = 0 \quad (2.18)$$

At temperature $T = T_p$,

$$\frac{1}{(1-\alpha)} \frac{d\alpha}{dt} = \frac{E_c}{RT_p^2} \frac{dT}{dt} \quad (2.19)$$

The maximum value of $d\alpha/dt$ occurs at temperature T_p , defined by

$$Ae^{-\frac{E_c}{RT_p}} = \frac{E_c}{RT_p^2} \frac{dT}{dt} \quad (2.20)$$

If heating rate is given by q , then

$$q = \frac{dT}{dt} \quad (2.21)$$

So Eq. (2.20) can be written as,

$$\frac{d\left(\ln \frac{q}{T_p^2}\right)}{d\left(\frac{1}{T_p}\right)} = -\frac{E_c}{R} \quad (2.22)$$

Therefore, $\ln(q/T_p^2)$ versus $(1/T_p)$ should be a straight line whose slope governs the activation energy for crystallization (E_c).

$$\ln\left(\frac{q}{T_p^2}\right) = -\frac{E_c}{RT_p} + const. \quad (2.23)$$

However, the above equation does not signify anything about the mechanism of crystallization. Matusita and Sakka (1980) introduced a modified Kissinger equation, a more general form of Eq. (2.23),

$$\ln\left(\frac{q^n}{T_p^2}\right) = -\frac{mE_c}{RT_p} + Const. \quad (2.24)$$

Where q is the heating rate, T_p the peak temperature, E_c the activation energy of crystallization associated with the growth and nucleation, and m and n are dimensionality of crystal growth and the order parameter of the reaction (crystallization) respectively.

Since before the thermal analysis, no any heat treatment has been given to samples so dimensionality of growth m is taken to be equal to $n-1$ (Karmanov et al, 2001). The values of n and m infer about crystallization mechanism.

For $n = 4, 3, 2$ crystallization growth is 3, 2, 1 dimensional, respectively, whereas for $n = 1$ crystallization is surface nucleated (Matusita et al, 1981).

(c) **Alternative approach**

The activation energy associated with the growth and nucleation can also be evaluated using an alternative approach. When the glass is heated at a constant rate, crystal nuclei are formed at temperatures somewhat higher than the glass transition temperature and grow in size at higher

temperatures without any increase in number (Matusita and Sakka, 1979, 1980). If the number, N , of nuclei formed per unit volume in the course of heating from room temperature to some temperature T is expressed as

$$N = \frac{1}{q} \int_{T_r}^T I(T) dT = \frac{N_0}{q} \quad (2.25)$$

Where q is the heating rate and $I(T)$ is the nucleation rate. The radius, r of the crystallite is expressed as

$$r = \frac{1}{q} \int_{T_r}^T u_0 e^{-\frac{E_c}{RT}} dT \cong \frac{r_0}{q} e^{-\frac{E_c}{RT}} \quad (2.26)$$

Where $u = u_0 \exp(-E_c/kT)$ is the rate of crystal growth and E_c is the activation energy associated with growth and nucleation. The crystallization may occur in the bulk or on the surfaces. In case of bulk nucleation, each crystallite grows three dimensionally and the variation of the volume fraction, α , of the crystal is expressed as (Matusita et al, 1975).

$$\frac{d\alpha}{dt} = \frac{4N_0 r_0^2 u_0}{q^3} (1-\alpha) e^{-\frac{E_c}{RT}} \quad (2.27)$$

Integration of Eq. 2.27 approaches the following form

$$-\ln(1-\alpha) = \frac{K}{q^4} e^{-\frac{3E_c}{RT}} \quad (2.28)$$

Where, K is the constant.

In case of surface crystallization, nuclei are formed only on the surfaces and the crystals grow from the surface to the inside of the glass one dimensionally. Assuming the glass sphere of radius R_0 in which the surface layer of thickness r is crystallized, the volume fraction of the crystal is expressed as

$$1 - (1 - \alpha)^{1/3} = \frac{r}{R_0} = \frac{r_0}{qR_0} e^{-\frac{E_c}{RT}} \quad (2.29)$$

Excluding the region where x is close to unity, the following approximation can be used

$$1 - (1 - \alpha)^{1/3} \cong -\frac{1}{3} \ln(1 - \alpha) \quad (2.30)$$

Thus, following simplified expression can be derived

$$-\ln(1 - \alpha) = \frac{K'}{q^n} e^{-\frac{mE_c}{RT}} \quad (2.31)$$

Which can be further signified as

$$\ln(-\ln(1 - \alpha)) = -n \ln q - \frac{mE_c}{RT} + \text{const.} \quad (2.32)$$

Where α is the extent of crystallization, evaluated as the ratio of partial area of the exothermic peak up to temperature T to the total area of the peak and n is the order parameter. Thus the order parameter, also known as Avrami parameter (n), is calculated as

$$\frac{d(\ln(-\ln(1 - \alpha)))}{d(\ln q)} = -n \quad (2.33)$$

Similar expression is also proposed by Ozawa for calculation of n (Ozawa et al, 1970)

Moreover, according to Eq. 2.32, the plot of $\ln q$ versus inverse of peak temperature (T_p) should be a straight line with a slope of mE_c/nR .

The order parameter can also be calculated by other approach given by Augis and Bennett (1978);

According to Avrami equation, in the phase transformation process the amount of material transformed at a time t ,

$$x = 1 - e^{-(kt)^n} \quad (2.34)$$

Where n is Avarami parameter, k is reaction rate constant and given by,

$$k = \nu e^{-\frac{\Delta E}{RT}} \quad (2.35)$$

ν is frequency factor, ΔE activation energy, R is gas constant and T is temperature

$$T = T_0 + \alpha t \quad (2.36)$$

From Eq. (2.35) and (2.36),

$$kt = u = \nu t e^{-\frac{\Delta E}{R(T_0 + \alpha t)}} \quad (2.37)$$

So now Eq. (2.34) can be written as,

$$x = 1 - e^{-u^n} \quad (2.38)$$

and,

$$\dot{x} = \dot{u} n u^{n-1} (1-x) \quad (2.39)$$

$$\ddot{x} = (\ddot{u} u - u^2 (n u^n - n + 1)) n u^{n-2} (1-x) \quad (2.40)$$

From Eq. (2.37),

$$\dot{u} = \frac{u}{t} + a u \quad (2.41)$$

and,

$$\ddot{u} = u \left\{ \left(\frac{1}{t} + a \right)^2 - \frac{1}{t^2} \right\} \quad (2.42)$$

On substitution of Eqs. (2.40) and (2.41) in Eq. (2.42),

$$v^n e^{-n \frac{\Delta E}{RT_p}} = \left(\frac{T_p - T_0}{\alpha} \right)^{-n} \left\{ 1 - \frac{1}{n \left(1 + \frac{\Delta E}{R} \frac{T_p - T_0}{T_p^2} \right)} \right\} \quad (2.43)$$

where T_p is peak temperature for crystallization peak.

So in this case, if we plot $\ln \left(\frac{\alpha}{T_p - T_0} \right)$ versus $1/T_p$ then ΔE can be calculated.

Taylor expansion of Eq. (2.39),

$$\dot{x} = nbe^{nb\tau} e^{-e^{nb\tau}} \quad (2.44)$$

where,

$$b = \frac{\Delta E}{RT^2} \text{ and } \tau \text{ is measured from } T_p.$$

If Eq. (2.44) is plotted as $\frac{\dot{x}}{nb}$ versus $nb\tau$ then from the obtained graph it is clear that,

$$\Delta u = 2.5 = n \frac{\Delta E}{RT_p^2} \Delta T \quad (2.45)$$

$$n = \frac{2.5}{\Delta T} \frac{T_p^2}{\Delta E} R \quad (2.46)$$

The limitation of this technique is that it finds the average value of n for a complete process of crystallization. However, it can be very well used for complex systems to find n values.

Some other thermal stability parameters such as Hruby coefficient (k_{gl}) and Kauzmann temperature (T_{rg}) can also be calculated from using the formulations,

$$k_{gl} = \frac{T_c - T_g}{T_m^c - T_c}$$

where T_g and T_c are glass transition and crystallization temperature, respectively and T_m^c is the temperature of completion of melting .

2.4 Electrical characterization

The electrical conductivity measurements on ionic solids cannot be accurately performed with application of a dc voltage due to heterogeneous charge distribution (polarization) that further reduces the overall electrical conductivity of the system. It is not just the electrode electrolyte interface, but in a solid electrolyte, each interface polarizes in its unique way when the system is subjected to an applied potential difference.

Thus to measure the electrical conductivity in ionic solids ac voltage has been applied. The ac voltage gives rise to impedance spectroscopy. This impedance spectroscopy is a powerful method of characterizing many of the electrical properties of the materials. It may be used to investigate the dynamics of bound and mobile charges in the bulk or interfacial regions of any solid/liquid ionic materials.

2.4.1 Impedance spectroscopy

Generally, the electrochemical process represent through the combination of resistance (R), inductance (L), capacitance (C) and the component dependent on frequency (ω) (Sinclair et al 1989; Boukamp, 2001).

The complex impedance Z^* , at any frequency ω is given by

$$Z^*(\omega) = Z_R(\omega) + iZ_I(\omega) \quad (2.47)$$

or,
$$Z^* = |Z|e^{i\omega t} \quad (2.48)$$

where, $Z_R(\omega)$ and $Z_I(\omega)$ are the real and imaginary parts of the complex impedance (Z^*) respectively and the $|Z|$ is the magnitude of complex impedance and given by

$$|Z| = \sqrt{Z_R^2 + Z_I^2} \quad (2.49)$$

$$\text{Thus, electrical conductivity, } \sigma^* = \frac{l}{Z^* A} \quad (2.50)$$

Where l and A are length and cross sectional area of the sample, respectively. Using Eqs (2.39) and (2.41), conductivity is obtained as,

$$\sigma_R(\omega) = \left(\frac{l}{|Z|A} \right) \cos \theta \quad (2.51)$$

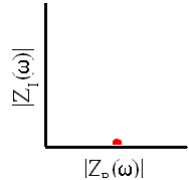
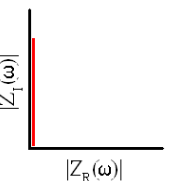
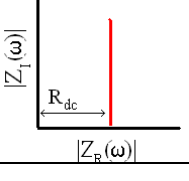
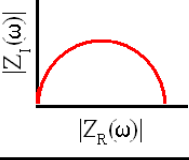
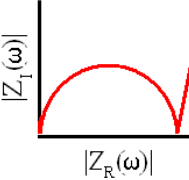
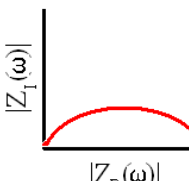
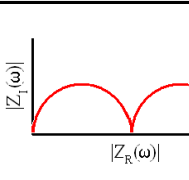
where θ , the phase angle is given by $\theta = \tan^{-1}(Z_I / Z_R)$.

If the sample behaves as a simple resistor then $Z_R(\omega) = R_{dc}$ and $Z_I(\omega) = 0$, and hence for this case,

$$Z^*(\omega) = |Z| \cos \theta + i|Z| \sin \theta = R_{dc} \quad (2.52)$$

Thus in this case, a plot of $Z_R(\omega)$ vs $Z_I(\omega)$ is just a point on the real axis. Similarly, if samples behave as different elements, different impedance plots can be obtained. Some of the typical impedance plots corresponding to different behavior of the electrochemical cell is given in Table 2.1.

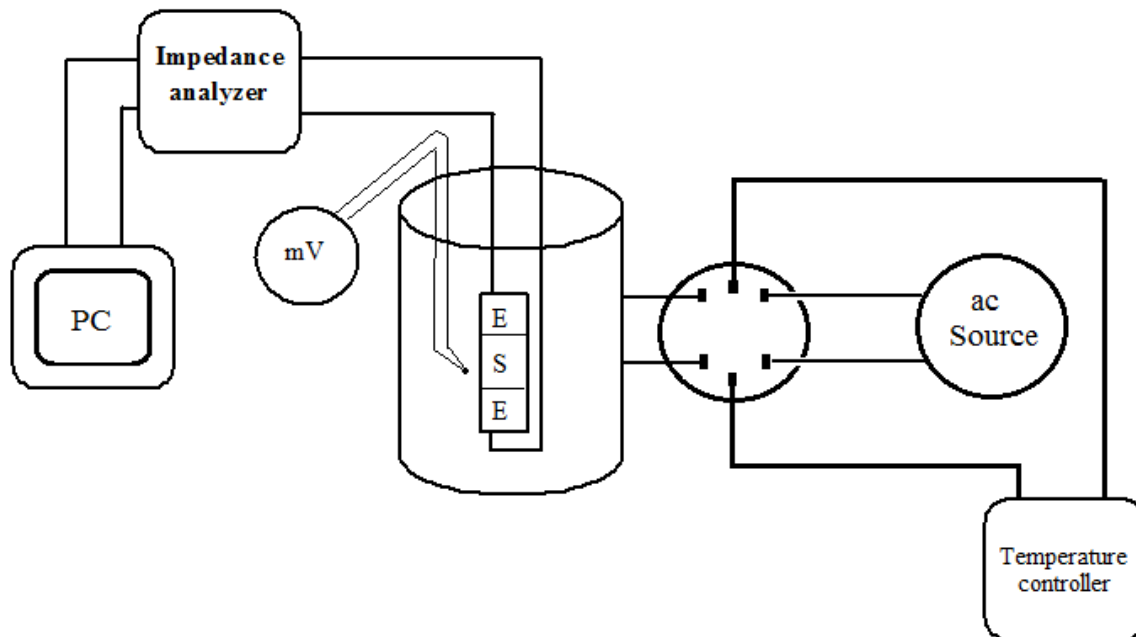
Table 2.1: Impedance plots corresponding to different combination of resistance and capacitor.

Behavior	$Z_R(\omega)$	$Z_I(\omega)$	$Z^*(\omega)$	Plot
Resistor	R_{dc}	0	R_{dc}	
Capacitor	0	$1/i\omega C$	$1/i\omega C$	
Series combination of R and C	R_{dc}	$1/i\omega C$	$R_{dc} + 1/i\omega C$	
Parallel combination of R and C	$\frac{R_{dc}}{1 + \omega^2 C^2 R_{dc}^2}$	$\frac{-\omega C R_{dc}^2}{1 + \omega^2 C^2 R_{dc}^2}$	$\left(Z_R - \frac{R_{dc}}{2}\right)^2 + Z_I^2 = \left(\frac{R_{dc}}{2}\right)^2 = Z_a$	
Parallel combination of R and C with C in series	Z_a	$1/i\omega C$	$Z_a^2 + 1/(i\omega C)^2$	
Parallel combination of R and constant phase element	R_{dc}	$A(2\pi i f)^{-n}$	$1/R_{dc} + 1/A(2\pi i f)^{-n}$	
2 (Parallel combination of R and C) in Series combination	Z_a	Z_a	$Z_a + Z_a$	

2.4.2 Electrical conductivity setup

Computer interfaced HIOKI 3532-50 impedance analyzer (42Hz-5MHz) was used to investigate the electrical conductivity. The measurements were carried out on cylindrical pellets. For better electrode and electrolyte contact, sample is pressed in the HCHC steel die in sandwich geometry, spreading fine powder of silver on both sides. These measurements of the electrical conductivity of the samples are carried out in the temperature range 25 – 200 °C using a cylindrical furnace.

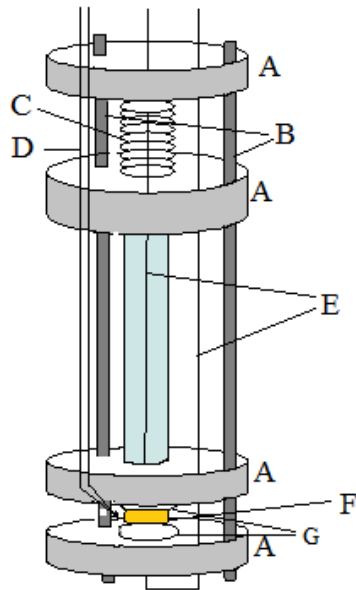
The setup used for electrical conductivity-temperature measurements is shown in Fig. 2.6. For the steady state measurements, the temperature is controlled by (PID) Libratherm programmable temperature controller PRC-309.



S: sample, E:silver electrode, k: chromel-Alumel thermocouple.

Fig. 2.6: Schematic diagram of electrical conductivity measurement setup (300K-1000K)

As shown in Fig. 2.7, the sample holder consists of identical lava and Teflon discs, silver electrodes and stainless steel supporting rods. The temperature of the sample was monitored using computer interfaced Rishcom multimeter and a chromel-alumel thermocouple.



A-Lava disk; B- Stainless steel rods; C- Pressure spring; D- Chromel Alumel thermocouple; E- Silver wires; F- Sample; G- Silver electrodes.

Fig. 2.7: Sample holder for electrical conductivity measurement (293K-500K)

2.5 Mobility measurements

Ionic mobility ($\text{m}^2/\text{V}\cdot\text{sec}$) is defined as the velocity attained by an ion moving through a solid under unit electric field. To measure the ionic mobility in solids transient ionic current (TIC) technique has been used (Watanabe et al, 1984) and set-up is shown in Fig. 2.8. The technique has been extensively developed and applied to glasses (Agrawal et al, 1994) and composites (Agrawal et al, 2011) as well.

In this technique ionic mobility was measured using direct current measurement on the electrolyte samples sandwiched between blocking electrode (graphite). A constant dc voltage is applied initially for 30 minutes in one direction. Subsequently the polarity of this current is reversed. The transient current versus time curve undergoes a peak. From the height of this peak the time of flight τ is obtained and using the formula ionic mobility is calculated.

$$\mu = \frac{d^2}{V\tau} \quad (2.53)$$

where d is the thickness of sample and V is the applied voltage. For a more reliable and correct result, μ is measured at different thickness of the samples.

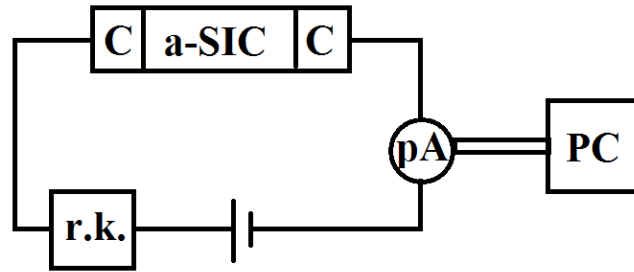


Fig. 2.8: Set up for mobility measurement. Where r.k. is the reversing key, pA is Keithley-6514 electrometer interfaced with PC.

2.6 Electrochemical cell characterization

The study of electrochemical behavior enables the understanding of the thermodynamic stability of the system. Secondly, it also evaluates the potential of the electrolyte for its possible application in solid state ionic devices. In the present study all the electrolyte (essentially glasses and glass-ceramics) samples were characterized by their electrochemical cell characteristics. The galvanic cells of the type $\text{Ag}|\text{sample}|\text{I}_2$ were fabricated, where anode was a mixture of Ag powder and the prepared glass and glass-ceramic samples (20 Ag + 80 Sample), while the cathode was a mixture of I_2 , prepared sample, graphite and tetra methyl ammonium iodide (TMAI). The weight ratio of the constituents kept $72\text{I}_2+25\text{C}+2\text{TMAI}+1\text{glass}$.

To achieve better electrode-electrolyte contact, anode material was first uniformly spread over the bottom of a HCHC die followed by a layer electrolyte (a-SiC). The two layers were then pressed at $\sim 2 \text{ tons/cm}^2$. The cathode powder was subsequently spread over the electrolyte and the three layers were compressed at $\sim 2 \text{ tons/cm}^2$. Thus obtained compact discs of diameter 11 mm, thickness $\sim 5\text{mm}$ and typical weight of 1.5-2g were sealed with polystyrene and packed in a Teflon case. The open circuit voltage and constant load characteristics have been carried out for all the electrochemical cells using Rishcom RS232 multimeter system interfaced with a PC. The typical set up is shown in Fig. 2.9.

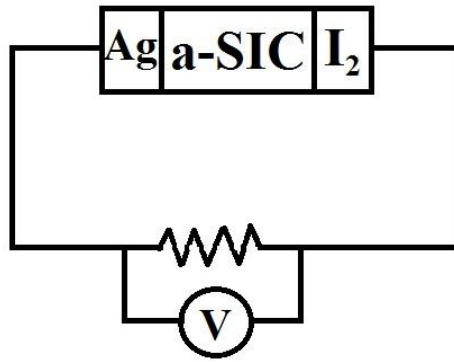


Fig. 2.9: Schematic presentation of electrochemical cell characterization set up

CHAPTER 3

CuI-AgI-Ag₂O-V₂O₅ SYSTEM: Effect of mixed alkali

This chapter describes the effects of mixed alkali (CuI substitution) on structural, electrical and electrochemical properties in AgI oxysalt glasses giving emphasis to thermal stability. As discussed earlier in section 1.6, fundamental system 50AgI-33.33Ag₂O-16.67V₂O₅ (50SISOVO) is doped with CuI. The compositions 50(Cu_xAg_{1-x})I-33.33Ag₂O-16.67 V₂O₅ for x=0.1, 0.15, 0.20, 0.25 and 0.30 (corresponding to 5, 7.5, 10, 12.5 and 15 m/o of CuI in AgI-Ag₂O-V₂O₅ system, respectively) were chosen well within the glass forming region and abbreviated as 10, 15, 20, 25, 30 and 40CI-SISOVO, respectively, for the present investigation.

The glass-ceramic composites of the same compositions are also prepared and characterized.

3.1. Structural investigations

3.1.1. X-ray diffraction

For the comparative study, X-ray diffraction (XRD) patterns for melt-quenched as well as for the 10 and 30CI-SISOVO samples annealed after melt quenching are shown in Fig. 3.1. Fig. 3.1 a and d show the patterns of as prepared glassy samples. Absence of any significant peak apparently confirms the glassy/amorphous nature of these samples. Further, the glassy samples are annealed above crystallization temperatures to investigate the precipitated compounds. The XRD results of 10 and 30 CI-SISOVO glassy samples annealed at 140°C (Fig. 3.1b and e) and at 170 °C (Fig. 3.1c and f)) are also shown. The annealing of 10CI-SISOVO sample at 140 °C results into major precipitation of two compounds, viz., Ag₄V₂O₇ and Ag₈I₄V₂O₇, as evident in Fig. 3.1b. Moreover, AgI also precipitates in small amount in this low CuI content sample. Interestingly, when the 10CI-SISOVO sample is further annealed at 170 °C (Fig. 3.1c), the intensity of the peaks corresponding to Ag₄V₂O₇ and AgI remain unchanged and that correspond to Ag₈I₄V₂O₇ appears to grow slightly. These results suggest that major precipitation of Ag₄V₂O₇ and AgI occurs at lower temperatures (~ 140 °C).

Nevertheless, crystallization of $\text{Ag}_8\text{I}_4\text{V}_2\text{O}_7$ also begins at lower temperatures but subsequently completes at relatively higher temperatures.

It may be suggested here that annealing of 10CI-SISOVO exhibits major precipitation of $\text{Ag}_4\text{V}_2\text{O}_7$ and AgI at low temperatures and that of the $\text{Ag}_8\text{I}_4\text{V}_2\text{O}_7$ compound whose precipitation also begins at low temperatures but is progressive and subsequently ends at somewhat higher temperature.

In case of the 30CI-SISOVO (high CuI content) sample, the XRD results suggest that on annealing, the overall precipitation of compounds is relatively small (Fig. 3.1 e and f).

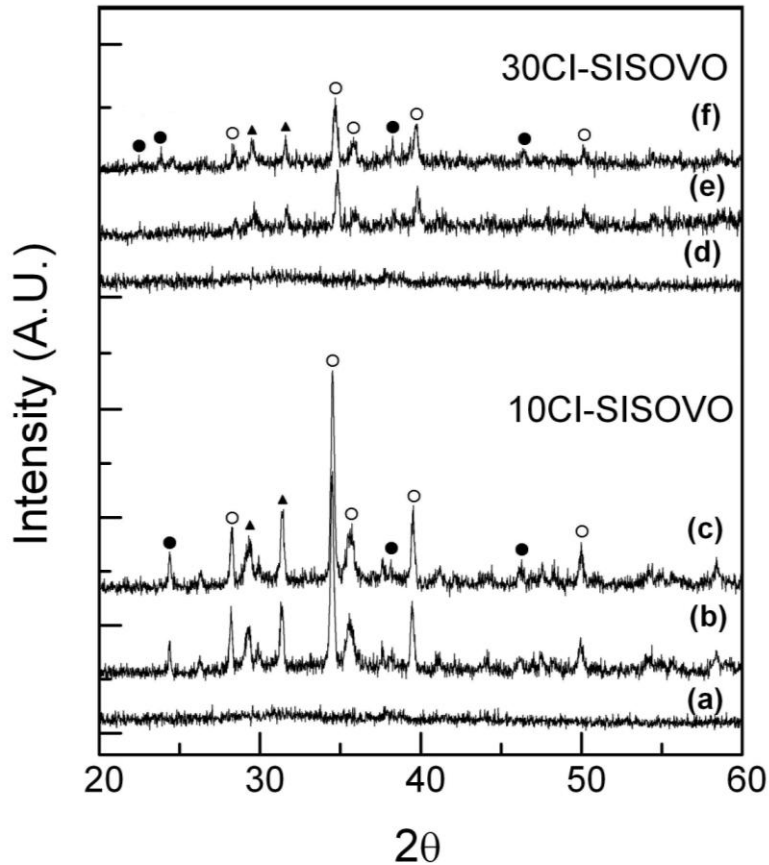


Fig.3.1: X-ray diffraction patterns for as prepared glasses (a and d), glassy samples annealed at 140 °C (b and e), and at 170 °C (c and f). Symbols denote (○) $\text{Ag}_8\text{I}_4\text{V}_2\text{O}_7$ (●) AgI (▲) $\text{Ag}_4\text{V}_2\text{O}_7$ peaks.

For the better understanding and clarity of precipitated compounds, XRD results are obtained for all the samples annealed at all the three crystallization temperatures and shown for one 30CI-SISOVO in Fig. 3.2. When the 30CI-SISOVO sample is annealed at 95 °C, there is a major precipitation of AgI and minor precipitation of $\text{Ag}_4\text{V}_2\text{O}_7$ and $\text{Ag}_8\text{I}_4\text{V}_2\text{O}_7$ compounds (Fig. 3.2a). On further annealing at 140 °C, there is small growth in the peaks corresponding to AgI and $\text{Ag}_8\text{I}_4\text{V}_2\text{O}_7$, whereas, major growth in those corresponding to $\text{Ag}_4\text{V}_2\text{O}_7$ compound. Thus AgI and $\text{Ag}_8\text{I}_4\text{V}_2\text{O}_7$ precipitates in small amount, whereas, $\text{Ag}_4\text{V}_2\text{O}_7$ in relatively larger amount. Further, when the sample is annealed at 170 °C, the peaks correspond to AgI and $\text{Ag}_4\text{V}_2\text{O}_7$ show no appreciable change, whereas, those correspond to $\text{Ag}_8\text{I}_4\text{V}_2\text{O}_7$ grow significantly. It may be suggested here that though the simultaneous precipitation begins at $T \leq 100$ °C, the first major precipitation is that of AgI (~ 94 °C). Further heating leads to crystallization of $\text{Ag}_4\text{V}_2\text{O}_7$ and $\text{Ag}_8\text{I}_4\text{V}_2\text{O}_7$ compounds at respective higher temperatures of ~ 140 °C and 170 °C.

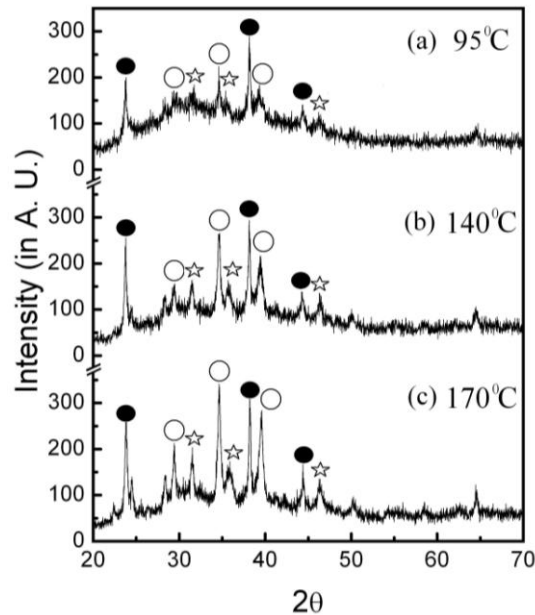


Fig.3.2: X-ray diffraction patterns for glass-ceramic samples obtained at various crystallization temperatures. Symbols denote: (○) $\text{Ag}_8\text{I}_4\text{V}_2\text{O}_7$ (●) AgI (☆) $\text{Ag}_4\text{V}_2\text{O}_7$ peaks.

Thus it may be concluded here that (i) in both (low and high CuI content) samples, crystallization occurs with precipitation of multiple phases, (ii) addition of CuI reduces the formation of the two compounds (viz., $\text{Ag}_4\text{V}_2\text{O}_7$ and $\text{Ag}_8\text{I}_4\text{V}_2\text{O}_7$) in glass-ceramics and (iii)

silver iodide precipitates in both the compositions. X-ray diffraction results for the other compositions do confirm glassy nature of the samples. It is observed that the AgI–Ag₂O–V₂O₅ system dissolves CuI at least up to 17.5 m/o (corresponding to x=0.35, viz, 35CI-SISOVO).

The average particle size of the precipitated crystallites during annealing, calculated using Debye - Scherer formula, is found to be ~ 20-50 nm for all the compositions.

3.1.2. Scanning electron Microscopy

SEM images are obtained for glassy samples as well as glass-ceramics (i.e. glassy samples annealed at various crystallization temperatures).

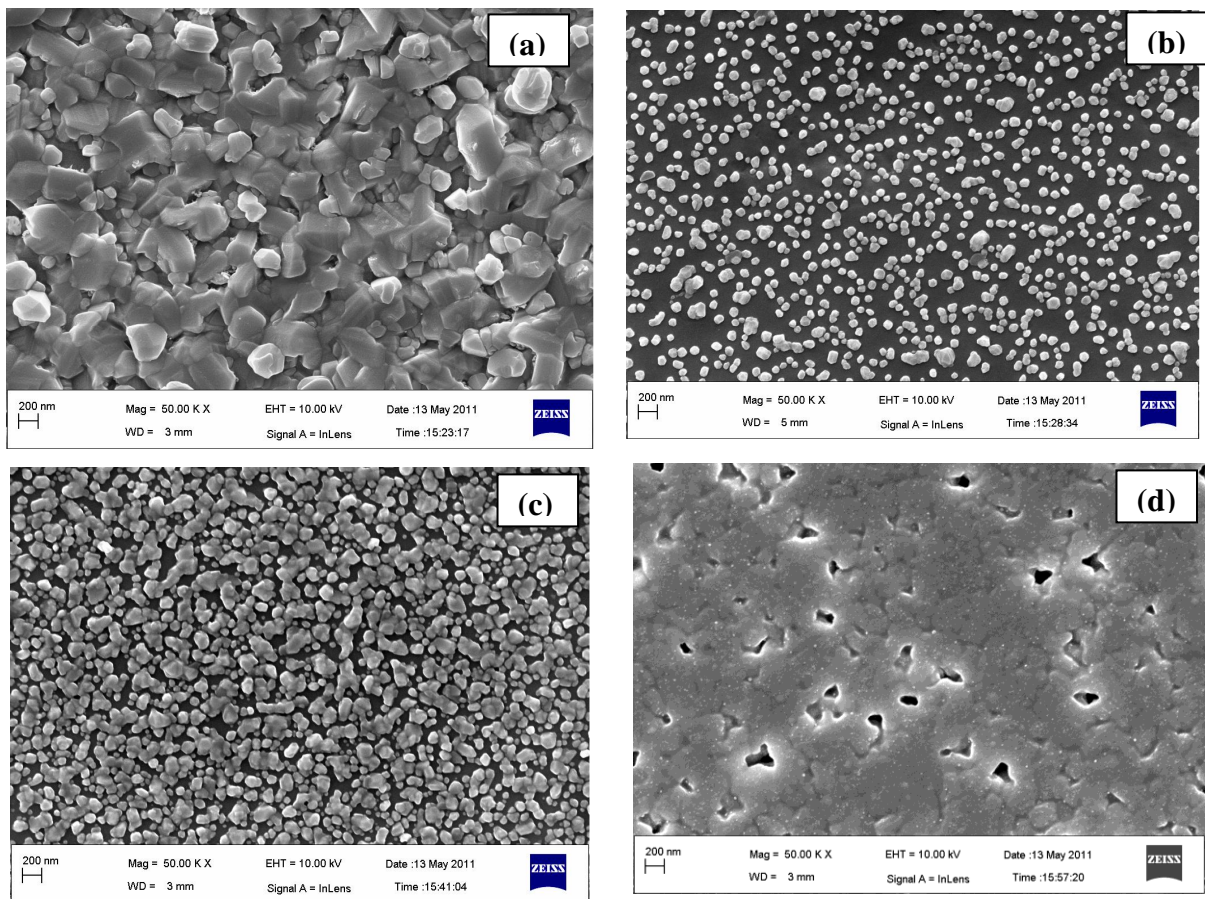


Fig: 3.3: Scanning electron microscopy images for 30CI-SISOVO (a) as prepared glass, sample annealed at (b) 90 °C (T_{c1}), (c) 140 °C (T_{c2}) and (d) 170 °C (T_{c3}).

Fig. 3.3a exhibits a flake like homogeneous structure for glassy samples even at a high resolution of 200nm. SEM images of the glassy films annealed at various temperatures are

shown in Fig. 3.3 b-d. Again, it is revealed from these images that there is some uniform growth of tiny crystallites in the samples annealed at 90 °C (Fig. 3.3 b). Majority of these crystallites may be that of AgI as also revealed by XRD. Moreover, in the sample annealed above 140 °C (T_{c2}) there is subtle but significant growth in the number of uniform crystallites embedded in the glass matrix (Fig. 3.3 c). It is readily noted that there is existence of fine crystallites/particles of size ~ 20-200 nm. When these samples annealed above the complete crystallization, there is a noticeable growth in these precipitated particles (Fig. 3.3 d) which in turn, tends to form a polycrystalline structure.

3.2. Differential Scanning calorimetry

The results of DSC are shown in Fig. 3.4 for 10, 15 and 30CI-SISOVO samples for a typical heating rate of 10 °C/min. The heating cycles for the glass-ceramic samples are also shown. In the DSC scans for all the as prepared glassy samples (Fig. 3.4a, c and e), there appear an endothermic smooth dip in 60–75 °C range that correspond to respective glass transition temperature (T_g) of these samples. Apparently, all the samples are glassy in nature. The T_g shows a decrease with CuI content.

Fig. 3.4a shows the DSC pattern for 10CI-SISOVO melt-quenched sample. For this, there appears a broad exothermic crystallization peak with rise (T_c) at ~113 °C, that may be visualized as two merged up exothermic peaks having maximum at ~128 (T_{p1}) and ~148 °C (T_{p2}). For the 15CI-SISOVO sample (Fig. 3.4c), similar merged up peaks appear to begin at ~107 °C and have first crystallization peak T_{p1} at ~135 °C and T_{p2} at ~154 °C. The DSC scans for 30CI-SISOVO are shown in Fig. 3.4e and f. Here the patterns are found to be significantly different from those of the 10 and 15CI-SISOVO samples. In the first cycle, first major exothermic peak appears to begin at ~107 °C and ends at the ~120 °C followed by another small exothermic peak at ~140 °C. On further heating, a small endothermic dip appears at ~150 °C that may correspond to characterization $\beta \rightarrow \alpha$ phase transition of AgI.

In the heating cycle of glass-ceramic samples no significant thermal event is seen in case of 10CI-SISOVO (Fig. 3.4b), whereas, for 15 and 30CI-SISOVO a small endothermic dip appears at ~147 °C (Fig. 3.4 d and f) exhibiting the presence of AgI that may have precipitated during the crystallization. The DSC results suggest that there are at least three compounds that

precipitate at T_{p1} and T_{p2} for low CuI content samples. The crystallization of these compounds may be simultaneous, however their respective maximum rates of crystallization (appear at T_{p1} and T_{p2} , respectively) are significantly different. For low CuI content samples, T_{p1} and T_{p2} may correspond to precipitation of $Ag_4V_2O_7+AgI$ and $Ag_8I_4V_2O_7$, respectively.

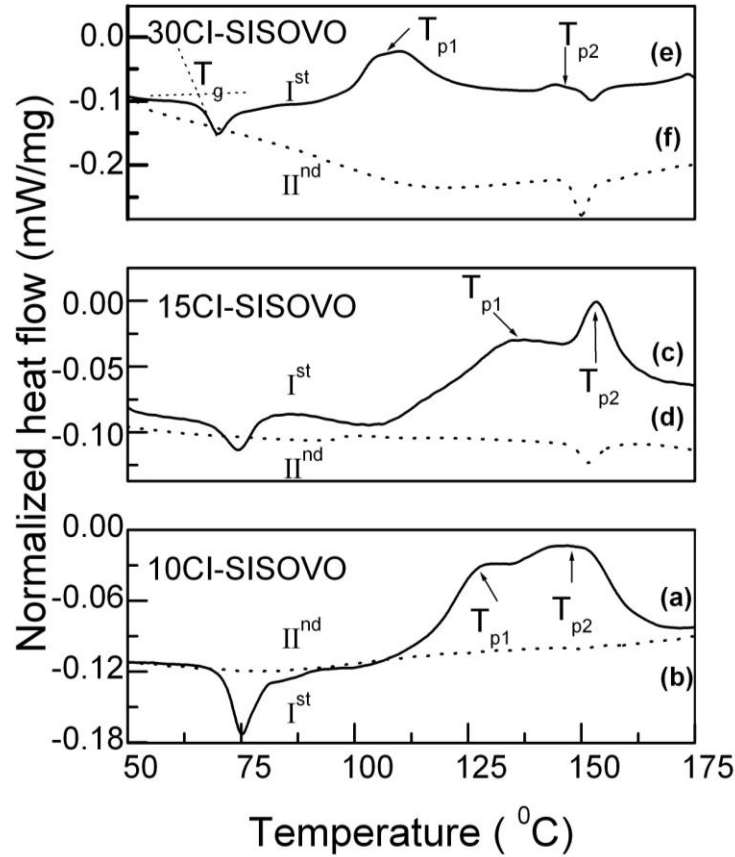


Fig. 3.4: DSC scans for different compositions of CI-SISOVO (I^{st}) glassy and (II^{nd}) annealed glassy samples.

Further, it is important to note that the higher CuI content samples (e.g. 30CI-SISOVO) again exhibit major precipitation of at least two compounds with maximum crystallization rate at T_{p1} and T_{p2} , respectively. In this case at T_{p1} , there is a major precipitation of AgI along with minor precipitation of $Ag_4V_2O_7$. Further, at T_{p2} precipitation of $Ag_8I_4V_2O_7$ is expected. Apparently, the XRD and DSC results are in good agreement with each other.

For the further understanding of thermal events in the samples within the glass forming region, the parameters defining the thermal stability of glassy system are obtained from DSC

plots and given in Table 3.1. The total enthalpy release (ΔH) in the samples during crystallization is calculated from the total area under the exothermic peak. The value of ΔH found to be decreasing with CuI content clearly suggests that CuI substitution in the SISOVO matrix suppresses the crystallization. Similarly, other thermal stability parameters, e.g., T_c , T_g , $T_c - T_g$, T_{rg} and T_g/T_m also consistently decrease with CuI content. Interesting to note that precipitation of $Ag_8I_4V_2O_7$ reduces with CuI addition. It may be due to the fact that the added CuI reacts with Ag_2O introducing Cu_2O in the glass matrix. Thus the Ag_2O deficiency in the matrix may reduce the $Ag_8I_4V_2O_7$ and $Ag_4V_2O_7$ formation in the glass.

Table 3.1: Characteristics temperatures and total enthalpy release during crystallization in the CI-SISOVO system.

X	ΔH (J/g)	T_c ($^{\circ}C$)	T_g ($^{\circ}C$)	$T_{rg} = T_g/T_m$	$T_c - T_g$ ($^{\circ}C$)
0.10	20 ± 0.40	110	70	0.37	40
0.15	19 ± 0.38	102	65	0.34	37
0.20	18 ± 0.36	96	62	0.32	34
0.25	14 ± 0.28	94	61	0.30	33
0.30	10 ± 0.20	92	60	0.29	32

The above discussion (precipitation of different compounds at different temperature) further suggests that for low CuI content samples there may be at least three types of Ag^+ ions surrounded by different environments. The first type of Ag^+ ions may be surrounded by V–O units, whereas, the second type of Ag^+ ions surrounded by V–O along with I– units. There is also a possibility of a third type of Ag^+ ion that may be surrounded by I– ions alone. Such surrounding of Ag^+ ions may be facilitate the precipitation of three compounds, viz., $Ag_4V_2O_7$, AgI and $Ag_8I_4V_2O_7$ during the crystallization.

To study the kinetics, DSC scans have been performed on all the as prepared glasses at various heating rates (5-20 °C/min) and shown in Fig. 3.5 for one of the samples viz., 10CI-SISOVO.

As evident, there is a broad crystallization peak with two clear kinks. On further heating no exothermic peak appears till melting temperature ($T_m \sim 200$ °C). The T_g and T_p (crystallization peak temperature) found to be shifting monotonically towards the higher temperatures as heating rate increases. Since the XRD studies suggest precipitation of at least three compounds, the three merged up peaks can be fit well within this broad peak as shown in Fig. 3.5. These fitted peaks are shown by dotted lines and correspond to formation of AgI, $Ag_4V_2O_7$ and $Ag_8I_4V_2O_7$ compounds, respectively.

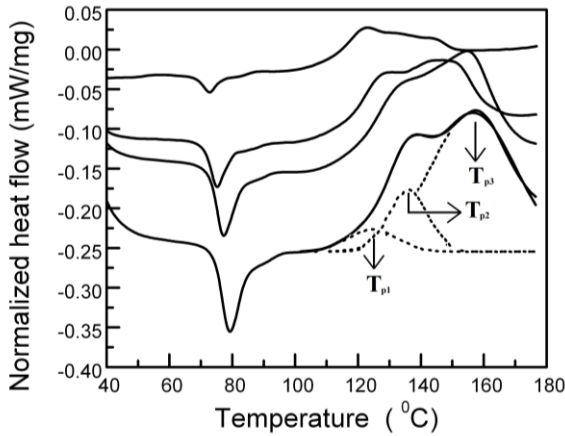


Fig. 3.5: DSC scans at various heating rates for 10CI-SISOVO sample. T_{p1} , T_{p2} and T_{p3} correspond to major precipitation of AgI, $Ag_4V_2O_7$ and $Ag_8I_4V_2O_7$, respectively.

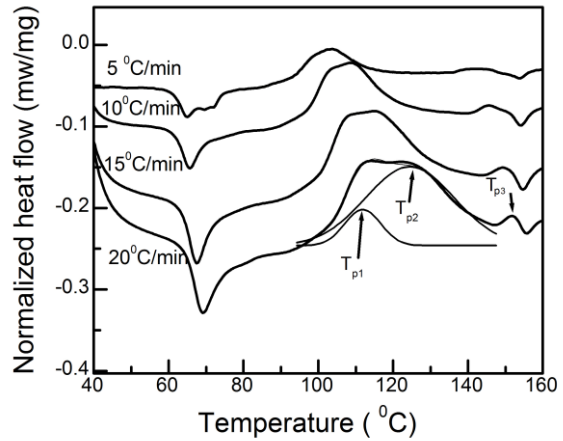


Fig. 3.6: DSC scans at various heating rates for 30CI-SISOVO sample. The peaks correspond to T_{p1} : AgI, T_{p2} : $Ag_4V_2O_7$ and T_{p3} : $Ag_8I_4V_2O_7$.

Likewise, Fig. 3.6 shows the DSC scans of 30CI-SISOVO at different heating rates. Since, CuI content in the sample is higher, thus the trends for this sample is notably dissimilar to that of 10 CI-SISOVO as discussed and witnessed earlier. There appears one broad peak onset at ~ 100 °C with two kinks followed by a well separated small but significant exothermic peak at $T \sim 160$ °C. The first two merged-up peaks thus may correspond to precipitation of AgI and $Ag_4V_2O_7$. In addition, presence of third small but significant peak is attributed to that of $Ag_8I_4V_2O_7$ precipitation.

3.2.1. Glass transition and crystallization kinetics

Following to Eq. 2.2, the plot of $\ln(q)$ versus inverse of temperature (T_g) for 10 and 30 CI-SISOVO samples is shown in Fig. 3.7. Apparently, the plot is linear and E_s values for compositions within glass forming region are obtained from the slope of $\ln q$ vs inverse of T_g , and plotted as a function of CuI content in Fig. 3.8. Clearly, the E_s value is found to be decreasing as a function of CuI content. Interestingly, E_s value exhibit a decreasing trend with CuI content. Thus, it may be suggested that the energy required for structural units to overcome the frozen viscous state at T_g decreases with CuI addition. It may also be inferred from Fig. 3.8 that system exhibits a viscosity that decreases at T_g when CuI content is increased.

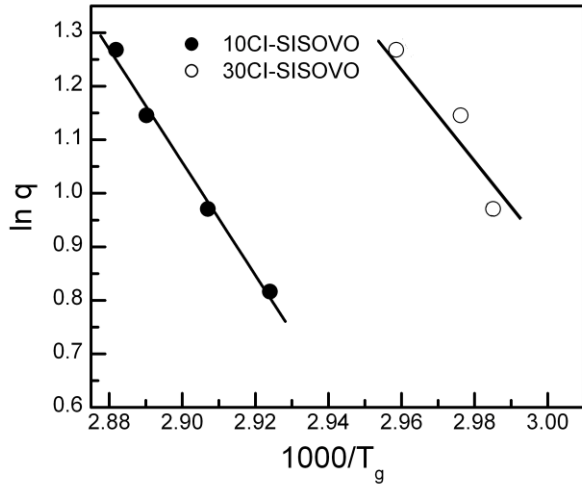


Fig. 3.7: $\ln q$ versus inverse of temperature for 10 and 30CI-SISOVO

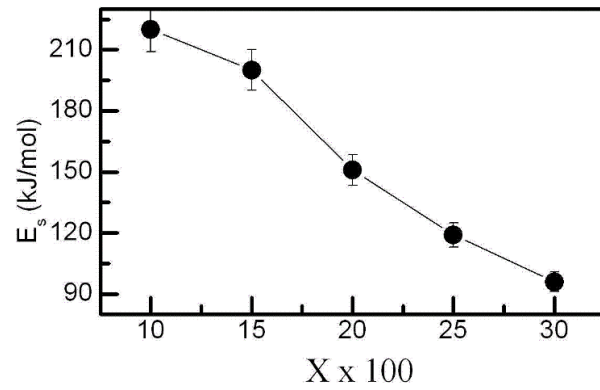


Fig. 3.8: The activation energy for structural relaxation at T_g as a function of CuI content in CI-SISOVO

As discussed earlier that CuI addition increases the Cu_2O amount that, in turn, decreases the Ag_2O content in glass matrix as per the following reaction suggested by various workers (Hariharan et al, 1992; Murugesan et al 2007)



Thus, it may also be stated here that essentially it is the Cu_2O substitution that reduces the E_s value.

In Fig. 3.9 a and b, $\ln(q/T_p^2)$ versus inverse of T_p are plotted for the 10 and 30CI-SISOVO samples, respectively. The three peak temperatures (T_p) in the DSC scans are, respectively,

attributed to precipitation of three compounds. Therefore, the E_c values for T_{p1} , T_{p2} and T_{p3} are mainly attributed to precipitation of AgI, $Ag_4V_2O_7$ and $Ag_8I_4V_2O_7$ compounds, respectively. The plots are apparently linear and thus E_c values are obtained using Eq. 2.14 for different compositions and these are plotted as a function of CuI content in Fig. 3.10.

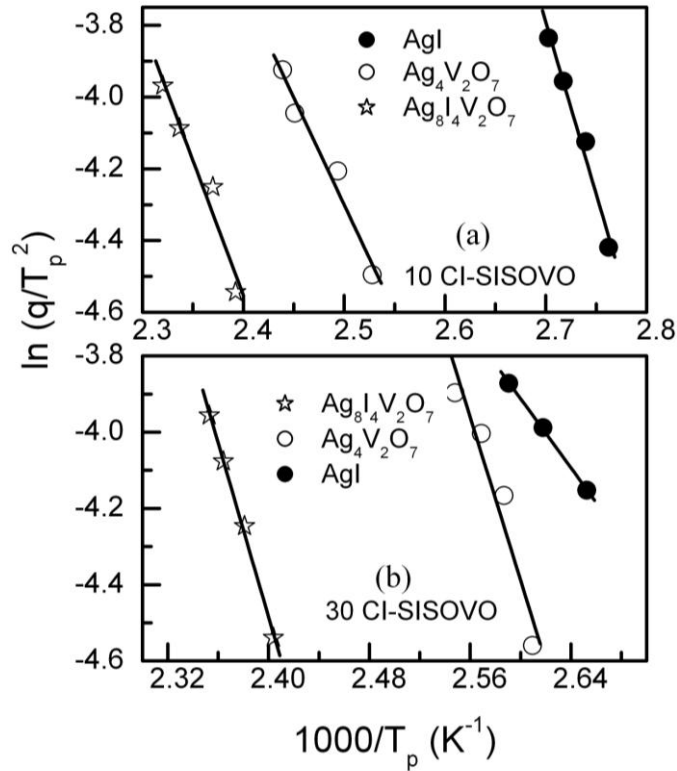


Fig.3.9: Modified Kissinger plot for (a) 10CI-SISOVO sample and (b) 30CI-SISOVO sample.

The E_c values corresponding to crystallization of AgI in the samples remain almost constant for low CuI content and exhibits a decreasing trend with increasing CuI content in the glass matrix (Fig. 3.10 a). These results suggest that higher CuI content reduces the energy barrier for crystallization of AgI. Thus, it is expected that AgI precipitation should be facilitated with CuI substitution. These results are in good agreement with DSC second heating cycles where area under endothermic dip at 147 °C exhibits a subtle but significant increase.

Likewise, Fig. 3.10 b and c show the variation of E_c for $Ag_4V_2O_7$ and $Ag_8I_4V_2O_7$ as a function of CuI content, respectively. These E_c values show systematic rise with CuI content. It may be suggested here that the energy barriers for crystallization of $Ag_4V_2O_7$ and

$\text{Ag}_8\text{I}_4\text{V}_2\text{O}_7$ become more prominent with CuI content in the samples that in turn gives rise to suppressed precipitation of these compounds.

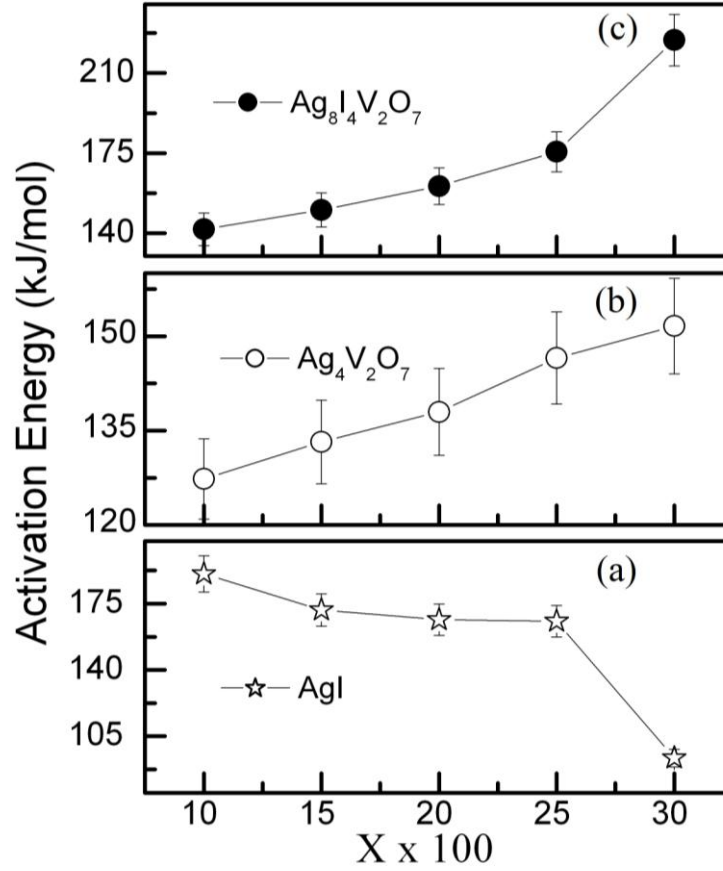


Fig.3.10: The E_c values (obtained from Eq. (2)) as a function of CuI content.

Using the Eq. (2.32), the Avrami parameter (n) is obtained for all the compositions ($x= 0.1-0.3$). Since in most cases of the system one gets merged-up crystallization peaks in the DSC patterns. The value of n is calculated using multiple Gaussian fitting on these exothermic peaks. Symmetric Gaussian peaks obtained after the fitting are used to calculate ΔT for individual precipitations. For all the compositions (10-30CISISOVO) at various rates (5-20 $^{\circ}\text{C}/\text{min}$), value of n is calculated and found to be almost near unity. It may be suggested here that the crystallization in these samples occurs with surface nucleation (Kissinger, 1956).

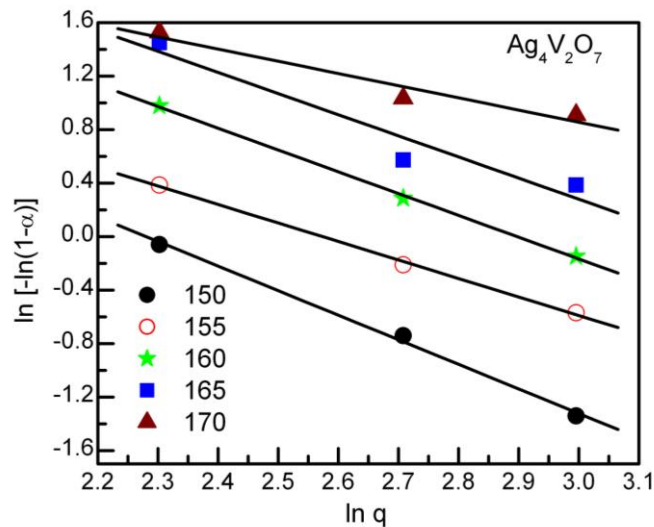


Fig. 3.11: $\ln(-\ln(1-\alpha))$ versus $\ln q$ for 10CI-SISOVO sample for the crystallization of $\text{Ag}_4\text{V}_2\text{O}_7$.

As reported in various studies (Dalvi et al, 2003; Tiwari et al 2009) temperature dependence of n can also be obtained using Eq. 2.46. Thus, we have calculated the temperature dependence of n for this complex glassy system. For this, $\ln[-\ln(1-\alpha)]$ versus $\ln q$ has been plotted and shown for crystallization of $\text{Ag}_4\text{V}_2\text{O}_7$ in 10CI-SISOVO sample (Fig. 3.11). The n values obtained from the slope (Fig. 3.11, Eq. 2.24) are given in Table 3.3. It is interesting to note that these do not show any particular trend with temperature and found to be comparable to those of obtained from Augis-Bennett method. Similar comparable values of n obtained from both methods are also reported in other studies as well (Karamanov et al, 2008). Qualitatively, the crystallization mechanism can also be understood from the width of the exothermic peak. Wide crystallization peak generally refers to the surface crystallization within the samples, whereas, the sharp peak infers about the bulk crystallization (Reynoso et al 2003). Thus, it may be concluded here that overall crystallization in these samples is dominated by surface nucleation.

Table 3.2: The Avrami parameter calculated by Augis - Bennett relation at various rates as a function of CuI content (5-20 °C/min) for the crystallization of three different compounds viz., AgI, Ag₄V₂O₇ and Ag₈I₄V₂O₇.

x	Heating rate (q)	n		
		Peak 1 (AgI)	Peak 2 (Ag ₄ V ₂ O ₇)	Peak 3 (Ag ₈ I ₄ V ₂ O ₇)
0.1	5	1.01	1.08	0.89
	10	1.14	1.38	0.88
	15	0.88	0.81	1.07
	20	0.99	1.18	0.95
0.2	5	1.04	1.03	0.94
	10	0.96	1.02	1.13
	15	1.03	1.01	1.15
	20	0.99	0.98	0.3
0.3	5	1.22	0.98	1.01
	10	0.98	1.01	1.38
	15	1.38	0.95	2.04
	20	1.62	0.88	2.06

Table 3.3: The Avrami parameter calculated by Matusita Sakka equation as a function of temperature.

Peak 1		Peak 2		Peak 3	
Temperature (°C)	n (±1%)	Temperature (°C)	n (±1%)	Temperature (°C)	n (±1%)
114	1.85	125	1.32	150	1.75
118	0.88	130	1.12	155	1.38
122	0.95	135	0.82	160	1.62
126	1.02	140	1.54	165	1.57
130	0.77	145	0.83	170	0.91

3.3. Electrical conductivity

At the outset, the ionic nature of all the samples is confirmed by galvanic cell method using the following relation

$$t_+ = \frac{V_{observed}}{V_{calculated}} \quad (3.2)$$

Using Eq. 3.2 the ionic transport number is found to be near unity for all the samples. In view of structural and thermal studies, which revealed precipitation of various compounds during crystallization, the electrical conductivity is also studied above the T_g and T_c , i.e. in the metastable regions, for various compositions. The electrical conductivity (1 kHz) versus temperature measured (for glass and glass-ceramic samples) at a typical heating rate of 1 °C/min is shown in Fig. 3.12. The conductivity-temperature cycles for 10, 15 and 30 CI-SISOVO glasses (Fig. 3.12a, c and e) and glass-ceramics (Fig. 3.12 b, d and f) reveal interesting results that are divided in three regions for clarity.

The conductivity in region I increases with temperature for all the glassy samples and follows Arrhenius behavior. These cycles are reversible at least up to 65–70 °C ($T \leq T_g$). The activation energy for ionic conduction is found to be ~0.15-0.25eV for all these glassy samples.

For the 10CI-SISOVO sample (Fig. 3.12 a) above the glass transition temperature ($T_g \sim 65$ °C) and prior to crystallization temperature ($T_c \sim 110$ °C), the conductivity (region II) increases at appreciably faster rate and deviates significantly from linear behavior. On further heating, the conductivity shows a notable drastic fall and saturates, subsequently. Furthermore, on heating it again increases Arrheniusly (region III). It may be stressed here that fall in the conductivity corresponds to beginning and saturation to that of completion the crystallization process.

The σ - T characteristics of 15 and 30CI-SISOVO (Fig. 3.12 c and e, respectively) are rather dissimilar to that of 10CI-SISOVO sample (especially in region II and III). For the 15CI-SISOVO sample conductivity exhibits a little deviation from the Arrhenius behavior at T_g and on further heating a slight fall near T_c . Subsequently, conductivity attains a plateau for a small temperature range and further increases linearly with temperature. Further, the σ - T behavior

for 30CI-SISOVO (Fig. 3.12 c) exhibits no significant deviation from Arrhenius behavior at T_g , though a plateau like region is apparent in the vicinity of T_c that may be an indication of smaller and slower crystallization.

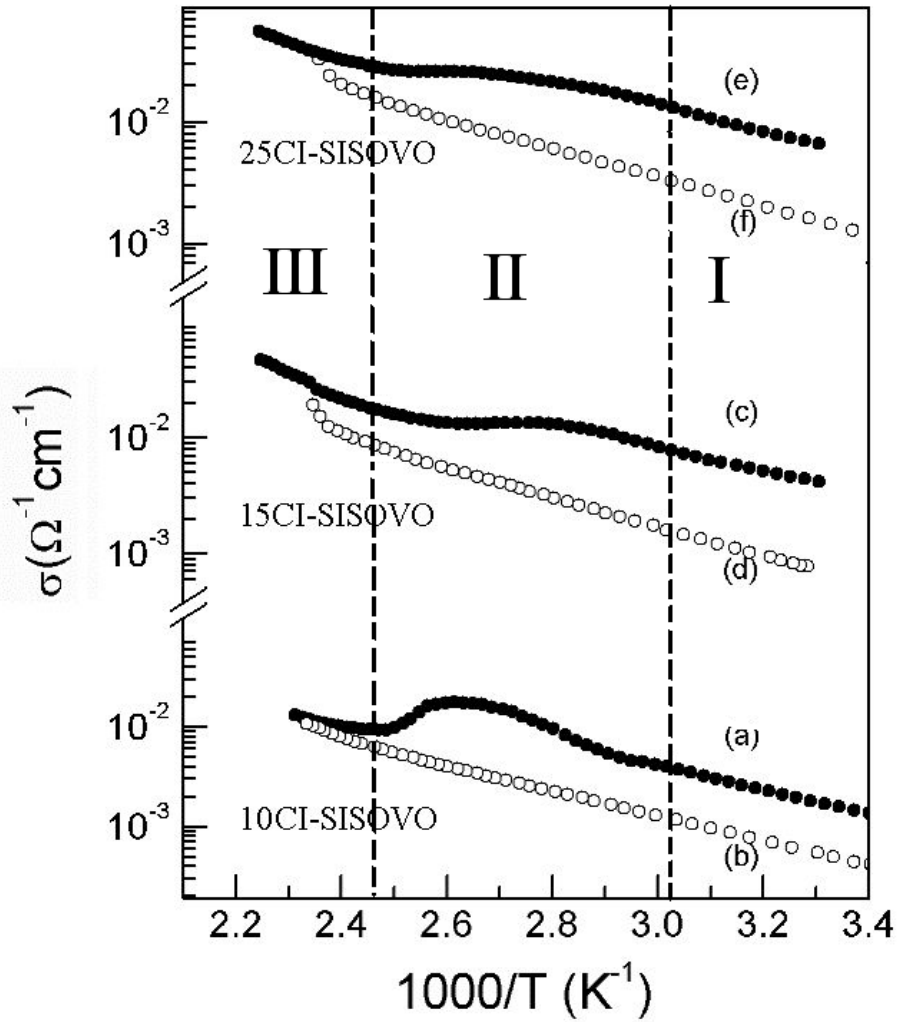


Fig. 3.12: Electrical conductivity as a function of inverse of temperature at a typical heating rate of $1^\circ\text{C}/\text{min}$. Symbols denote: (●) first and (○) second heating

Earlier structural studies on glassy (Adams et al, 1996) and mechanochemically synthesized (Dalvi et al, 2004) $\text{AgI-Ag}_2\text{O-V}_2\text{O}_5$ systems have confirmed that precipitation of $\text{Ag}_8\text{I}_4\text{V}_2\text{O}_7$ affects the conductivity very significantly and is indeed responsible for its sharp fall at T_c .

To clearly visualize the conductivity behavior in thermally unstable region II, for $T_g \leq T \leq T_c$ and $T \geq T_c$, the conductivity as a function of temperature has been replotted for 50SISOVO (that contains no CuI) and 10, 15CI-SISOVO samples in Fig. 3.13.

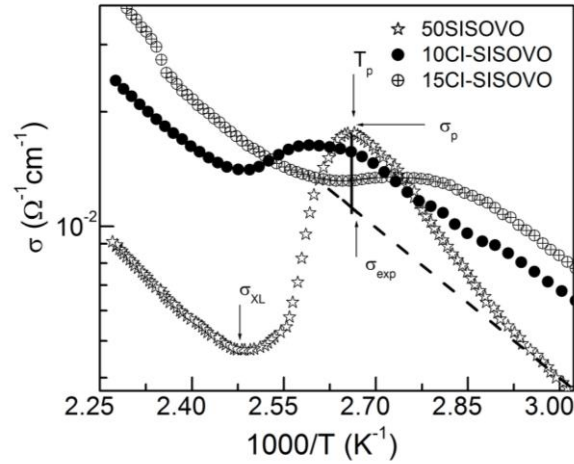


Fig. 3.13: Electrical conductivity - temperature plot on an extended scale. Conductivity at peak (σ_p), after crystallization (σ_{XL}) and extrapolated at peak temperature (σ_{exp}) are shown for 50 SISOVO, 10CI-SISOVO and 15CI-SISOVO samples.

As noticed, the fall in the conductivity above the crystallization temperature apparently depends on the CuI content in the samples. For 15CI-SISOVO, at T_c fall in the conductivity is drastically small, whereas, for $x=0.3$ only a plateau is seen in σ - T plot (Fig. 3.13) with no further fall in the conductivity near T_c . Thus, as the CuI content increases, fall in the conductivity at crystallization decreases. For low CuI content samples, on the completion of crystallization, conductivity attains a constant value of σ_{XL} and further found to be increasing Arrheniusly with the temperature.

This behavior of the electrical transport (region II) can be very well explained by a crystallite bypass model inspired by cluster bypass model. When the glass is heated well above T_g , stable nucleation begins (Fig. 3.14a and b). The ions contributing in the transport bypass these stable nuclei. Thus the glass for the temperatures $T_g < T < T_c$ undergoes a transformation into glass-ceramic nanocomposite that can be thought of tiny crystallites surrounded by/embedded into connective tissues of matrix. If the crystallization process is growth dominated, these nuclei on further heating grow in size as well, and at crystallization (T_c) block all the

connective tissues of the glass matrix. There is another possibility when the process of crystallization is nucleation dominated. In this, the number of stable nuclei formed well above the T_g grow till the end of the crystallization process. In any case, at $T = T_c$ the ions cannot bypass these crystallites and now move through them. Finally, the ionic structure of these nanocrystallites dictates the electrical transport and its behavior at T_c .

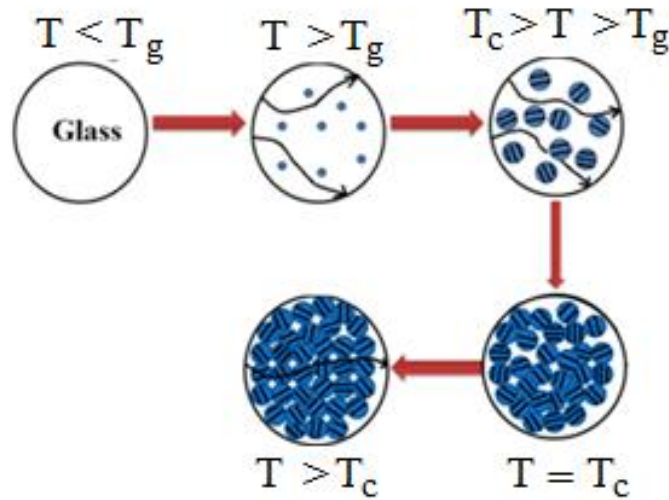


Fig. 3.14a Crystallite by pass model to understand the conductivity behavior during crystallization (for nucleation dominated crystallization process)

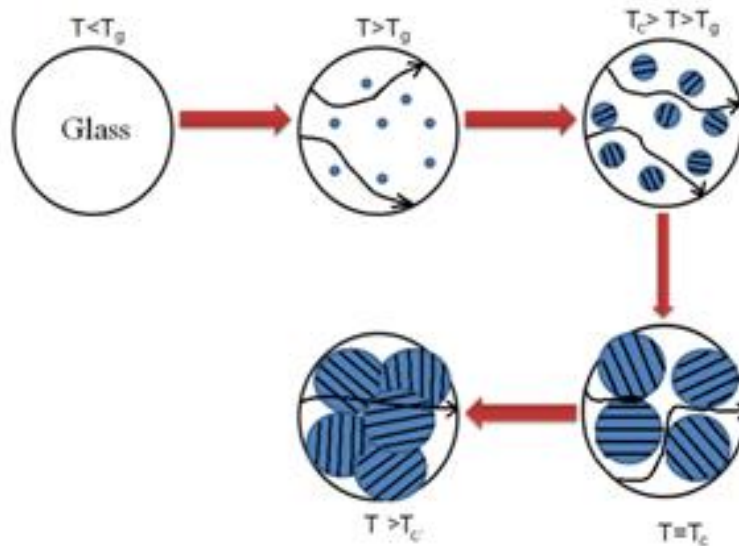


Fig. 3.14b Crystallite by pass model to understand the conductivity behavior during crystallization (for growth dominated crystallization process)

If the electrical conductivity of the crystallites is comparable to that of the connective tissue,

the conductivity may deviate but will exhibit no drop. However, if the conductivity of the crystallites is poor than that of the tissue, a drastic fall in its value is expected. Further, it may be emphasized here that if the conductivity of crystallites is higher than that of the tissue (for example α -AgI like precipitation, if any), a rise in conductivity at T_c may also be seen.

In the present system, in case of lower CuI content samples, these tiny crystallites are due to major precipitation of $Ag_8I_4V_2O_7$ which is a relatively poor ionic conductor and such a formation results into drop in the conductivity at crystallization. On the other hand, for higher CuI content, major precipitation of AgI occurs in the system (as suggested by XRD and DSC results), whose conductivity is comparable to that of the connective tissue. Thus no fall in the conductivity at T_c is witnessed.

Further, as discussed in section 3.1.2, SEM results also suggest that the low CuI content samples (10CI-SISOVO) exhibit nucleation dominated crystallization process (Fig. 3.14a), whereas, high CuI content samples (30CI-SISOVO) exhibit the growth dominated (Fig. 3.14b). Thus, two possibilities of the electrical transport may be predicted as shown in the Figs 5 a and b for the CuI substituted SISOVO system.

Region III and the electrical transport in glass-ceramics

On further heating above 130 °C, the conductivity again increases linearly. In the heating cycles of the glass-ceramic samples (Fig. 3.12 b, d and f), for all three glass-ceramics samples, the conductivity increases Arrheniously.

In thermally unstable region (region II), thermal events are absent for all these glass-ceramic samples and conductivity increases linearly as function of temperature in both the region I and II. Further, the activation energy for ionic conduction is found to be $\sim 0.2-0.3$ eV, little higher than those of the glassy samples. The 15 and 30CI-SISOVO samples exhibit a significant deviation from linearity followed by a rise in conductivity at ~ 147 °C that may be due to $\beta \rightarrow \alpha$ phase transition in the precipitated AgI. Such rise is more apparent for 30CI-SISOVO and almost negligible in case of 10CI-SISOVO sample that once again confirms the fact that AgI precipitation increases with CuI content. This transition of glass-ceramic samples is reversible.

The conductivity at room temperature is plotted as a function of CuI content in Fig. 3.15 a. It is apparent that conductivity increases with CuI content, reaches to a maximum of $\sim 10^{-2} \Omega^{-1}$

cm^{-1} at $x=0.35$ (35CISISOVO) and further decreases for higher CuI content. The decrease in the conductivity above $x=0.35$ may be due to increased crystallinity in the samples. The conductivity of the annealed (above T_c) glassy samples also exhibits an increase with Cu^+ ion substitution in the matrix. The activation energy of ionic conduction (E_σ) as a function of CuI content is found to be decreasing (Fig. 3.15 b), which shows consistency with conductivity–temperature cycles. The E_σ value of crystallized samples is found to be lower than those of the virgin glassy samples and follows similar trend with CuI content. Similar results on CuI substituted systems are obtained in earlier investigations (Murugesan et al, 2007). The enhancement in the conductivity is further investigated.

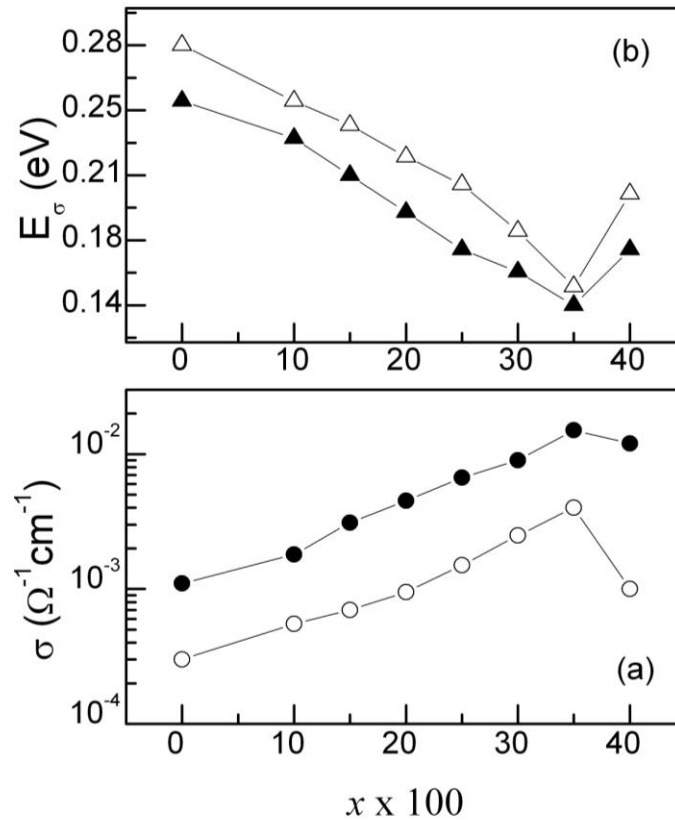


Fig. 3.15: Electrical conductivity at 300K (a) and activation energy ($T \leq T_g$) (b) as a function of CuI content. Symbols denote: room temperature conductivity (●) glass and (○) glass-ceramic samples; (▲) activation energy for glassy samples; (△) for glass-ceramic samples.

The electrical conductivity is given by

$$\sigma = \sum_i n_i q_i \mu_i \quad (3.5)$$

where, n_i is the density and q_i and μ_i the charge and mobility of the i^{th} species of the charge carriers, respectively. As also discussed earlier (Section 3.3), it is proposed by various workers that substituted CuI eventually transforms into Cu_2O according to Eq. 3.1. Thus, the total majority charge carriers i. e., Ag^+ ions in the system are constant and hence increase in the conductivity cannot be directly attributed to the increase in number of charge carriers (n_i). Secondly, investigation by various workers (Murugesan et al, 2007) have shown that Cu^+ ion in such systems do not contribute in the ionic conductivity and the total electrical conductivity is only due to those of Ag^+ ions.

Thus, the first possibility of the conductivity increase should be solely due to increase in mobility of ions due to the formation of favorable structure for smooth ionic movement. To further understand, the increase in the conductivity with CuI content, the ionic mobility (μ) is measured as a function of CuI content by the transient ionic current (TIC) technique (Chandra et al, 1989; Agrawal et al, 1994). Blocking graphite electrodes are pasted on both sides of the glassy sample and cylindrical pellet is further sandwiched between platinum electrodes. The dc voltage of $V \approx 0.4$ V is applied for 1 h to completely polarize the sample. The polarity is then reversed and the transient current is measured as a function of time. The mobility μ ($\text{cm}^2 \text{V}^{-1} \text{s}^{-1}$) can thus be calculated by the Eq. 2.53.

The transient current increases rapidly, attains a maximum and subsequently falls (30CI-SISOVO Fig. 3.16 a). Time (τ) in which current attains a maximum is obtained from this I-t plot (Fig. 3.16 a). For better accuracy, mobility is measured for different thicknesses. Fig. 3.16 shows d^2 versus $V\tau$ plot for two samples 10 and 30CI-SISOVO. Mobility is measured from the slope. The value of mobility is plotted as a function of CuI content in Fig. 3.17. Apparently, mobility appreciably increases with CuI content in the sample.

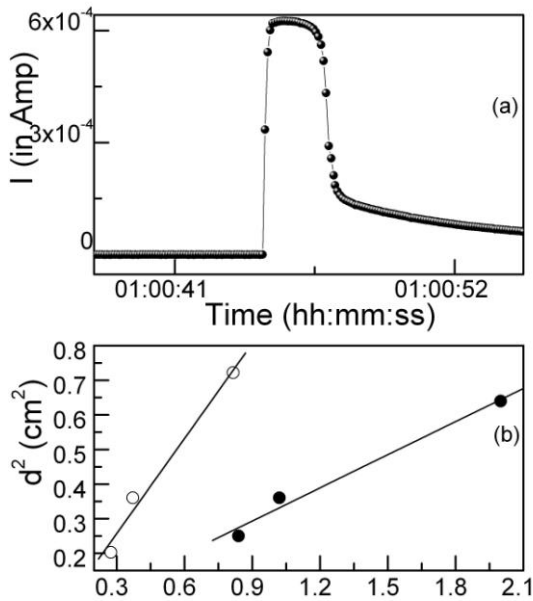


Fig. 3.16: (a) Transient current versus time plot on an extended scale for 30CI-SISOVO sample (b) d^2 versus $V\tau$ plot for 10 and 30 CI-SISOVO samples.

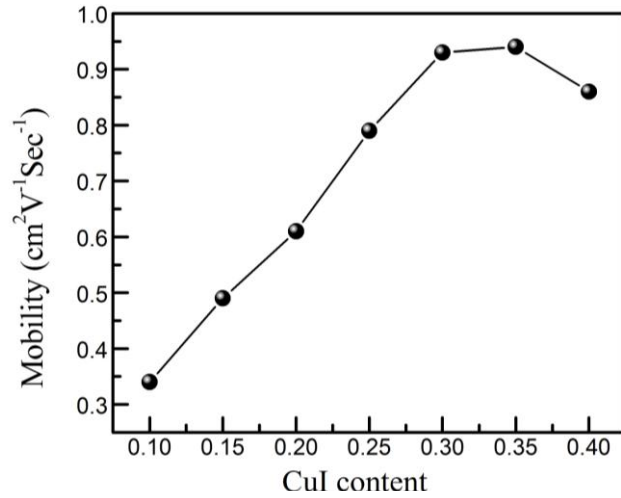


Fig. 3.17: Ionic Mobility as a function of CuI content in the samples

There is another possibility of rise in conductivity in this system. Since, the XRD/DSC results revealed that atleast three types of Ag^+ ions exist in this system. Thus,

$$\text{Total } Ag^+ \text{ ions} = Ag^+(1) + Ag^+(2) + Ag^+(3)$$

Where $Ag^+(1)$, $Ag^+(2)$ and $Ag^+(3)$ are respectively, surrounded by I^- alone, V-O alone and both I^- and V-O units. Even though, the total number of Ag^+ ions is conserved with CuI substitution, there may be increase in $Ag^+(1)$ type ions (which is most conducting among them) on the cost of $Ag^+(2)$ and $Ag^+(3)$. This change in coordinates/surroundings about Ag^+ ions may also contribute through in the conductivity rise.

Thus, it may be concluded here that the rise in conductivity with CuI content is (i) essentially due to Cu_2O substitution in the glass matrix that in turn increases the ionic mobility significantly and may also be due to (ii) increase in type $Ag^+(1)$ silver ions.

3.4 Electrochemical cell characteristics

In order to test the electrochemical stability of these glass-ceramic samples, constant load characteristics were carried out on button type cells fabricated using these samples as electrolytes. Here results are discussed for one of them, viz. 30 CI-SISOVO glass-ceramic sample.

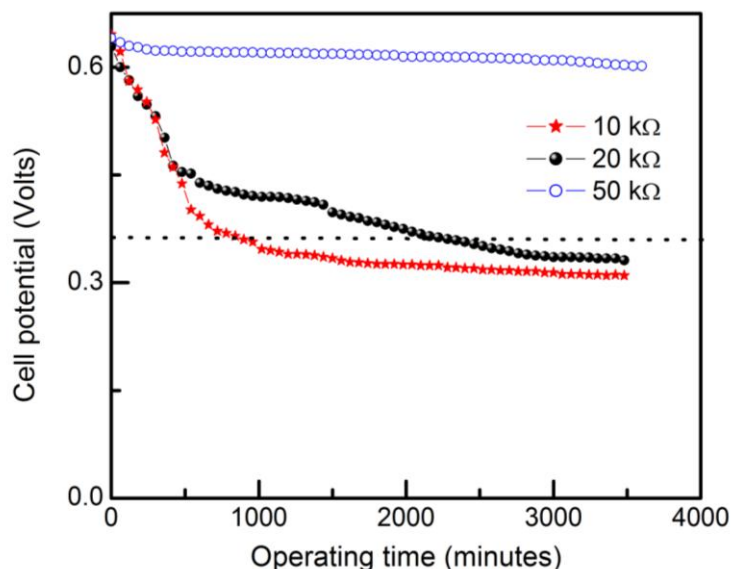


Fig. 3.18: Constant load characteristics for external loads for Ag/I₂ electrochemical cells with 30CISISOVO glass-ceramic sample as electrolyte.

The open circuit voltage (OCV) for 30SICOSOVO sample is almost constant for 24 hrs. Further, current is drawn from the cell at various external loads of 10, 20 and 50 kΩ for next 96 hrs. There is initial fall in the cell potential generally for all samples, but the fall is more drastic for the load of 10 and 20 kΩ and stabilizes subsequently. This fall may be due to polarization and/or formation of thin AgI layer at the interface. At high load viz. 50 kΩ or low current drop, the cell voltage is practically constant over a 96hrs. Thus, it is concluded here that these samples are stable under the battery conditions.

3.5. Conclusion

1. Thermal properties of CuI substituted SISOVO system revealed interesting results. Samples till $x=0.35$ are highly glassy in nature. The system is found to exhibit multiple crystallization and electrical conductivity versus temperature cycles successfully reveal the crystallization behavior of these samples. The massiveness/extent of the crystallization

decreases with CuI content in the glass matrix. There is simultaneous precipitation of three compounds, viz., AgI, $\text{Ag}_4\text{V}_2\text{O}_7$ and $\text{Ag}_8\text{I}_4\text{V}_2\text{O}_7$. However the temperature for the rate of maximum crystallization is different for each of them, as suggested by XRD and DSC results. The activation energies of structural relaxation (E_s) at T_g and crystallization (E_c) do show significant change with CuI addition. As a result, crystallization of $\text{Ag}_4\text{V}_2\text{O}_7$ and $\text{Ag}_8\text{I}_4\text{V}_2\text{O}_7$ decreases and that of AgI increases with CuI addition, as also revealed by $\sigma - T$ cycles. Thus, CuI plays an important role in the crystallization. The Avrami parameter calculated using Ozawa/Matusita Sakka equations suggests surface nucleation regime and exhibit no significant temperature dependence.

2. Cu^+ ion substitution significantly affects electrical as well as thermal properties of the AgI– Ag_2O – V_2O_5 system. The ionic conductivity is found to be increasing with CuI content that may be attributed to increase in the mobility due to Cu_2O incorporation into the matrix, whereas, subsequent drop above $x=0.35$ may be due to crystallization.

3. The annealing of the glasses above T_c results into formation of glass-ceramic nano composites as confirmed by SEM and XRD results. These are thermally stable at least upto $\sim 170^\circ\text{C}$ with ionic transport number near unity. The highest conductivity for such composites is found to be $\sim 2 \times 10^{-3} \Omega^{-1}\text{cm}^{-1}$ at room temperature achieved for a composition 35 CI-SISOVO. The same sample is used as electrolyte in Ag/ I_2 cell and exhibits good electrochemical stability. Using the SEM and XRD results, a model, viz. crystallite by-pass model is proposed to explain the conductivity behavior in thermally unstable region of the superionic glasses.

CHAPTER 4

AgI-Cu₂O-Ag₂O-V₂O₅ SYSTEM: Role of glass modifier variation

As discussed earlier in chapter 3, Copper iodide has been used as a possible dopant in silver oxysalt glassy (SISOVO) superionic system by various workers. The substitution of CuI in place of AgI in to the glass matrix leads to significant enhancement of ionic conductivity. It is demonstrated in chapter 3 that rise in conductivity is mainly attributed to notable increase of mobility of Ag⁺ ions in the glass matrix. The CuI, that replaces AgI, reacts with Ag₂O according to following reaction:



Thus addition of CuI eventually leads to precipitation of Cu₂O into the matrix, conserving the amount of AgI into the system. For a better understanding, the thermal properties, trends of stability parameters were also investigated for samples prepared by direct substitution of Cu₂O in the glass matrix. Thus this chapter discusses the effect of direct incorporation of Cu₂O addition in SISOVO matrix. The compositions 50AgI-33.33{(Cu₂O)_x-(Ag₂O)_{1-x}}-16.67 V₂O₅ for x=0.1, 0.15, 0.20, 0.25, 0.30 and 0.40 (corresponding to 3.33, 5, 6.67, 8.33, 10 and 13.33 m/o of Cu₂O in AgI-Ag₂O-V₂O₅ system, respectively) were chosen and abbreviated as 10, 15, 20, 25, 30 and 40SICOSOVO, respectively. Some of these form glass, whereas, other form glass-ceramics. In addition, the effect of variation of Ag₂O amount, i.e. the role of glass modifier itself, on thermal properties is also studied in the chapter.

4.1. Structural investigations

4.1.1. X-ray diffraction

The X-ray diffraction (XRD) measurements have been carried out to study the structural properties of 50AgI-33.33[(Ag₂O)_{1-x}-(Cu₂O)_x]-16.67V₂O₅ superionic system and shown for 10 and 30 SICOSOVO in Fig. 4.1. For 10 SICOSOVO, absence of any significant peak (Fig.4.1a) apparently confirms the glassy/amorphous nature. Whereas, the pattern for high Cu₂O content sample, viz. pristine 30 SICOSOVO, exhibits tiny peaks (Fig. 4.1c) that suggest (1) glass is

partially crystalline and (2) may have composite nature. The particle size for this as prepared 30 SICOSOVO sample is found to be $\sim 30\text{-}40\text{ nm}$ using Debye-Scherrer relation (Eq. 2.10). The XRD patterns of the samples annealed above all the crystallization temperatures (later revealed by DSC) are shown in Fig. 4.1 b and d. As evident, the annealing of 10 SICOSOVO sample at 170°C results mainly into precipitation of three compounds, viz., AgI, $\text{Ag}_4\text{V}_2\text{O}_7$ and $\text{Ag}_8\text{I}_4\text{V}_2\text{O}_7$ (Fig 4.1 b). Apart from these some unidentified peaks are present in the pattern that may be due to precipitation of some compound containing copper, oxygen and vanadium in a very small amount.

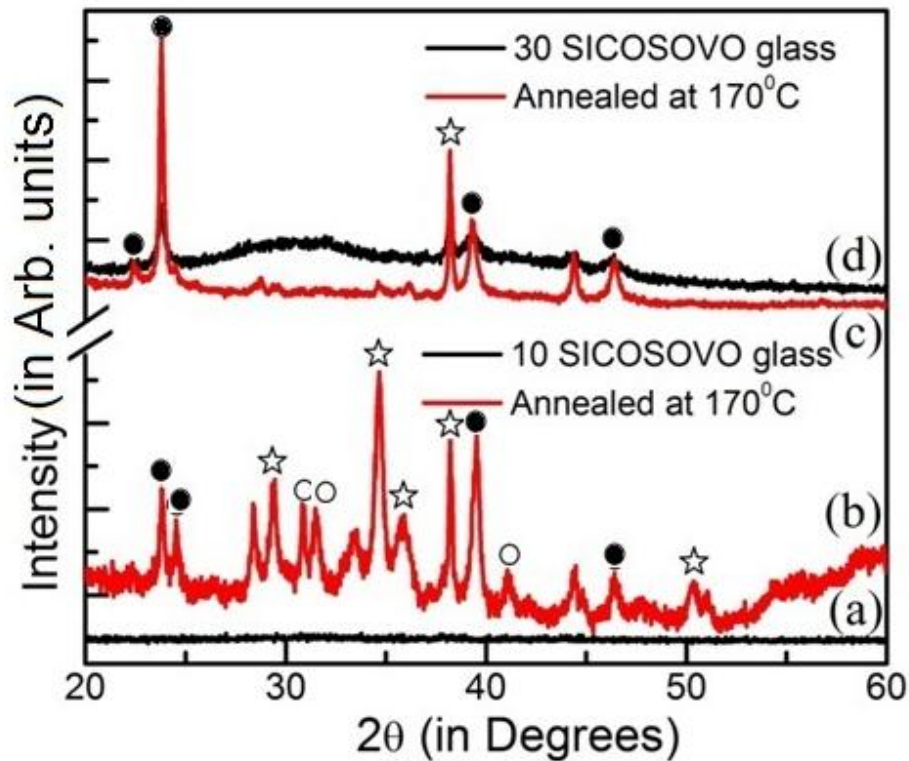


Fig.4.1: X-ray diffraction patterns for as prepared glasses (a and d), glass ceramics (b, c). Symbol denote (●) AgI (○) $\text{Ag}_4\text{V}_2\text{O}_7$ and (☆) $\text{Ag}_8\text{I}_4\text{V}_2\text{O}_7$

Apparently, the 30 SICOSOVO sample annealed at 170°C results into precipitation of the same two compounds viz., AgI and $\text{Ag}_8\text{I}_4\text{V}_2\text{O}_7$. However, the peak height corresponding to

AgI grows and for $\text{Ag}_8\text{I}_4\text{V}_2\text{O}_7$ found to be suppressed (Fig. 4.1d). The particle size for these precipitated samples is found to be little grown upto $\sim 50\text{-}60\text{ nm}$.

Present results suggest that Cu_2O addition facilitates the precipitation of AgI and suppresses that of $\text{Ag}_8\text{I}_4\text{V}_2\text{O}_7$ and $\text{Ag}_4\text{V}_2\text{O}_7$ in these glasses. Thus, the results suggest that samples for $x < 0.3$ are indeed glassy in nature and those of higher Cu_2O content results into glass-ceramic formation.

To further scrutinize the precipitated compounds, X-ray diffraction patterns are also obtained for 20 SICOSOVO (Fig. 4.2), which is a composition well within the glass forming region. As apparent, a halo pattern in as prepared 20SICOSOVO sample (Fig 4.2a) suggests the amorphous nature of the sample. The X-ray diffraction patterns of same samples annealed above the crystallization temperatures (later revealed by DSC) are shown in Fig. 4.2 b and c.

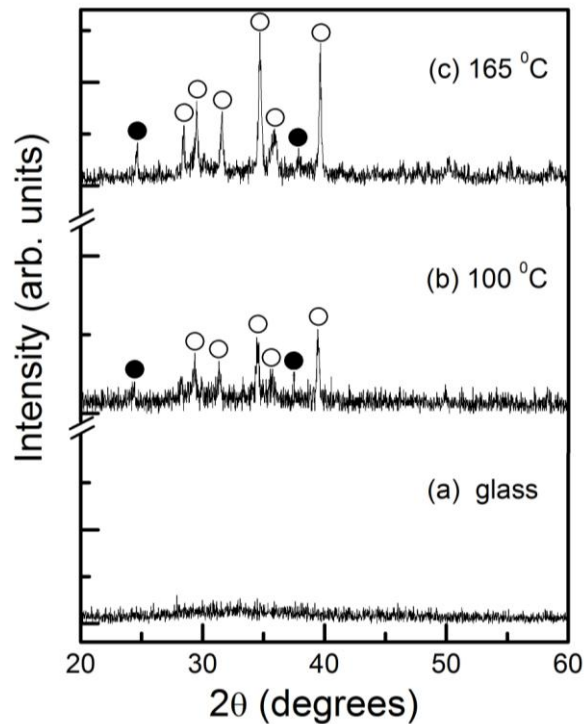


Fig.4.2: X-ray diffraction patterns for 20 SICOSOVO, (a) as prepared and glass ceramics obtained after annealed at (b) 100 °C and (c) 170 °C. Symbol denote (●) AgI and (○) $\text{Ag}_8\text{I}_4\text{V}_2\text{O}_7$

The annealing of 20 SICOSOVO sample at 100 °C (a temperature above T_{c1}) results mainly into precipitation of two compounds, viz., AgI, and $\text{Ag}_8\text{I}_4\text{V}_2\text{O}_7$, as evident in Fig 4.2 b. For the sample annealed at 165 °C, there is significant growth in peaks correspond to precipitation of

$\text{Ag}_8\text{I}_4\text{V}_2\text{O}_7$ compound, whereas, height of peaks correspond to AgI remain unaffected. It may be suggested here that annealing at lower temperature results into formation of AgI with $\text{Ag}_8\text{I}_4\text{V}_2\text{O}_7$, whereas, major crystallization of $\text{Ag}_8\text{I}_4\text{V}_2\text{O}_7$ compound at respective higher temperature. The particle size calculated using Debye-Scherrer relation is found to be $\sim 35 - 40$ nm for both the compounds.

These results suggest that the as prepared samples containing small amount of Cu_2O ($x = 0.1, 0.2$) exhibit complete glassy nature and on annealing results into precipitation of three compounds viz., $\text{Ag}_8\text{I}_4\text{V}_2\text{O}_7$, AgI and $\text{Ag}_4\text{V}_2\text{O}_7$ at various stages. Annealing at lower temperature ($\sim 100^\circ\text{C}$) results into precipitation of AgI, whereas, the second state precipitation (at 170°C) is that of $\text{Ag}_8\text{I}_4\text{V}_2\text{O}_7$ along with $\text{Ag}_4\text{V}_2\text{O}_7$ in small amount. No precipitation of copper based compound suggests that incorporated Cu_2O remains in the amorphous matrix.

4.1.2. Scanning electron Microscopy

SEM images are obtained for all the Cu_2O substituted SISOVO glass and glass-ceramic samples as well and shown for 10 and 30 SICOSOVO sample in Fig. 4.3.

Annealing of 10 SICOSOVO at first crystallization temperature ($\sim 100^\circ\text{C}$) results into precipitation of small crystallites which is surrounded by connective tissues, whereas, annealing at high temperature (above complete crystallization, $\sim 170^\circ\text{C}$) results into formation of glass-ceramic structure (Fig. 4.3b and c). The tiny crystallites may belong to AgI, $\text{Ag}_4\text{V}_2\text{O}_7$ and $\text{Ag}_8\text{I}_4\text{V}_2\text{O}_7$ compounds dispersed uniformly in the glass matrix.

It is revealed from Fig. 4.3 d that as prepared glass of 30SICOSOVO also exhibits tiny crystallites within the glassy matrix. Whereas, for the glass-ceramic samples (Fig. 4.3 e), there is growth in the size of these tiny crystallites.



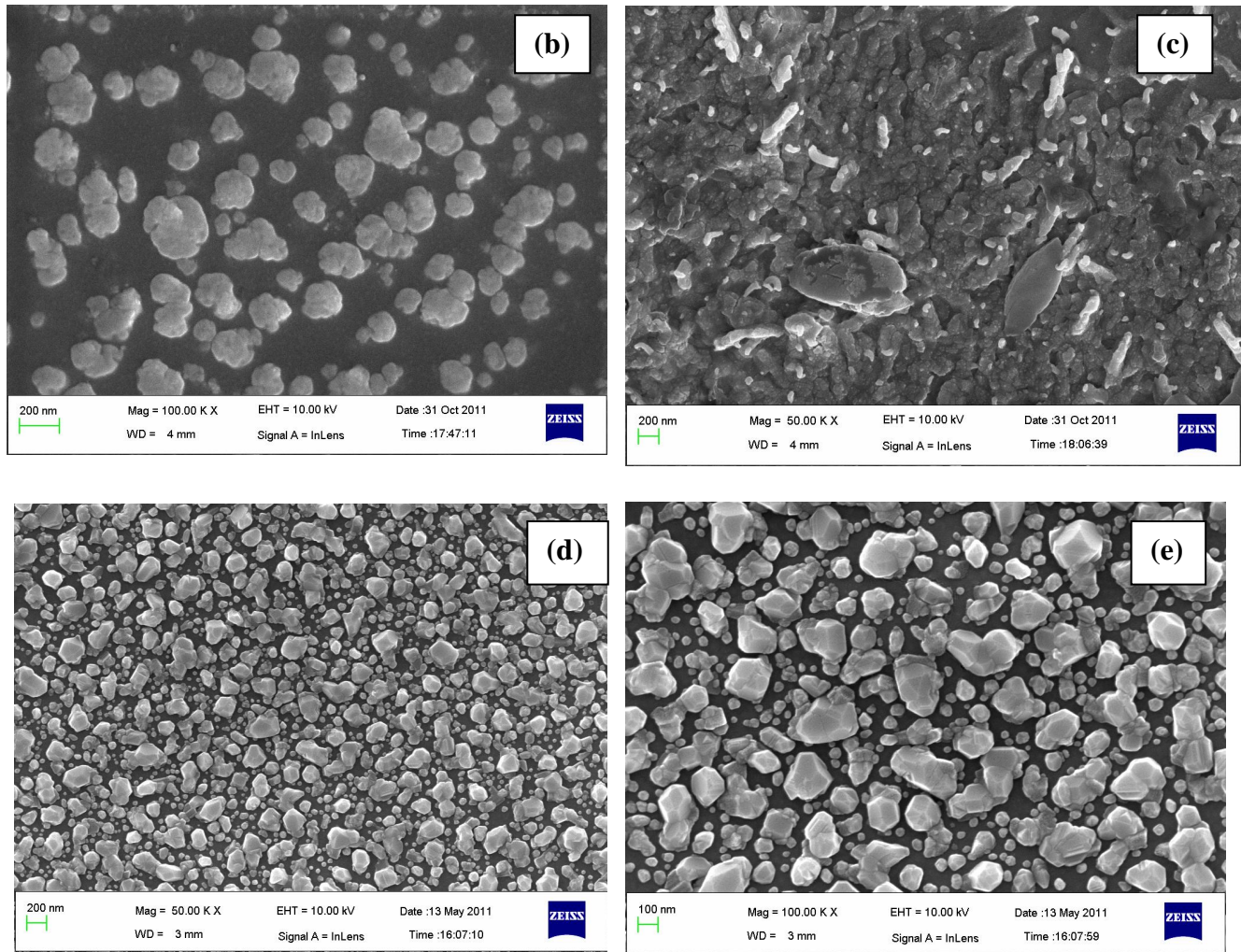


Fig. 4.3: Scanning electron microscopy scans for 10SICOSOVO (a) glass and glass-ceramics annealed at (b) 100⁰C (c) 170⁰C and 30SICOSOVO (d) glass and (e) annealed at 140⁰C

As XRD results suggest, these crystallites may be that of AgI compound which precipitate during the crystallization process. The particle size obtained from these images are found to be in the range of ~20-200nm. For $x \geq 0.3$, it is not possible to form the glass/composites.

4.2. Differential Scanning calorimetry

Differential scanning calorimetry (DSC) is performed on all the samples and shown for 10 and 30 SICOSOVO samples in Fig. 4.4 at a typical heating rate of 10 °C /min. For all the as prepared glassy samples (Fig. 4.4 a, and b), there appear an endothermic smooth dip in 50-65 °C temperature range that correspond to respective glass transition temperature (T_g) of these samples. The T_g shows a decrease with Cu_2O content as reported in Table 4.1. It is also apparent (Fig. 4.4) that multiple crystallization peaks occur in the DSC scans which suggest the complex nature of the samples.

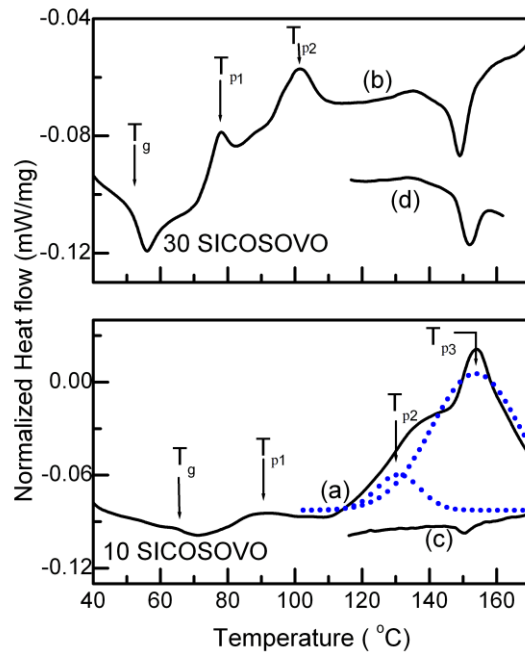


Fig. 4.4: DSC scans for different compositions of SICOSOVO glassy samples (a and b) and glass ceramic samples (c and d).

In Fig. 4.4 (a), for 10 SICOSOVO sample crystallization begins at ~ 80 °C followed by a small but significant exothermic hump. On further heating, there appears a broad exothermic crystallization peak with onset (T_c) at ~ 110 °C, that may be visualized as two merged-up peaks having maximum at ~ 135 (T_{p1}) and ~152 °C (T_{p2}). On further heating, the sample melts near 200 °C.

These DSC results again suggest that there are at least three compounds that precipitate during the crystallization at different maximum rate of crystallizations for lower Cu_2O content samples ($x \leq 0.2$). In agreement with XRD results, T_{p1} , T_{p2} and T_{p3} may be attributes to AgI,

Ag₄V₂O₇ and Ag₈I₄V₂O₇, precipitation respectively. Similar DSC results were obtained for all the samples ($x < 0.3$).

The DSC scans for as prepared 30 SICOSOVO, which is partially crystalline (Fig 4.4 b) exhibit patterns significantly different from those of the other ($x < 0.3$) glassy samples. In this, two consecutive exothermic peaks appear to begin at ~ 80 and 100 °C. On further heating, a small endothermic dip appears at ~ 150 °C that may correspond to characteristic of $\beta \rightarrow \alpha$ phase transition in AgI. It may be suggested here that higher Cu₂O content samples again exhibit major precipitation of AgI in two stages.

In Fig. 4.4 c and d, second heating cycles are shown for 10 and 30 SICOSOVO, respectively. Only one endothermic dip is seen for 10 SICOSOVO and 30 SICOSOVO at ~ 147 °C. The area under the dip increases with Cu₂O content that confirms the increasing precipitation of AgI during the first cycle.

Apparently, these results are in good agreement to those of XRD results.

Table 4.1: Thermal stability parameters as a function of Cu₂O content.

$x \times 100$	T_g (°C)	T_c (°C)	$T_c - T_g$ (°C)	$T_{rg} (T_g/T_m)$
0	68	100	32	0.32
5	65	90	25	0.31
10	60	85	25	0.3
15	58	83	25	0.29
20	56	80	24	0.29
25	53	77	24	0.27
30	50	74	24	0.27

To further understand the thermal events in the samples, the parameters defining the thermal stability (also introduced in Chapter 3) are obtained from DSC plots and given in Table 4.1. These parameters viz., T_c , T_g consistently decrease with Cu₂O content, whereas, T_{rg} and $T_c - T_g$ almost remain constant and exhibit no appreciable change.

4.2.1. Glass transition and crystallization kinetics

The DSC scans are performed for all these compositions ($x = 0.1-0.3$) at various heating rates (5 - 20 °C/min) and are shown for two of the samples, viz., 10 and 20 SICOSOVO in Fig. 4.5 and 4.6, respectively. For clarity the patterns are shown for four heating rates only. It is readily noted that the glass transition and crystallization temperatures shift to higher values as the heating rate (q) increases.

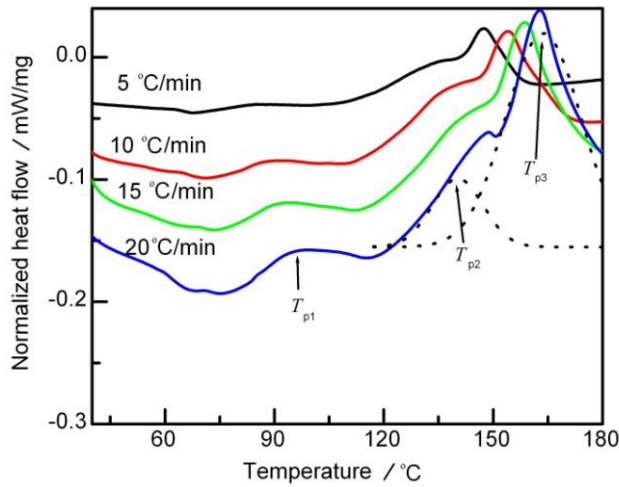


Fig. 4.5: DSC scans at various heating rates for 10 SICOSOVO sample. T_{p1} , T_{p2} and T_{p3} correspond to major precipitation of AgI, $Ag_4V_2O_7$ and $Ag_8I_4V_2O_7$, respectively.

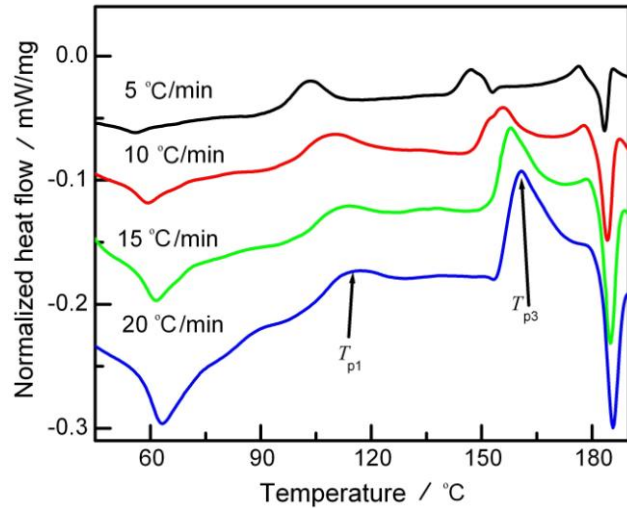


Fig. 4.6: DSC scans at various heating rates for 20 SICOSOVO sample. Major precipitation of AgI at T_{p1} and $Ag_8I_4V_2O_7$ at T_{p3} .

Fig. 4.7 shows the plot of $\ln q$ versus inverse of T_g for 10-30SICOSOVO samples. Resulting graphs are very much linear whose slope yields the E_s value at T_g . These E_s values obtained from the graph has been plotted in Fig. 4.8 with Cu_2O content in the glass matrix.

For the accuracy the parameters are reported and discussed only for the samples well within the glass forming region. It is interesting to note that E_s value decreases with Cu_2O content. The activation energy for structure relaxation (E_s) is associated with the viscous flow at T_g . Thus, it may be suggested that the energy required for structural units to overcome the frozen viscous state at T_g decreases with Cu_2O addition. Similar trends of E_s versus CuI content have been obtained for CuI doped $AgI-Ag_2O-V_2O_5$ system as well (Chapter 3).

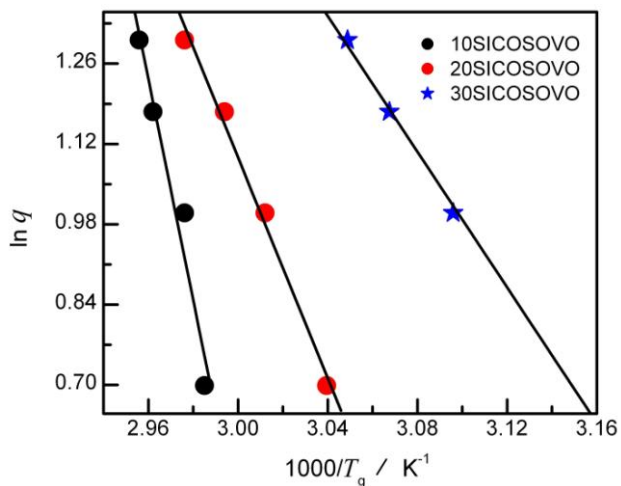


Fig. 4.7: $\ln q$ versus inverse of temperature for 10, 20 and 30 SICOSOVO.

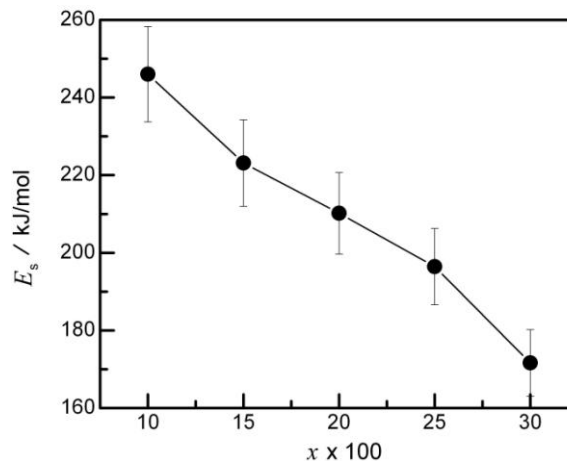


Fig. 4.8: The activation energy for structural relaxation at T_g as a function of Cu_2O content in SICOSOVO.

Since, the XRD along with DSC results suggested that annealing of these glasses results into precipitation of three different compounds for 10SICOSOVO, the exothermic peak 1, 2 and 3 apparent in Fig. 4.5 are attributed to precipitation of AgI, $\text{Ag}_4\text{V}_2\text{O}_7$ and $\text{Ag}_8\text{I}_4\text{V}_2\text{O}_7$ compounds, respectively. The plot of $\ln(q/T_p^2)$ versus inverse of T_p is obtained for the samples well within the glass forming region corresponding to respective crystallization peaks. For 10-25 SICOSOVO samples these plots are shown in Fig. 4.9 correspond to AgI precipitation that occurs at the first peak in the DSC patterns. Similarly the kinetics of second crystallization peak correspond to $\text{Ag}_8\text{I}_4\text{V}_2\text{O}_7$ precipitation. The E_c values obtained from the slopes for various precipitated compounds are plotted in Fig. 4.10 as a function of Cu_2O content.

The fact that E_c values corresponding to AgI precipitation decreases strongly suggest that higher Cu_2O content reduces the energy barrier for crystallization and facilitates the crystallization of AgI. Likewise, the E_c values are also obtained for the precipitation of $\text{Ag}_8\text{I}_4\text{V}_2\text{O}_7$. In this case, the E_c values show a systematic rise that suggests existence of prominent energy barriers corresponding to precipitation of $\text{Ag}_8\text{I}_4\text{V}_2\text{O}_7$. Thus its formation during crystallization is suppressed. The composition dependence of E_c value corresponding to precipitation of the third compound $\text{Ag}_4\text{V}_2\text{O}_7$ could not be obtained as its precipitation is not very apparent in high Cu_2O content samples. It is also evident from the DSC results (Fig. 4.4 a

and b) that crystallization peak corresponding to precipitation of (i) AgI grows and (ii) $\text{Ag}_8\text{I}_4\text{V}_2\text{O}_7$ is drastically suppressed as a function of Cu_2O content. These results are in agreement with crystallization kinetics.

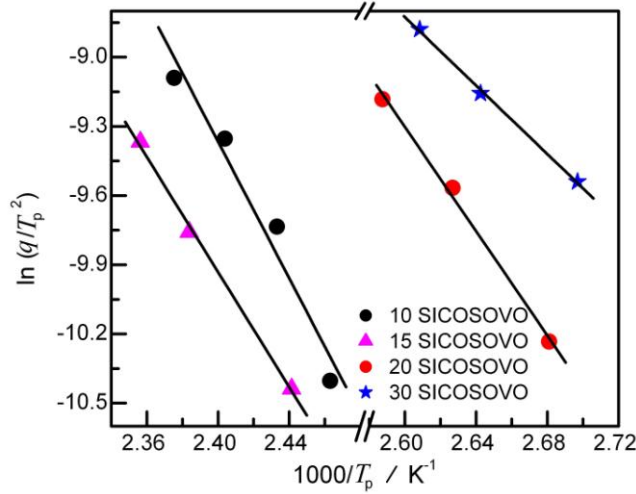


Fig. 4.9: Modified Kissinger plot for 10, 15, 20 and 30 SICOSOVO samples corresponding to precipitation of AgI (T_{p1})

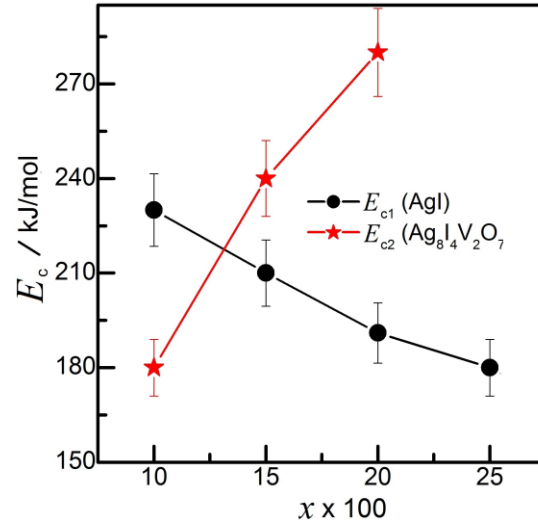


Fig. 4.10: The E_c values as a function of Cu_2O content.

Due to complex nature of the system, the Avrami parameter n in the present case is calculated only using Augis –Bennett method and given in Table 4.2. The value of n is found to be nearly unity for all the compositions. As discussed earlier in chapter 3, wide crystallization peak generally refers to the surface crystallization within the samples, whereas, the sharp peak infers about the bulk crystallization. Thus, it may be concluded here that overall crystallization in these samples is dominated by surface nucleation.

Table 4.2: The Avrami parameter calculated by Augis - Bennett relation at various rates as a function of CuI content (5-20 °C/min) for the crystallization of three different compounds viz., AgI, $\text{Ag}_4\text{V}_2\text{O}_7$ and $\text{Ag}_8\text{I}_4\text{V}_2\text{O}_7$.

X	Heating rate (q)	n		
		Peak 1 (AgI)	Peak 2 ($\text{Ag}_4\text{V}_2\text{O}_7$)	Peak 3 ($\text{Ag}_8\text{I}_4\text{V}_2\text{O}_7$)
0.1	5	1.01	0.95	1.5
	10	1.14	1.3	0.88

	15	1.3	1.5	0.9
	20	1	0.9	1.8
0.2	5	1.27	-	1.5
	10	0.96	-	0.99
	15	1.03	-	1.3
	20	0.99	-	1.2
0.3	5	1	-	-
	10	1.2	-	-
	15	0.88	-	-
	20	1.7	-	-

It has been demonstrated by various workers (Nowinski et al, 2008) that Ag_2O content and hence (Ag_2O - V_2O_5 ratio) plays an important role in formation as well as electrical properties of AgI-glasses.

To scrutinize the thermal properties with the variation of Ag_2O amount, differential scanning calorimetry scans are again performed at various heating rates and shown for one composition in Fig. 4.11. Using the formulation given in Section 2.2 thermal stability parameters are obtained. The DSC scans of this system exhibit two closely and merged up prominent crystallization peaks which correspond to precipitation of $\text{Ag}_8\text{I}_4\text{V}_2\text{O}_7$ and $\text{Ag}_4\text{V}_2\text{O}_7$ (also confirmed by XRD on annealed samples). Since the precipitation of these compounds could not be attributed to T_{p1} and T_{p2} , crystallization kinetics could not be done to avoid misleading information and interpretation. However the glass transition kinetics of this system revealed interesting results. As shown in Fig. 4.11, these peaks shift to higher temperatures with increasing ramps. Thus, the activation energies of structural relaxation and crystallizations are obtained and plotted as a function of Ag_2O amount in SISOVO glass matrix in Fig. 4.12. Apparently, E_s increases with Ag_2O content.

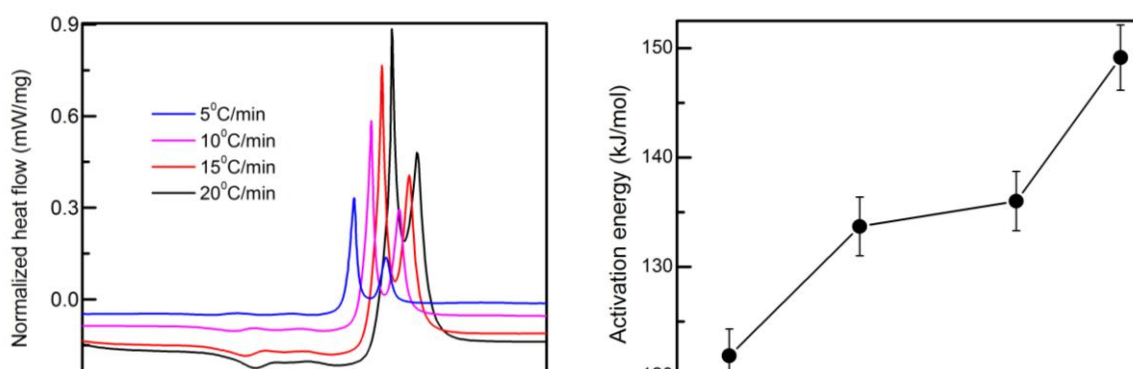


Fig. 4.11: DSC scans at various heating rates for 50AgI-27.5Ag₂O-22.5V₂O₅ sample.

Fig. 4.12: The activation energy for structural relaxation as a function of Ag₂O content in AgI-Ag₂O-V₂O₅ system.

As evident, it may be also be noticed here that CuI as well as Cu₂O substitution reduces Ag₂O amount in the glass matrix and in this perspective the E_s values obtained in case of Cu₂O and CuI substituted samples are in good agreement with Fig. 4.12.

4.3. Electrical conductivity and Ionic mobility

At the outset, the ionic transport number for all the samples ($x \leq 0.3$) was measured by galvanic cell method. Cells of two types: (i) Ag|SICOSOVO|I₂ and (ii) Cu|SICOSOVO|I₂ were prepared and open circuit voltage (OCV) was measured as a function of time. For the Ag/I₂ cells the OCV quickly attains a value of 0.678 volts and remains fairly constant close to the calculated value (0.687 Volts). On other hand, the OCV for Cu/I₂ type cells found to be developing very slowly and after fluctuations stabilizes subsequently at 0.4 volts that is much less than calculated OCV of 0.72V for Cu/I₂ cells. This may further suggest (i) Cu⁺ ions are less mobile than Ag⁺ ions in these glasses and (ii) system is essentially Ag⁺ ion conducting with ionic transport number near unity.

The electrical conductivity is studied above the T_g and T_c, for all the compositions. The room temperature conductivity and activation energy is plotted for the first and second heating cycles in Fig. 4.13. The conductivity is found to be increasing with Cu₂O content in the glass matrix for both the cycles till $x = 0.3$ and falls subsequently. The maximum conductivity at room temperature is found to be $\sim 2 \times 10^{-2} \Omega^{-1}\text{cm}^{-1}$ with minimum activation energy of ~ 0.13 eV for a composition $x = 0.3$. The room temperature conductivity of glass-ceramic samples exhibits similar trend. For the composition $x \gg 0.3$ it is not possible to obtain homogeneous glass-

ceramic/ nanocomposite on quenching so these compositions are omitted in the study. The activation energy for ionic conduction obtained for both cycles in the thermally stable region ($T \leq T_g$) exhibits expected opposite trend to conductivity. The compositions well below $x = 0.3$ are glassy, whereas, glass-ceramic nanocomposite formation is evident at and above $x = 0.3$. As apparent, the rise in the conductivity with compositions is not abrupt but gradual. Thus it may be suggested here that the highest conductivity at this composition, even though it is not completely glassy, is most likely due to compositional variations of the glass matrix rather than the nanocomposite nature.

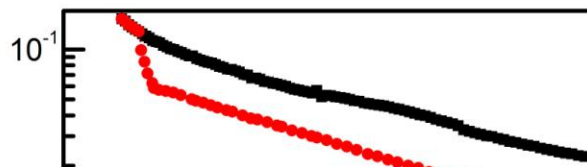
Fig. 4.13 (a) Electrical conductivity as a function of Cu_2O content at room temperature. (b) Activation energy as a function of Cu_2O content.

According to structural model, for this system again it may be suggested that two types of Ag^+ ions surrounded by (1) I units and (2) Vanadium and Oxygen units are likely in the glass matrix.

Further, the electrical conductivity (1kHz) versus temperature ($\sigma-T$) at a typical heating rate of $1^\circ\text{C}/\text{min}$ is shown in Fig 4.14. For better understanding of these $\sigma-T$ cycles are again divided in three regions.

The conductivity versus temperature cycles for all the glassy samples are reversible up to $55-60^\circ\text{C}$ ($T \leq T_g$). In this region I, conductivity linearly increases with temperature and exhibits activation energy of $0.25-0.3\text{eV}$.

The region II is thermally unstable due to glass transition and crystallization. Above the T_g the conductivity shows anomalous rise deviating from linearity (apparent in Fig 4.14a for 10



SICOSOVO). On further heating, the conductivity falls drastically from 110 °C till 135 °C. This fall must be due to massive crystallization in the sample.

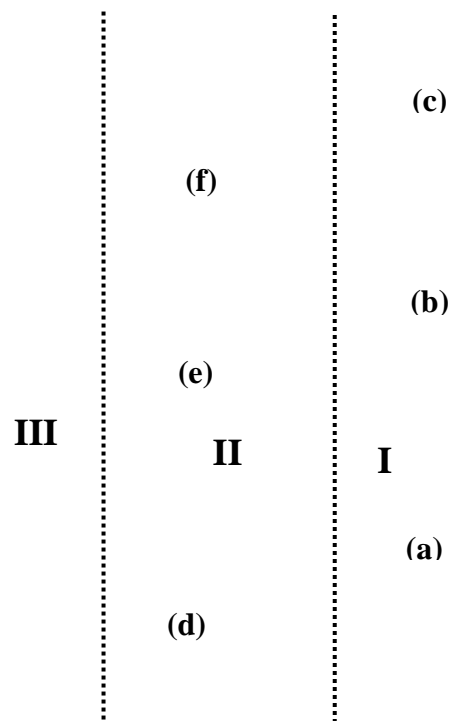


Fig. 4.14: Electrical conductivity as a function of inverse of temperature for (a) 10SICOSOVO, (b) 20SICOSOVO and (C) 30SICOSOVO samples. Symbols: (●) The glassy samples and (○) glass-ceramic samples.

at T_g , though a plateau like region is apparent in the vicinity of T_c of this sample that may be an indication of smaller and slower magnitude of crystallization. It is readily noted that electrical properties of the system is very similar to that of CuI substituted SISOVO (Chapter 3) system and hence this behavior of conductivity can also be explained using two models (1) crystallite by pass model and (2) structural model.

On further heating (above 135 °C) i.e. region III , conductivity increases linearly with inverse of temperature. In this region samples are essentially glass-ceramics and exhibit thermal stability.

The $\sigma - T$ cycles of glass-ceramic samples are shown in Fig. 4.14 d, e and f. Similar to those of the glassy samples, the electrical conductivity exhibits Arrhenius behaviour and cycles are

almost linear with activation energy of $\sim 0.28\text{-}0.33$ eV till ~ 147 °C where conductivity undergoes an apparent rise by a small amount. This rise in the conductivity, more prominent for higher Cu_2O content samples, is due to $\beta \rightarrow \alpha$ transition in AgI. This again suggests the increasing precipitation of AgI in these samples with Cu_2O addition in the matrix.

In the previous investigations (Chapter 3), the electrical conductivity enhancement with CuI substitution is attributed to significant rise in the mobility of Ag^+ ions (Section 3.3). It has important to understand the reasons of enhancement in the conductivity in Cu_2O substituted samples as well. Thus, to scrutinize the conductivity behavior, ionic mobility has been investigated for these samples using transient ionic current technique.

The mobility μ ($\text{cm}^2 \text{V}^{-1} \text{s}^{-1}$) can thus be obtained by the same method as described in section 3.4. For one of the sample (10 SICOSOVO), transient current is shown in Fig. 4.15 a. On reverse the voltage the current increases rapidly and attains a maximum and subsequently falls abruptly. Time (τ) in which current attains a maximum is obtained from such I-t plots. Mobility as a function of Cu_2O are thus obtained (Fig. 4.15 b). Interestingly, mobility increases with Cu_2O substitution and approaches maximum for $x = 0.3$.

These results suggest that Cu_2O substitution plays an important role in the formation of a structure that in turn facilitates the ionic motion.

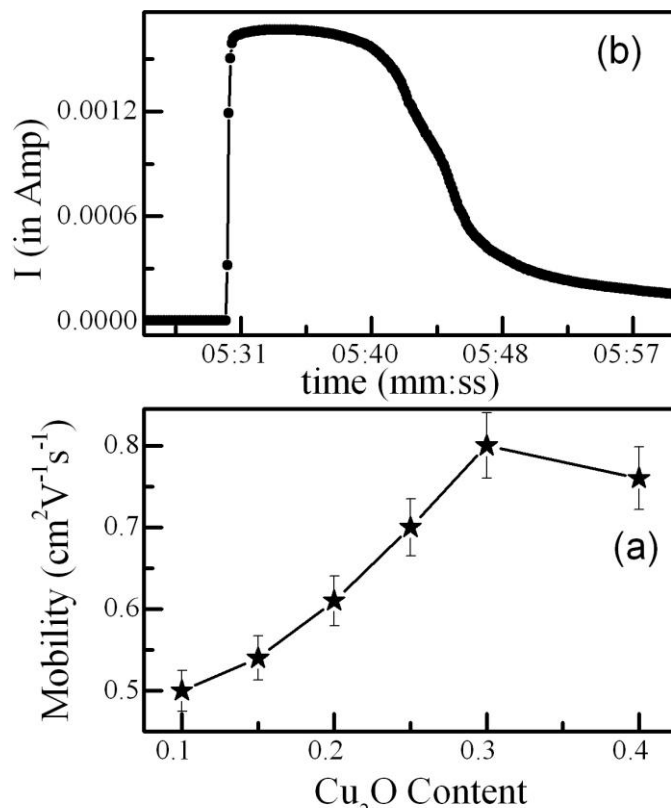


Fig. 4.15: (a) Transient current versus time plot on an extended scale for 30SICOSOVO sample. (b) Ionic Mobility as a function of Cu_2O content in the samples.

Interestingly in both (i.e. CuI substituted and direct Cu_2O substituted) type of systems any change in majority charge carriers is not expected. The ionic mobility vs composition exhibits similar trends (Fig. 3. 17 and 4.15) and thus it may be suggested here that it is the enhancement in the ionic mobility that essentially responsible for the conductivity enhancement in both the systems. However, the other possibility also remains that number of conducting Ag^+ ion (surrounded by I^- alone) may also increase on the cost of immobile Ag^+ ions as discussed in chapter 3.

4.4 Electrochemical cell characteristics

In order to test the electrochemical stability of these samples, constant load characteristics were carried out on button type cells fabricated using these samples as electrolytes. Here results are discussed for highest conducting 30 SICOSOVO sample which is glass-ceramic in nature.

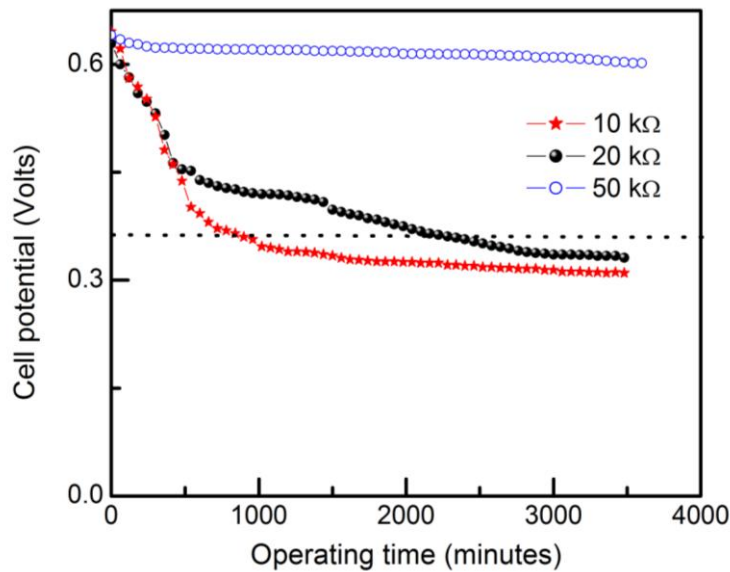


Fig. 4.16: Constant load characteristics for external loads for Ag/I₂ electrochemical cells with 30SICOSOVO glass-ceramic sample as electrolyte.

The open circuit voltage (OCV) for 30SICOSOVO sample is almost constant for 24 hrs. Further, current is drawn from the cell at various external loads of 10, 20 and 50 k Ω for next 96 hrs. There is initial fall in the cell potential in general for each case but the fall is drastic for the load of 10 and 20 k Ω . This fall may be again due to polarization and/or formation of AgI layer at the interface. At high load viz. 50 k Ω or low current drop, the cell voltage is practically constant over a 96hrs.

Again, for external load (10, 20k Ω), the cell voltage decreases gradually but stabilizes later on for the cells. Thus, it is concluded here that these samples are stable under the battery conditions.

4.4. Conclusion

1. Substitution of Cu₂O in AgI-Cu₂O_x-Ag₂O_{1-x}-V₂O₅ system exhibits interesting thermal properties. Samples till x=0.3 are highly glassy in nature. The system is found to exhibit multiple crystallization. The massiveness/extent of the crystallization is suppressed with Cu₂O content in the glass matrix. Cu₂O content significantly affects thermal stability parameters T_c, T_g, E_s and E_c. Such a substitution of Cu₂O facilitates crystallization of AgI but suppresses that of Ag₈I₄V₂O₇. The trend of E_s values suggest that glass become less viscous with Cu₂O content that may be playing an important role in conductivity enhancement as well.
2. Ionic conductivity of SISOVO can not only be increased by CuI substitution but also can be significant enhanced with Cu₂O substitution. Increase in the ionic conductivity is attributed to mobility rise.
3. For the glass-ceramic samples of this system, the highest conductivity is found to be $\sim 7 \times 10^{-3} \Omega^{-1} \text{cm}^{-1}$ at room temperature for 30 SICOSOVO. These highly conducting glass-ceramic samples are found to be thermally more stable than those of glassy samples of the same compositions. These highly conducting and thermally stable Cu₂O substituted glass-ceramic samples are stable under battery conditions and suitable for low power ionic devices.

4. The Cu_2O substituted samples are found to be very much similar to those of CuI substituted samples investigated earlier. In conclusion, both the substitutions, viz. (i) CuI in place of AgI and (ii) Cu_2O in place of Ag_2O in SISOVO matrix introduce similar changes in structural and thermal properties.

CHAPTER 5

AgI-Ag₂O-V₂O₅-MoO₃ SYSTEM: Variation of glass former

Present chapter discusses the effect of variation of MoO₃ (glass former) content in AgI-Ag₂O-(V₂O₅)_{1-x}-(MoO₃)_x system. In view of its influence on the crystallization, glass transition kinetics and electrical transport for temperatures, $T_g \leq T \leq T_c$, a systematic study has been performed.

The compositions 50AgI-33.33Ag₂O-16.67 {(MoO₃)_x-(V₂O₅)_{1-x}} for x=0.1, 0.15, 0.20, 0.25, 0.30 and 0.40 (corresponding to 1.67, 2.5, 3.33, 4.17, 5 and 6.67 m/o of MoO₃ in AgI-Ag₂O-V₂O₅ system, respectively) were chosen and abbreviated as 10, 15, 20, 25, 30 and 40SISOVOMO, respectively, for the present investigation.

5.1. Structural studies

5.1.1. X-ray diffraction

At the outset, all the melt quenched samples till x = 0.30 do exhibit halo patterns in the X-ray diffraction (XRD) and hence found to be glassy in nature (Fig. 5.1 a and 5.2 a and c). The glass forming region for this system is found to be narrow and the SISOVOMO samples for x \geq 0.4 exhibit crystalline nature. The XRD patterns for one of these, viz. 30 SISOVOMO melt-quenched as well as annealed after melt quenching (at T > T_c) are shown in Fig. 5.1. When 30 SISOVOMO is annealed above the temperature of complete crystallization (at 150 °C), significant peaks appear in the XRD pattern (Fig 5.1b) that correspond to precipitation of two compounds, viz. Ag₄V₂O₇ (minor) and Ag₈I₄V₂O₇ (major).

The XRD patterns of 15 and 25SISOVOMO annealed samples (Fig. 5.2 b and d) do confirm the major precipitation of Ag₈I₄V₂O₇ compound. It is apparent that amount of Ag₈I₄V₂O₇ remain almost constant and independent of MoO₃ content.

The typical average particle size of precipitated crystallites is calculated using Debye- Scherer formula and found to be ~ 30-40 nm. Moreover, since there is no precipitation of molybdenum based compound, it may be suggested that such a possible compound may be

either in very small amount or the annealing is unable to eliminate the MoO_3 from the glassy phase. Similarly, it was also proposed that heating the glass above T_c may not completely eliminate amorphous state (Dalvi et al, 2002).

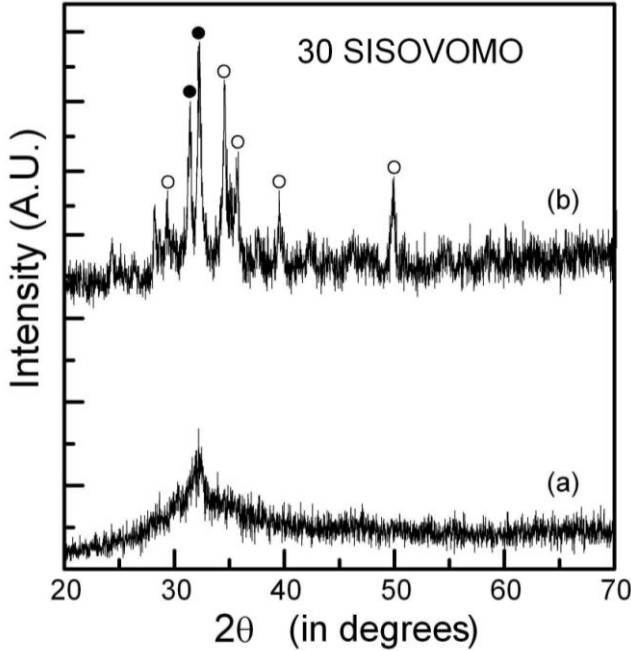


Fig. 5.1: The XRD patterns for 30SISOVOMO sample (a) as prepared glass and (b) glass-ceramic composites. Symbols denote: (○) $\text{Ag}_8\text{I}_4\text{V}_2\text{O}_7$ and (●) $\text{Ag}_4\text{V}_2\text{O}_7$

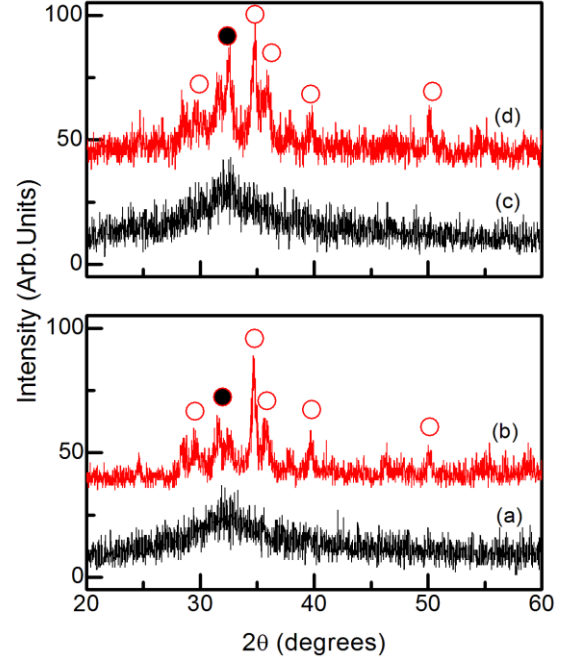


Fig. 5.2: The XRD patterns for 15SISOVOMO sample (a) as prepared glass and (b) glass-ceramic composites. 25SISOVOMO sample (c) as prepared glass and (d) glass-ceramic composites. Symbols denote: (○) $\text{Ag}_8\text{I}_4\text{V}_2\text{O}_7$ and (●) $\text{Ag}_4\text{V}_2\text{O}_7$

5.1.2. Scanning electron Microscopy

Scanning electron microscopy (SEM) results are obtained for all these composition and shown here for 10 and 30SISOVOMO in Fig. 5.3.

As apparent, almost homogeneous background dispersed with very fine nanoparticles is visible in as prepared (glassy) samples for 10SISOVOMO as well as for 30SISOVOMO. On the other hand, glass-ceramic samples of these compositions exhibit a significant phase separation and growth of nano crystallites within the glass matrix.

Interestingly, the SEM results for glass-ceramic nanocomposites are different for 10 and 30 SISOVOMO. For 10 SISOVOMO, well separated crystallites are seen, whereas, for 30 SISOVOMO these precipitated crystallites are small and uniform in size, and suggest a

homogeneous growth with large grain boundary region. It may be suggested here that low MoO_3 content samples exhibit a growth dominated, whereas high MoO_3 content samples exhibit a nucleation dominated process of crystallization.

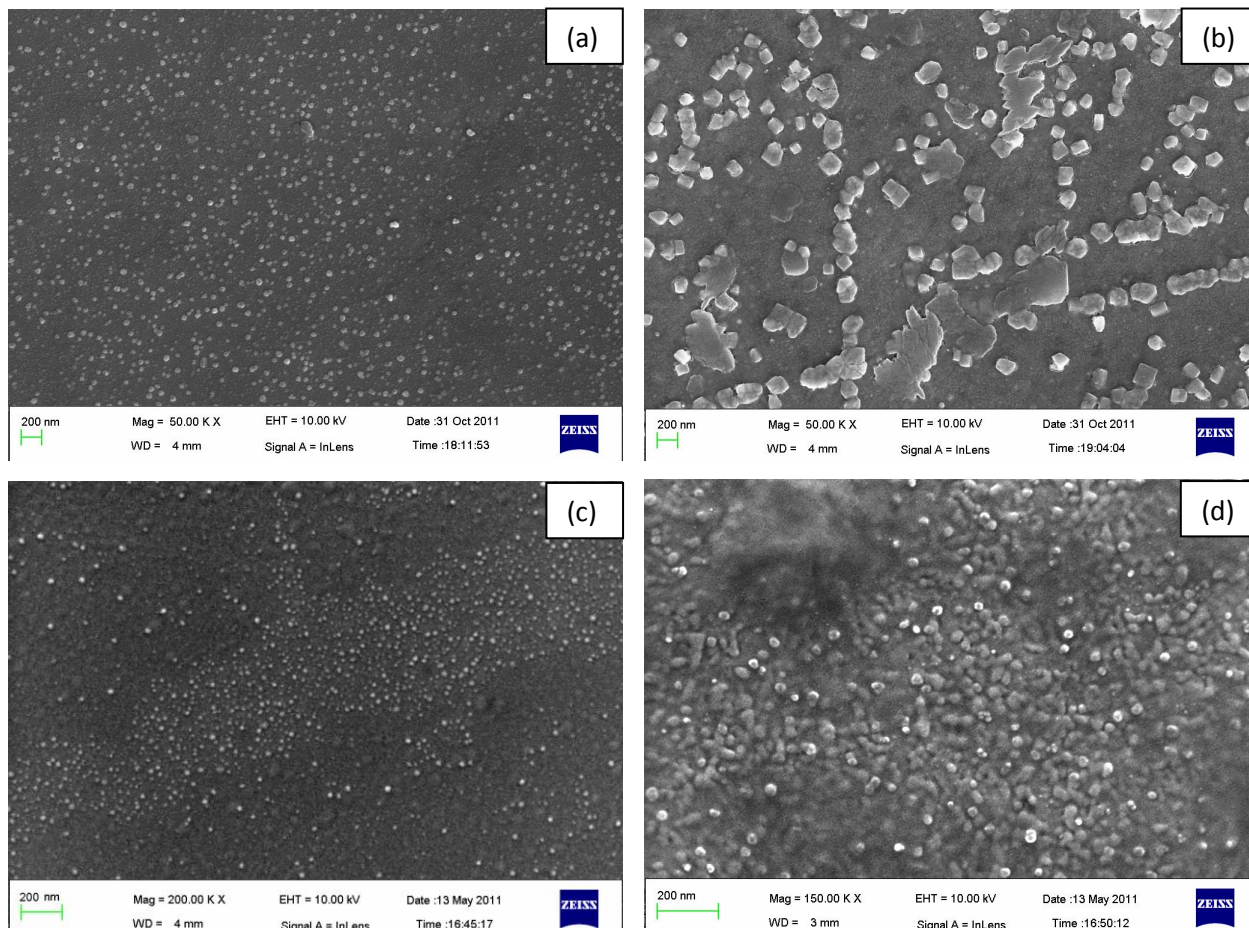


Fig. 5.3: SEM results for glassy and glass ceramic samples for 10 (a and b) and 30 (c and d) SISOVOMO.

The particle size obtained from these images is again found to be $\sim 30\text{-}40\text{nm}$ which is in agreement with size obtained from XRD results.

5.2. Differential Scanning calorimetry

DSC patterns for all the samples at a heating rate of 10 °C/min are shown in Fig. 5.4. Apparently, unlike the system discussed in chapter 3 and 4, this exhibits almost a single crystallization peak (100-120°C) and apparent T_g in the range of ~ 70-80 °C.

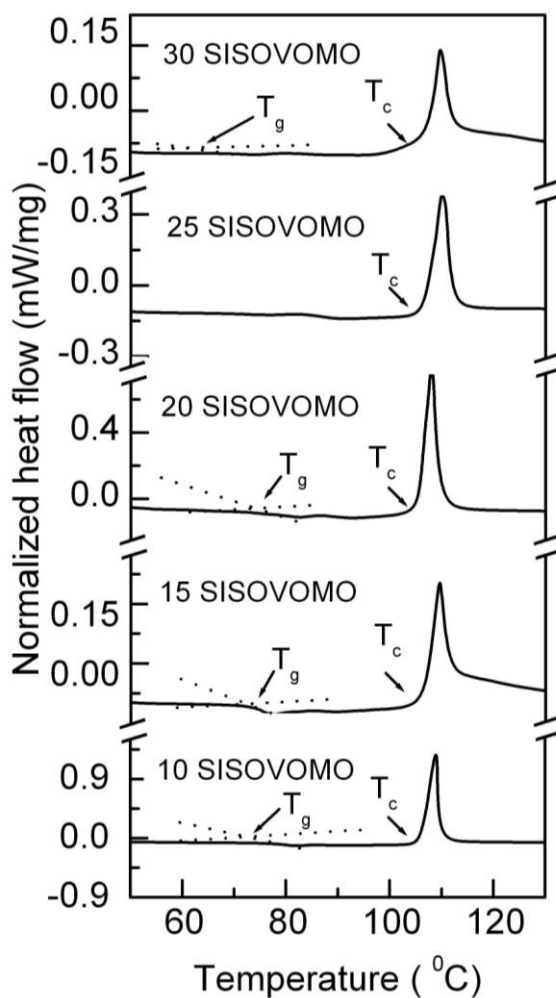


Fig. 5.4: DSC scans at a typical heating rate of 10⁰C/min for the glassy system 50 AgI- 33.33Ag₂O-16.67[(V₂O₅)_{1-x}-(MoO₃)_x] (x = 0.1-0.3)

Thus, existence of T_g and T_c in DSC scans confirm that all these samples are purely glassy in nature and undergo single stage precipitation.

Further, the T_g and T_c do not change significantly with MoO_3 addition. Such a weak dependence of T_g and T_c has also been seen in $\text{AgI-Ag}_2\text{O-V}_2\text{O}_5$ system with another glass former (P_2O_5) addition (Garbarczyk et al, 2000). The thermal stability of these glasses is further studied as a function of MoO_3 content. From DSC scans T_c-T_g values are obtained and given in Table 5.1. It may be noticed that MoO_3 addition does not change $T_c - T_g$ appreciably. Furthermore, the second thermal stability parameter Hruby coefficient (k_{gl}) also remains almost constant with MoO_3 addition (Table 5.1).

The enthalpy release (ΔH) during the amorphous \rightarrow crystalline transition is also obtained from the area under the exothermic (crystallization) peak and used as a third thermal stability parameter (also given in Table 5.1). The value of ΔH is found to be constant with MoO_3 content within the experimental error and clearly suggests that MoO_3 substitution in the SISOVO matrix does not affect the disorder in the glass matrix significantly for the compositions well within the glass forming region. Thus, it may be suggested here that the degree of disorder in these samples is almost constant with the addition of MoO_3 . The above discussed three criteria suggest that the thermal stability of these glassy samples is unaffected by MoO_3 addition in the matrix within the glass forming region ($x \leq 0.4$).

Table 5.1: Characteristics temperatures, total enthalpy release during the crystallization and E_s and E_c values obtained from Moynihan and modified Kissinger equation, respectively, in the SISOVOMO system.

X	T_c-T_g (°C)	k_{gl}	ΔH (J/gm)
0	26	0.23	92 ± 5
0.1	27	0.24	90 ± 5
0.2	30	0.32	80 ± 4
0.3	27	0.3	85 ± 4
0.4	26	0.28	89 ± 5

5.2.1. Glass transition and crystallization kinetics

Fig. 5.5a and b shows the DSC scans performed at different heating rates viz. 5, 10, 15 and 20 °C/min for the sample 10 and 30 SISOVOMO, respectively. As discussed, for both the samples DSC scans exhibit single crystallization. It is readily noticed, the glass transition (T_g) and the crystallization peak temperature (T_p) shift monotonically to higher values as the heating rate increases.

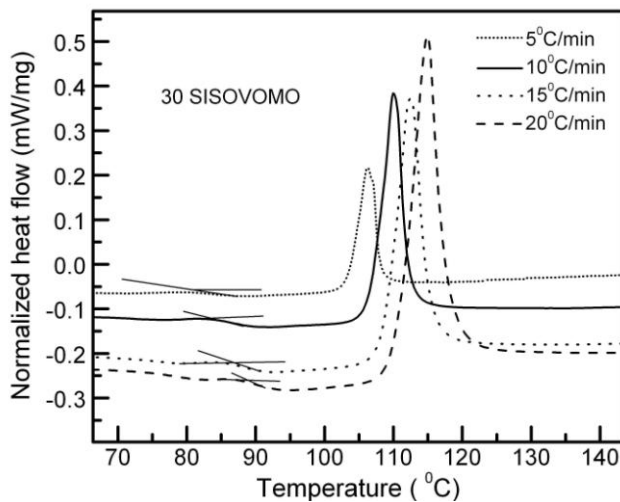


Fig. 5.5a: DSC scans for 30SISOVOMO at the various heating rates, viz. 5, 10, 15 and 20°C/min.

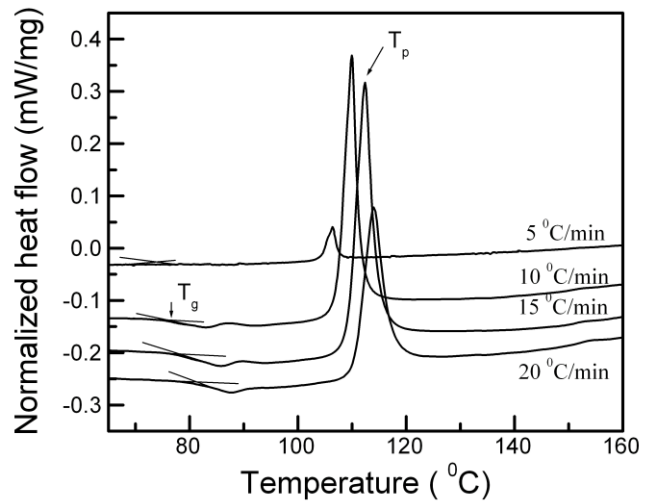


Fig. 5.5b: DSC scans for 10SISOVOMO at the various heating rates, viz. 5, 10, 15 and 20°C/min.

Using the Moynihan eq., the activation energy of structural relaxation is obtained. The plot of $\ln q$ versus inverse of T_g is shown in Fig. 5.6 for 10, 20 and 30 SISOVOMO samples. The E_s value is obtained from the slope for many close-by compositions well within glass forming region and plotted in Fig. 5.7 as a function of MoO_3 content. Interestingly, the E_s value does not show appreciable change till $x = 0.1$, further shows a minimum at $x = 0.2$ and subsequently a notable rise till $x = 0.3$.

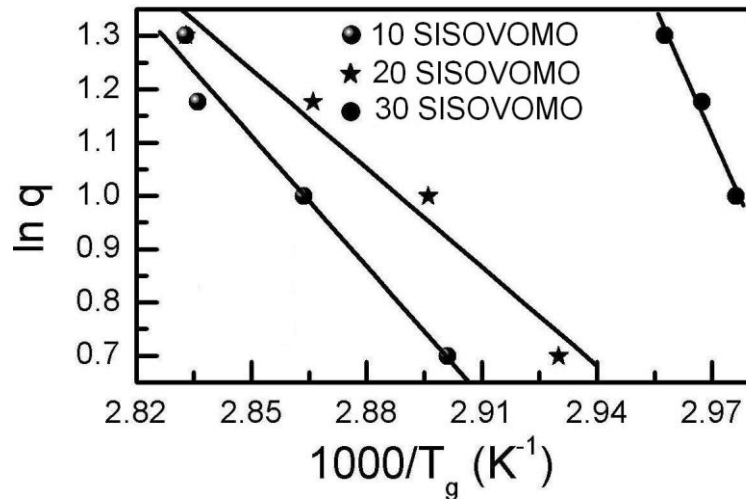


Fig. 5.6: Moynihan plots for 10, 20 and 30 SISOVOMO samples.

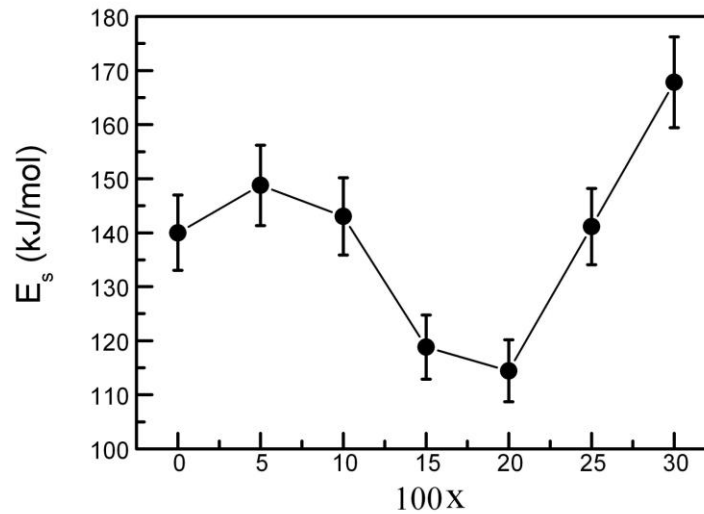


Fig. 5.7: The E_s values (obtained from Moynihan plots) as a function of MoO₃ content.

Since the crystallization peak is single Matusita Sakka equation is used to get information about E_c as well as order parameter (n) and dimensional growth (m). As already discussed, m and n related as for example, n = 1 (m is also defined equal to unity) follows surface nucleation, whereas, n = 2, 3 and 4, respectively correspond to one, two and three dimensional growth of nuclei (Matusita and Sakka, 1975).

The order parameter (n) of the crystallization is evaluated by Ozawa method (Ozawa, 1986).

The value of α is calculated from the ratio of the area of the exothermic crystallization peak till a temperature within the peak $T \geq T_c$ to the total area of peak. Using Eq. 4 and plotting $\ln[-\ln(1-\alpha)]$ versus $\ln q$, n is obtained for many nearer compositions within the glass forming region. Here the fractional area of the peak is taken upto a temperature $T = 106^\circ\text{C}$ (a temperature within crystallization peak that is close to T_c). For clarity $\ln(-\ln(1-\alpha))$ vs $\ln q$ plot is shown for three compositions in Fig. 5.8. Avrami parameter (n) is evaluated from the slope as discussed in chapter 2. It is readily noticed that order parameter, n , as a function of MoO_3 content decreases significantly from 3.7 to 2.4 (Fig. 5.9).

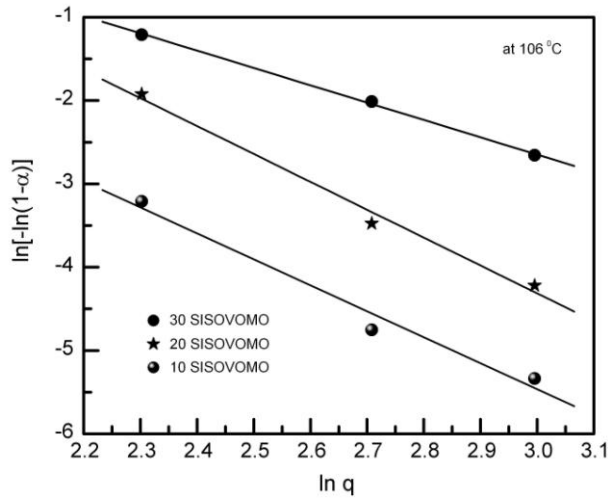


Fig.5.8: $\ln\{-\ln(1-\alpha)\}$ versus $\ln q$ plots for 10, 20 and 30 SISOVOMO for $T = 106^\circ\text{C}$

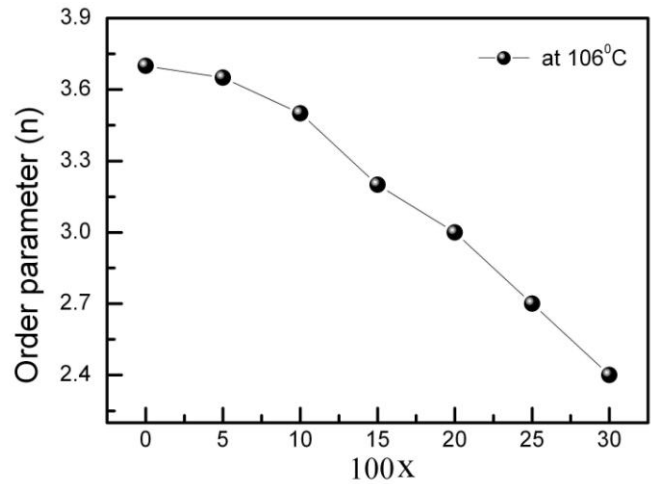


Fig. 5.9: Order parameter (n) with MoO_3 content

According to equation (3), $\ln q^n/T_p^2$ versus inverse of temperature has been plotted for corresponding values of n in Fig. 5.10. Here the values of n are taken for respective MoO_3 content samples as calculated from Fig. 5.8 and shown in Fig. 5.9. From slope of Fig. 5.10, the activation energies associated with crystallization are obtained for all the pure glassy samples.

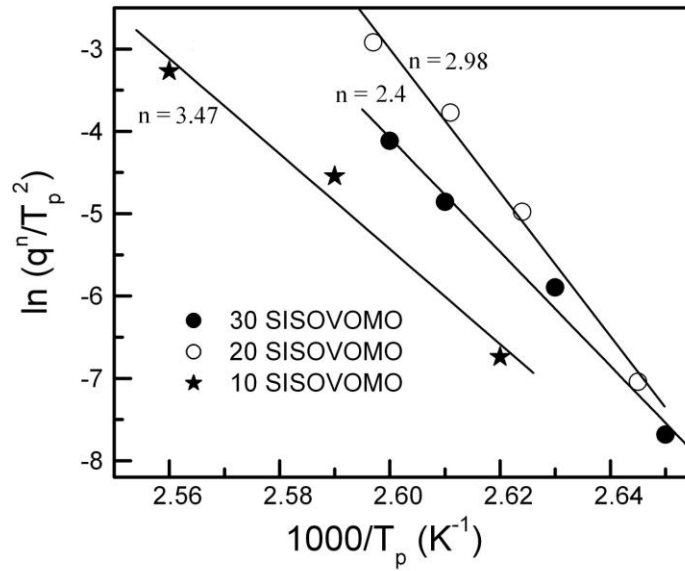


Fig. 5.10: Modified Kissinger plot for 10, 20 and 30 SISOVOMO.

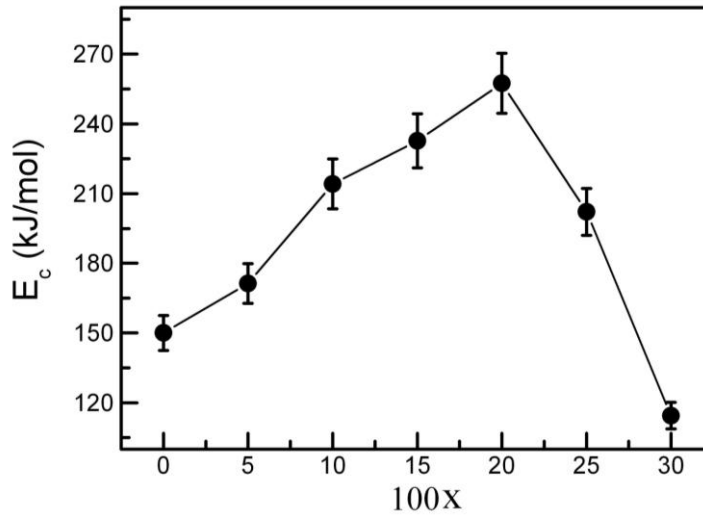


Fig. 5.11: The E_c values obtained from Modified Kissinger Equation as a function of MoO_3 .

The activation energy for crystallization, obtained from the Eq. (3) is plotted in Fig. 5.11. As evident from Fig. 5.11, E_c values tend to increase with MoO_3 content upto 20 SISOVOMO ($x = 0.2$).

As apparent from Fig. 5.11 and Fig. 5.7, E_s and E_c values show opposite trends. Such interesting opposite trends are also found in $AgI-Ag_2O-V_2O_5$ system with AgI addition in an

earlier work. To further analyze E_s and E_c trends and thermal stability, the electrical conductivity is studied above T_g and T_c .

5.3 Electrical Conductivity

To examine the thermal events, alternatively, conductivity - temperature cycles are carefully obtained ($1^\circ\text{C}/\text{min}$) and studied in the thermally unstable region i.e. $T \geq T_g$ and $T \geq T_c$. As already discussed in section 5.2, the enthalpy change (ΔH) and other thermal stability parameters do not vary with MoO_3 significantly, it is expected that degree of disorder is also comparable in all MoO_3 substituted samples and thus it is not surprising that the room temperature conductivity of the glasses does not show appreciable change with MoO_3 addition (Fig. 5.12).

The electrical conductivity is plotted as a function of temperature for 50 SISOVO and 10-30 SISOVOMO glassy samples in Fig. 5.12a, c, e and g. Firstly, unlike the previously studied two system, σ -T plot exhibits similar trend for all the samples. The σ -T cycles are perfectly reversible up to the temperature $T \leq T_g$ (region I). Apparently, the conductivity increases as a function of temperature Arrheniusly till $\sim 74^\circ\text{C}$. Above T_g it shows notable deviation from linearity followed by drastic fall from $\sim 100 - 105^\circ\text{C}$ till $\sim 125 - 135^\circ\text{C}$ due to crystallization. Further, the conductivity saturates that may correspond to completion of crystallization process.

The conductivity behavior in this thermally unstable region (II) again can be explained using crystallite by pass model. As discussed in previous sections 3.4 and 4.4, the drastic fall in the conductivity may be due to precipitation of poor ion conducting $\text{Ag}_8\text{I}_4\text{V}_2\text{O}_7$. Since the amount of this compound remains almost constant hence fall in conductivity is witnessed in all the compositions at T_c , unlike the previously studied two systems.

On further heating, conductivity again increases linearly that suggests pure ionic nature of the crystallized compounds.

The σ -T cycles of the glass-ceramic samples are shown in Fig. 5.12 b, d, f and h. For all, the conductivity exhibits almost reproducible Arrhenius behavior in the complete range (30 - 165°C). This suggests ionic nature of the glass-ceramics.

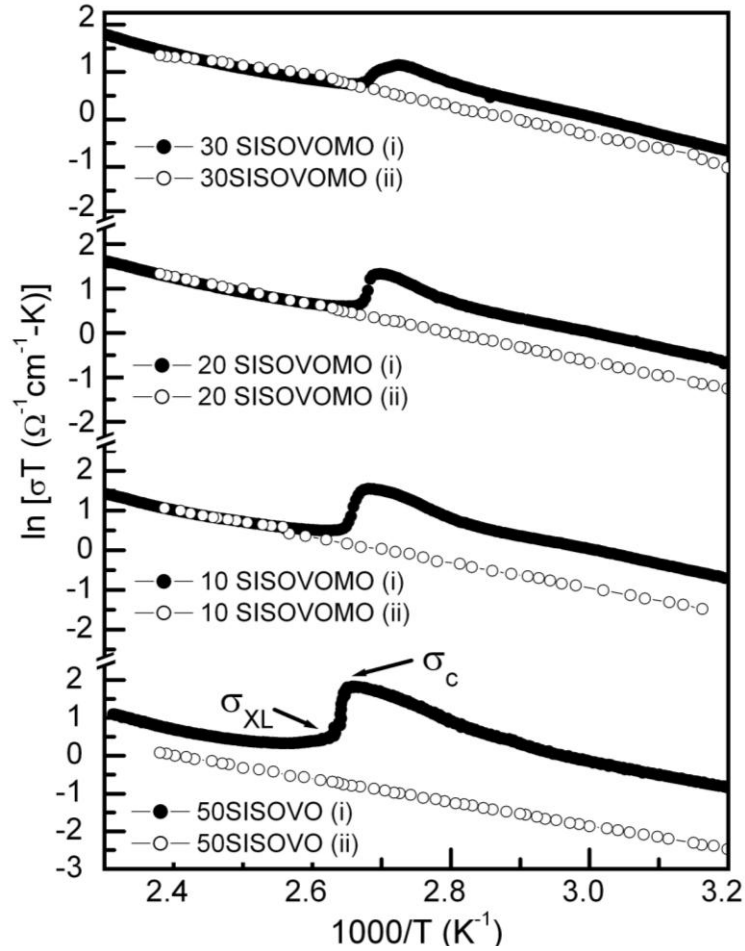


Fig. 5.12: Electrical conductivity versus inverse of temperature for various compositions at a heating rate of $1^{\circ}\text{C}/\text{min}$. The conductivity at peak and after crystallization are shown as σ_c and σ_{XL} , respectively for one of compound. Symbols denote (●) First cycle and (○) second cycle.

The room temperature conductivity of the glass-ceramics is plotted as a function of MoO_3 content along with the activation energy (E_a) of these second cycles (Fig. 5.13). Interestingly, conductivity increases with MoO_3 addition till $x = 0.3$ where it reaches a maximum value of $\sim 10^{-3} \Omega^{-1}\text{cm}^{-1}$ and drops subsequently. Moreover, conductivity and activation energy exhibit opposite trends. It may be again emphasized here that conductivity of glass is almost independent, whereas, that of glass-ceramic exhibits enhancement with MoO_3 content in the matrix. The glass-ceramic may be thought of crystallites of $\text{Ag}_8\text{L}_4\text{V}_2\text{O}_7$ surrounded by

connective tissues. It is likely that due to possible nucleation dominated crystallization the effective grain boundary fraction may have increased for higher MoO₃ samples (Indris et al, 2000) and may be responsible for conductivity rise in glass-ceramic nano composite samples.

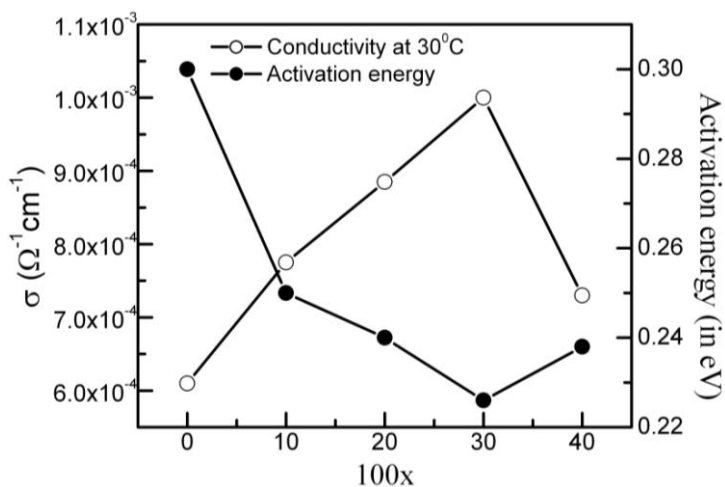


Fig. 5.13: The electrical conductivity (at 333K) and activation energy for second heating cycle as a function of MoO₃ content.

5.4. Electrochemical cell characteristics

Fig. 5.14 shows constant load characteristics for 30SISOVOMO glass-ceramic samples at various loads (viz, 10, 20 and 50kΩ). The open circuit voltage for these glass-ceramic samples are found to be ~ 0.685 and remains constant for more than 24 hrs. There is an initial fall in cell voltage for lower loads (10, 20 kΩ), which may be due to polarization and/or formation of AgI layer at the interface.

The cell voltage is practically constant over a 96hrs at high load viz. 50 kΩ or low current drop for these glass-ceramic samples.

Again, for lower external load (10, 20 kΩ), the cell voltage decreases gradually but stabilizes later on for these electrochemical cells. Thus, it is concluded here that these samples are stable under the battery conditions.

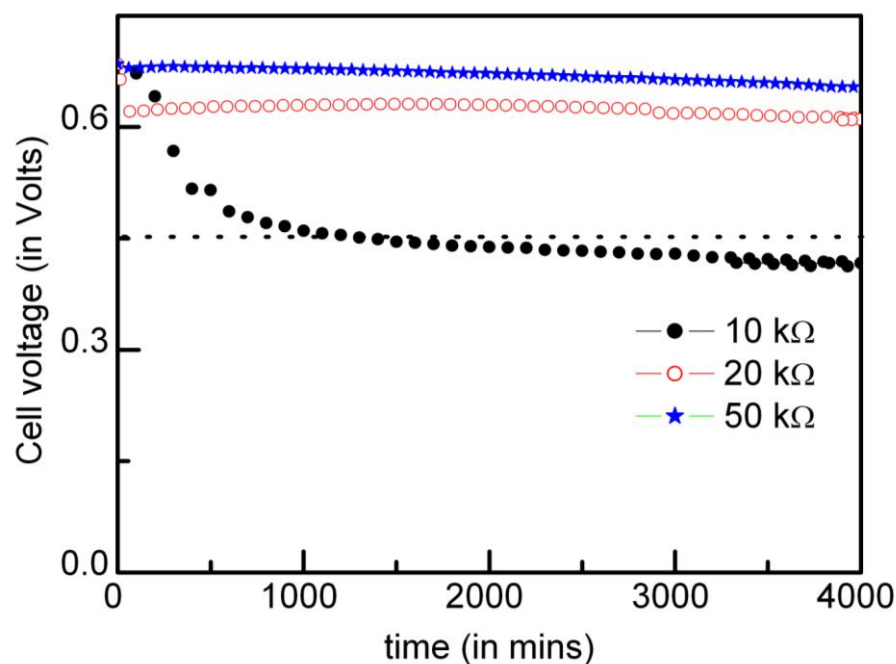


Fig. 5.14: Constant load characteristics for external loads for Ag/I₂ electrochemical cells with 30SISOVOMO sample as electrolyte

5.5. Conclusions

1. The effect of MoO₃ substitution in AgI-Ag₂O-V₂O₅ superionic glasses reveals interesting results. XRD results do infer that annealing of these glassy samples is (i) Either unable to eliminate the molybdenum based compound from glassy phase, or (ii) any MoO₃-based crystalline compound formed is in very little amount. It is apparent from XRD and conductivity results that the amount of precipitation of Ag₈I₄V₂O₇ remains almost constant and independent of MoO₃ content. It is also found that MoO₃ addition does not affect the thermal stability and enthalpy content significantly in the glass forming region. Nevertheless, it strongly influences the E_s (at T_g) and E_c values. The E_s and E_c values exhibit opposite trends with MoO₃ addition.

2. The glass-ceramic samples do exhibit nano composite nature, as revealed by XRD and SEM results. The conductivity of the glassy samples found to be not influenced by the composition variations. However, that of the crystallized (glass-ceramic) samples is surprisingly found to be increasing with MoO₃ addition. The highest conductivity for

crystallized samples is found to be $\sim 10^{-3}\Omega^{-1}\text{cm}^{-1}$ at room temperature which is comparable to and even higher than some of the SISOVO glass compositions. The rise in the conductivity with MoO_3 content of glass-ceramic samples may be due to nucleation dominated crystallization that eventually increases the effective grain boundary fraction.

3. The glass-ceramic samples exhibit good electrochemical stability and thus useful in low power ionic devices.

CHAPTER 6

Methods developed during work

This chapter discusses a new and extremely sensitive method, viz. electrical conductivity versus temperature cycles at various controlled heating rates, to study the crystallization and glass transition kinetics in the superionic glasses. As discussed in previous chapters, during the thermal characterization, the attention was to measure σ –T cycles in thermally unstable region. Thus, the thermal events (T_g , T_c) could be very well observed in the σ –T cycles. It is examined that how effectively these obtained parameters could be effectively used to (i) quantitatively study the crystallization, glass transition kinetics and therefore (ii) to calculate the activation energies for structural relaxation (E_s) and crystallization (E_c).

For the present investigation, the new method is attempted on the following two systems and for the compositions where crystallization is apparent, single and less ambiguous:

- (i) 10-30 SISOVOMO (ii) 0-10 CI-SISOVO

6.1 The method

In this method the electrical conductivity is very carefully measured at various rates (0.5 - 7°C/min). Those compositions were chosen in which the electrical conductivity significantly deviates from Arrhenius behavior at T_g and falls drastically at the crystallization. The thermal events and the shift of T_c and T_g are carefully monitored. The details are discussed for two of the systems.

(i) Studies on SISOVOMO

6.1.1 Electrical Conductivity-Temperature cycles

As already discussed in the previous chapter 5, SISOVOMO system exhibits apparent glass transition and a single crystallization peak in the DSC patterns. The electrical conductivity-temperature cycles do exhibit anomalous rise in the conductivity at T_g and drastic fall at T_c . For one typical heating rate of 5°C/min. DSC scans and electrical conductivity-temperature cycles are shown for a comparison for three of the compositions viz., 10, 20 and 30 SISOVOMO in Fig. 6.1. Apparently, T_c , T_g and T_c - T_g values obtained from differential scanning calorimetry (DSC)

and conductivity-temperature ($\sigma - T$) cycles are close and this result motivated to further scrutinize the $\sigma - T$ cycles at various rates.

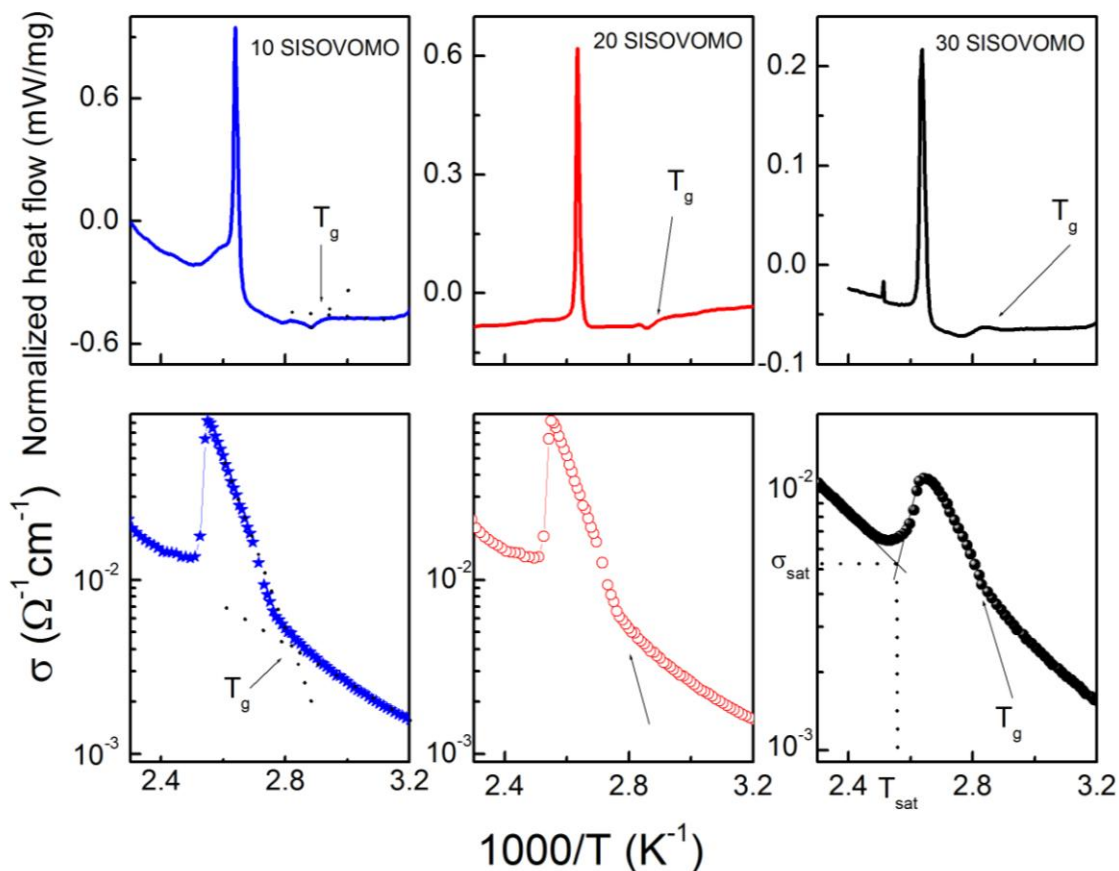


Fig. 6.1: DSC scans and σ -T cycles at a typical heating rate of $5^\circ\text{C}/\text{min}$ for 10, 20 and 30 SISOVOMO.

The $\sigma - T$ cycles were obtained for various heating rates as low as $0.5^\circ\text{C}/\text{min}$ and high as $7^\circ\text{C}/\text{min}$. For the kinetics of crystallization and glass transition, electrical conductivity versus temperature cycles obtained at various heating rates are shown in Fig. 6.2. Interestingly, observed T_g and T_c in $\sigma - T$ plots do shift monotonically towards higher temperatures with increasing ramps. It is important to note that generally it is not possible to see the glass transition very apparently for lower rates (e.g. $1\text{K}/\text{min}$ or less) in the DSC scans. Whereas, the thermal events are very much apparent in $\sigma - T$ cycles even for rates as low as $0.5\text{K}/\text{min}$.

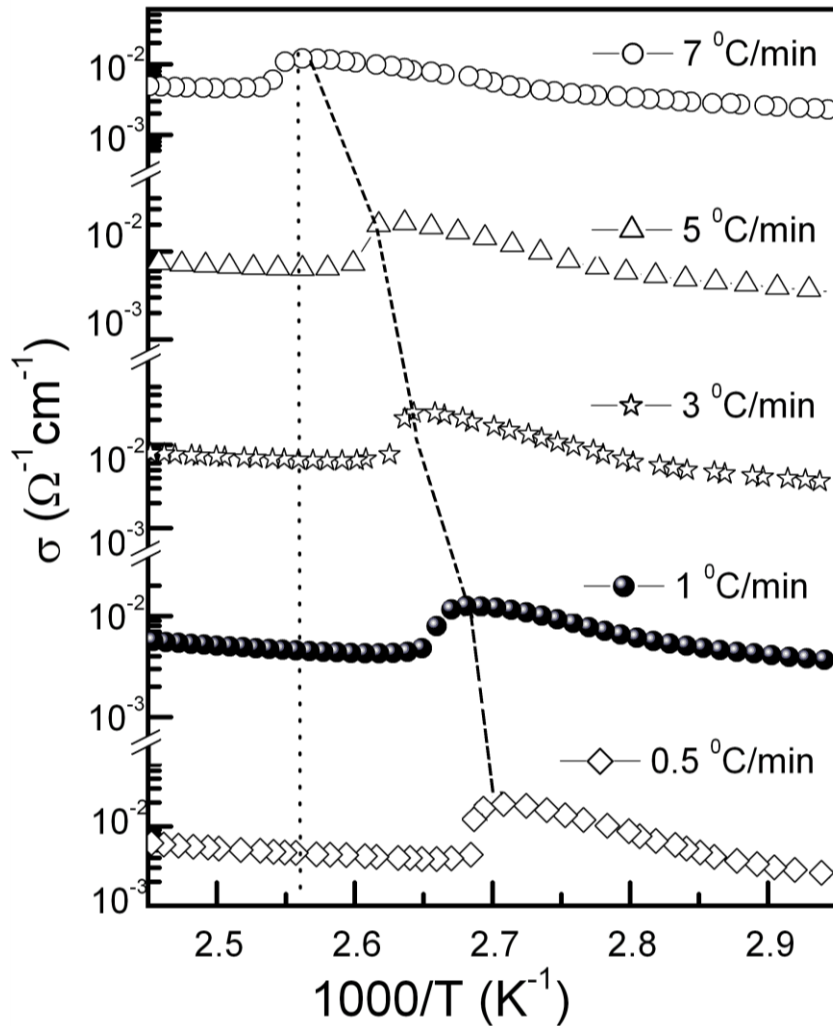


Fig. 6.2: Electrical conductivity versus inverse of temperature at various heating rates 0.5, 1, 3, 5 and 7 K/min for 20 SISOVOMO. The dotted line joins conductivity peak positions that shift towards higher temperatures

Examining the behavior of $\sigma - T$ cycles between two important temperatures T_c and T_{sat} , the T_p values are obtained for crystallization kinetics studies. Here T_{sat} is defined as temperature where the conductivity saturates instantly after a drastic fall at T_c . The σ vs $1/T$ plot between these two temperatures is shown for one of the sample 20 SISOVOMO in the inset of Fig. 6.3 at $1^\circ\text{C}/\text{min}$. Further, derivative of conductivity shows a maximum and its corresponding temperature is taken as T_p .

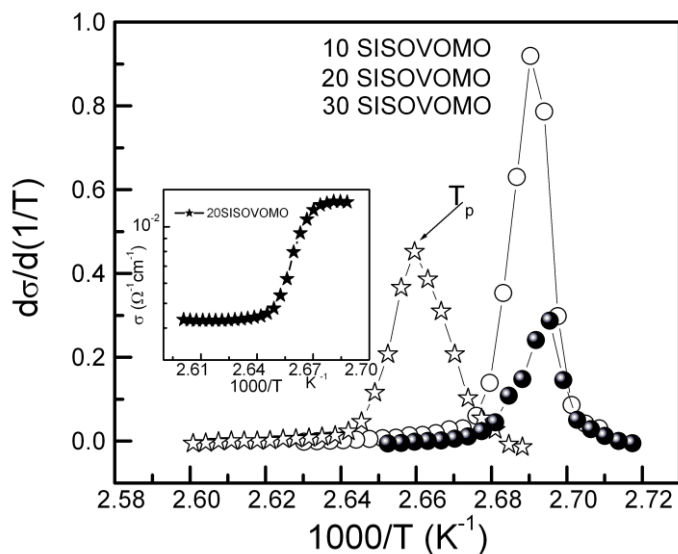


Fig. 6.3: Derivative of σ - $1/T$ cycles for the determination of the peak temperature (T_p). Inset: Electrical conductivity vs inverse temperature on an extended scale in the range $T_{\text{sat}} \geq T \geq T_c$ for a typical heating rate of $1^\circ\text{C}/\text{min}$.

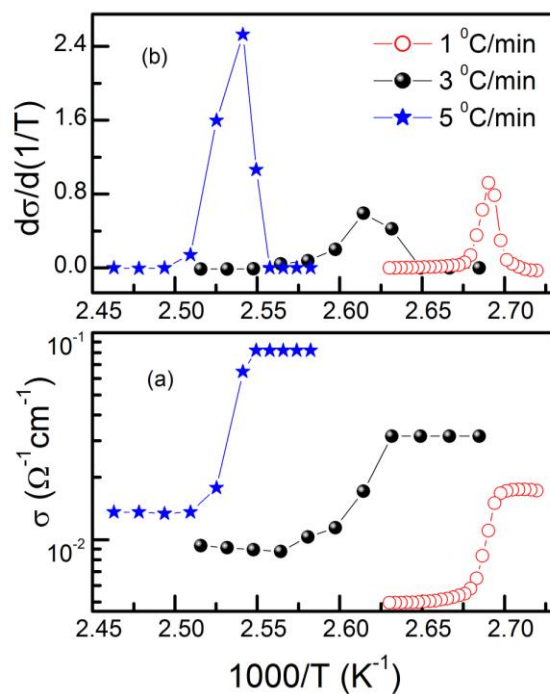


Fig. 6.4: (a) For 20SISOVOMO electrical conductivity vs inverse temperature on an extended scale in the range $T_{\text{sat}} \geq T \geq T_c$ (b) Derivative of σ - $1/T$ cycles for the determination of the peak temperature (T_p) at various heating rates.

Fig. 6.3 shows the differential conductivity as a function of inverse of temperature for all the three samples for a typical rate of 1 °C/min. Similarly, T_p values for each sample at various other rates are also calculated and shown in Fig. 6.4. Using T_p and T_g values obtained from $\sigma - T$ plots, the $\ln q$ versus $1/T_g$ and $\ln (q/T_p^2)$ versus inverse of T_p are plotted in Fig. 6.5.

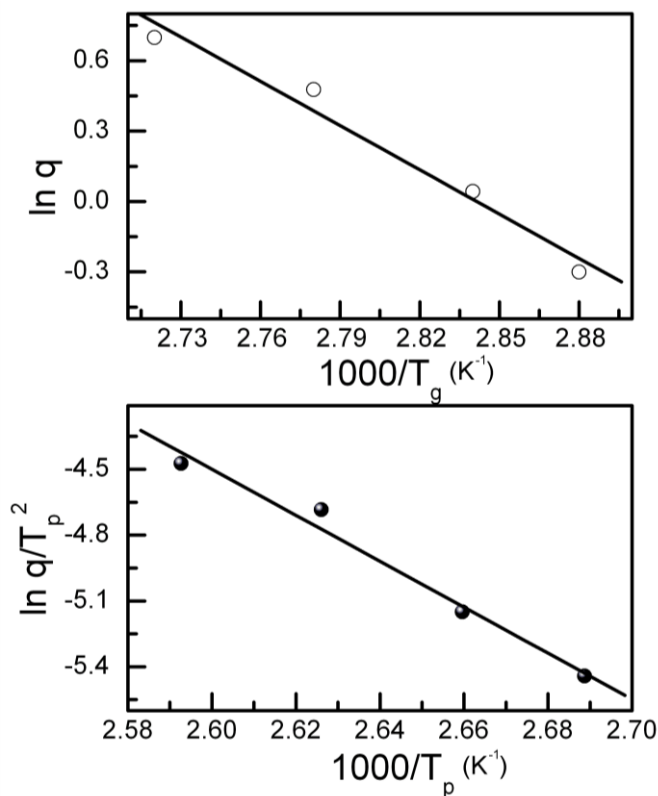


Fig. 6.5: Moynihan (a) and Kissinger (b) plots for 20 SISOVOMO obtained from $\sigma - T$ cycles.

Interestingly, both the plots are apparently linear. From the slope, using the Eqs. 2.11 and 2.12, the E_s and E_c are calculated. All these values thus obtained from $\sigma - T$ cycles and DSC scans are presented in Table 6.1. Interestingly, these values obtained from $\sigma - T$ cycles are in good agreement with those of determined from differential scanning calorimetry.

Table 6.1: Different thermal parameters obtained from Differential scanning calorimetry and conductivity-temperature cycles with MoO₃ content

X	T _g /K		T _c /K		E _s /kJ/mol		E _c /kJ/mol		T _{rg}		k _{gl}	
	σ- T cycles	DSC	σ- T cycles	DSC	σ- T cycles	DSC	σ- T cycles	DSC	σ- T cycles	DSC	σ- T cycles	DSC
0.1	355	351	391	380	160±15	140±15	235±25	210±20	0.37	0.35	0.27	0.28
0.2	353	359	381	378	130±13	118±12	280±30	250±25	0.36	0.34	0.26	0.27
0.3	350	335	378	373	200±20	170±17	135±15	110±10	0.36	0.33	0.25	0.25

(ii) 50{CuI_x-AgI_{1-x}} 33.33 Ag₂O-16.67V₂O₅ (CI-SISOVO) system

The thermal investigations using σ –T cycles were also performed on CI-SISOVO but only for low content of CuI samples, where system is less complex in nature.

To perform these kinetics, σ –T cycles obtained at various heating rates are shown in Fig. 6.6. It is once again evident from the figure that T_g, T_c are shifted towards higher temperature as the heating rate increases. The peak temperature, where the crystallization rate is maximum, is obtained from the differentiation of σ –T cycles for T_{sat} ≤ T ≤ T_c as shown in Fig. 6.7.

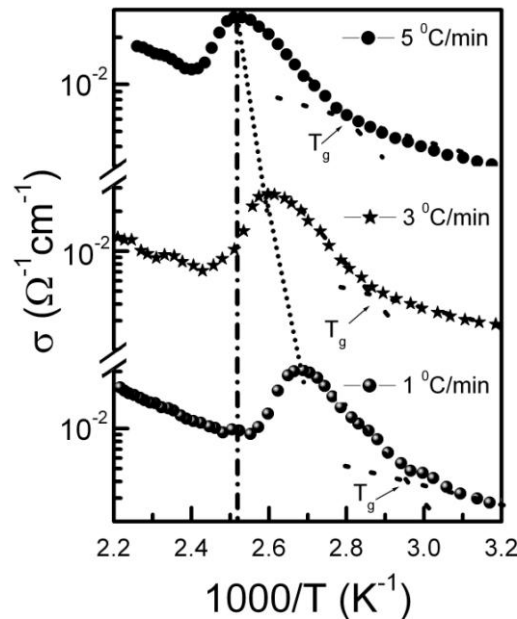


Fig. 6.6: Electrical conductivity versus inverse of temperature at various heating rates 0.5, 1, 3, 5 and 7 K/min for 10 CI-SISOVO. The dotted line joins conductivity peak positions that shift towards higher temperatures

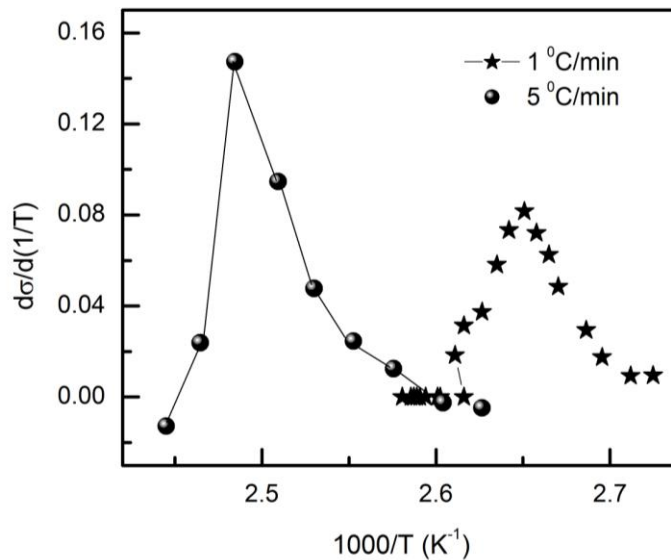


Fig.6.7: Derivative of σ - $1/T$ cycles for the determination of the peak temperature (T_p) at various heating rates for 10 CI-SISOVO

The T_g and T_p values obtained from these σ - T cycles are again used to calculate the activation energies for structural relaxation at T_g (E_s) and crystallization (E_c). The plots $\ln q$ vs $1000/T_g$ and $\ln q/T_p^2$ vs $1000/T_p$ are found to be linear (Fig. 6.7) whose slope yield the values of E_s and E_c as tabulated in Table 6.2.

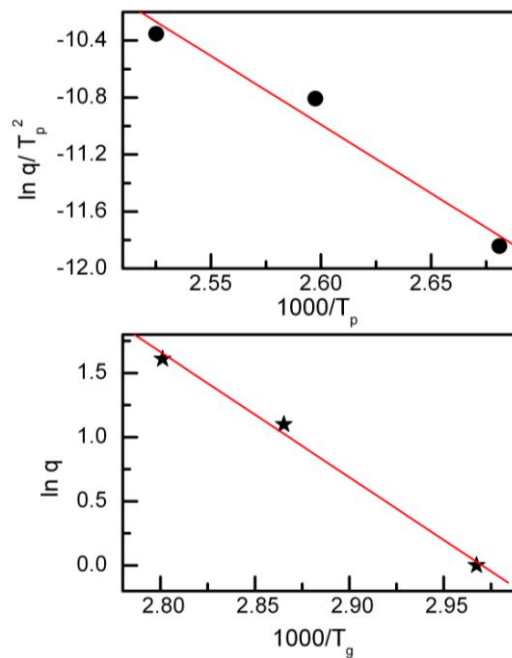


Fig. 6.8: Moynihan (a) and Kissinger (b) plots for 10 CI-SISOVO obtained from σ - T cycles.

Interestingly, these values obtained from σ - T cycles are also in good agreement with those of determined from differential scanning calorimetry for this system.

Table 6.2: Different thermal parameters obtained from Differential scanning calorimetry and conductivity-temperature cycles with CuI content

X	T_g /K		T_c /K		E_s / kJ/mol		E_c / kJ/mol	
	σ - T cycles	DSC	σ - T cycles	DSC	σ - T cycles	DSC	σ - T cycles	DSC
0	343	349	376	375	150±15	130±13	160±16	145±15
0.05	358	360	390	395	200±20	210±21	190±19	150±15
0.1	353	357	383	390	190±20	220±22	180±18	140±14

6.3 Conclusions:

1. The thermal stability parameters obtained from σ - T cycles are in good agreement with those of determined from differential scanning calorimetry scans. The E_s and E_c values and their trend with composition obtained from both methods are comparable within experimental error.
2. Thus our results strongly suggest that electrical conductivity versus temperature cycles at various controlled heating rates can be successfully used to examine the thermal behavior and stability of the superionic glasses. In addition, for these Ag^+ ion conducting superionic glasses for lower heating rates, σ - T cycles are found to be more sensitive than DSC scans. Such cycles are especially useful for samples (i) which show single crystallization and (ii) for which $T_c - T_g$ is high.
3. Finally, as a future prospective, such σ - T cycles may be extremely useful in thermal characterization of ion conducting glassy/amorphous thin films and multilayers where DSC measurements are ineffective due to small amount of the samples.

CHAPTER 7

Conclusions and future scope

7.1 Conclusions

In the present work fundamental Ag^+ ion conducting glassy and glass-ceramic superionic systems are investigated in view of their thermal stability. The applicability of the different thermal stability parameters has been examined e.g. Hrubby coefficient, activation energies associated with structural relaxation (E_s) at T_g and crystallization (E_c), enthalpy content (ΔH) etc have been calculated and used to improve understanding of ionic glasses. These parameters were obtained by non-isothermal crystallization kinetics using differential scanning calorimetry, using Kissinger, Moynihan and Matusita-sakka formulations. Alternatively, some of these could also be obtained by analyzing the carefully measured electrical conductivity-temperature cycles above the T_g and T_c at various (30-300K/h) heating rates. Efforts were also to realize conductivity-structure relationship in the thermally unstable region. Thus electrical transport in the temperature range $T \geq T_g$ and $T \geq T_c$ has also been studied.

Another aspect of the present work was to prepare and characterize glass-ceramic nano composites in fundamental Ag^+ ion glasses by controlled crystallization.

A well-known fundamental glassy system $\text{AgI-Ag}_2\text{O-V}_2\text{O}_5$ was chosen to demonstrate the applicability of the parameters. Effect of (i) mixed cation i.e. CuI substitution in place of AgI (ii) mixed glass modifier Cu_2O in place of Ag_2O and (iii) mixed glass formers (MoO_3 in place of V_2O_5), on σ - T cycles, structural and especially thermal properties is thoroughly investigated. The results are found to be indeed interesting and this last chapter concludes the thesis.

Since, the electrical transport is of immense interest for the ionics community, hence different parameters, for the compositions exhibiting highest ionic conductivity in the three discussed systems are summarized in Table 7.1.

Table 7.1: Summary of thermal stability parameters and conductivity for best conducting glassy and glass-ceramic samples out of three chosen system											
System	Conductivity ($\Omega^{-1}\text{cm}^{-1}$)	T_g (in $^{\circ}\text{C}$)	T_c (in $^{\circ}\text{C}$)			E_s (kJ/mol)	E_c (in kJ/mol)			n	Thermal stability (in $^{\circ}\text{C}$)
			T_{c1}	T_{c2}	T_{c3}		E_{c1} (AgI)	E_{c2} ($\text{Ag}_4\text{V}_2\text{O}_7$)	E_{c3} ($\text{Ag}_8\text{I}_4\text{V}_2\text{O}_7$)		
30 CI-SISOVO glass	1.5×10^{-2}	60	110	130	150	90	90	150	215	1	60
30 CI-SISOVO glass-ceramic	2×10^{-3}	-	-	-	-	-	-	-	-	-	170
30 SICOSOVO glass	2×10^{-2}	50	95	-	-	170	160	-	-	-	50
30 SICOSOVO glass-ceramic	6×10^{-3}	-	-	-	-	-	-	-	-	-	150
30SISOVOMO glass	2×10^{-3}	77	110			170	100			2.4	77
30SISOVOMO glass-ceramic	1.5×10^{-3}	-	-	-	-	-	-	-	-	-	180

Interestingly, the glass-ceramic samples, though relatively poor conducting, exhibit much better thermal stability. The other conclusions are the following:

1. Study of thermal properties using non-isothermal kinetics is found to be very useful in our studies. The thermal stability parameters such as E_s and E_c exhibit interesting trends with compositional changes that provided immense understanding of crystallization in these systems. It is also revealed that in some cases such compositional changes and thermal treatment improve the stability by suppression of the crystallization.

The thermal treatment on glassy samples also leads to formation of new compounds with new and better properties. For example, in present study, for all these system, some of the glass-ceramic nano composites exhibit the ionic conductivity in order of $\sim 10^{-3} \Omega^{-1}\text{cm}^{-1}$ which is comparable to that of host glasses. Further, the glass-ceramic samples are found to be thermally more stable than those of glassy samples for the same composition.

2. Previously, few workers have successfully attempted to analyze the high temperature phases which precipitated during crystallization using in-situ XRD measurements. It is found in present study that XRD of glasses annealed near the crystallization temperature (T_c) also serves well as an alternative to examine the high temperature phases. Room temperature XRD results of these annealed glasses give meaningful information about evolution of the phases.

3. Along with XRD results, SEM measurements are also obtained accurately for glassy as well as glass-ceramic samples in the present study. These SEM results have given a better view and understanding of structural modification due to thermal treatment of these samples. The growth in the precipitated crystallites size or number of nuclei with different heat treatment infer about the crystallization mechanism in these systems.

These SEM results of glassy and glass-ceramic samples are in good agreement with those of XRD, DSC and conductivity results.

4. Previously, various researchers have studied the conductivity mostly below glass transition temperature (T_g). In this work σ -T cycles have also been studied extensively in the thermal unstable region. It has been brought out in the present study that such σ - T cycles are extremely useful as an alternative method to calculate the thermal stability parameters. Carefully measured σ - T cycles at various well controlled heating rates viz. 0.5 - 7 K/min exhibit monotonic shift of T_g and T_c towards the higher temperatures with increasing ramp.

Interestingly, the thermal events which are not visible in DSC scans at lower rates (2, 3 K/min) are found to be very well apparent in σ - T cycles at relatively much lower heating rates (0.5 K/min). The T_g and T_c values obtained from σ - T cycles at various heating rates are successfully used for non isothermal glass transition and crystallization kinetics. It is found that all these thermal stability parameters (E_s and E_c) exhibit similar trend as a function of composition and are comparable with those of obtained from DSC scans within experimental error.

Thus, σ - T cycles can be used accurately as an alternative method to obtain the thermal stability parameters for those system which exhibit a single crystallization. It should be emphasized here that for the systems where quantity (amount) is very small and DSC is ineffective, i.e., thin films, this method may be very useful.

5. On the basis of obtained XRD, DSC, σ - T cycles and SEM results, a model viz. crystallite by pass model inspired by cluster by pass model has been proposed in the present study to explain the ionic transport in the thermally unstable region. It is readily noticed that for temperatures $T_g < T < T_c$ there is formation of stable tiny crystallites surrounded by connective tissues. In both the growth and nucleation dominated crystallization process, on further heating (at the crystallization) all the connective tissue are blocked thus the conductivity drops. It is realized that the behavior of σ - T cycles at T_c is dictated by conductivity of tissues and crystallites. Our experimental findings support this model very well.

6. The ionic mobility plays an important role in the enhancement of ionic conductivity. The structural modifications that occur due to compositional changes preferably leads to such a mobility rise.

7. The glass-ceramic nanocomposites are found to be highly ion conducting, thermally stable and electrochemically stable under battery conditions. These are found to be potential candidates for low power ionic devices.

7.2. Future scope

The present work has been carried out on fundamental of Ag^+ ion glasses in the existing and accessible experimental facilities. These investigations do have future scope in many dimensions. Some of the possible scopes are given below:

- All the investigations have been carried out using non-isothermal kinetics. To study the thermal properties of these glasses and glass-ceramic nanocomposites on isothermal kinetics can also be performed for better understanding. Secondly, Modulated differential scanning calorimetry is another tool to study these thermal properties more accurately. Such studies can be certainly extended to glassy thin films of these superionic glasses which can give a new dimension to thin film ionics studies. Thus, such a compositional dependence of stability parameters will help the ionics community to choose better thermally stable samples. The melt aging effect i.e. effect of time given to melt a sample on these glasses can also be studied.
- The present investigation on thermal studies reveals that the glass-ceramic samples obtained from glassy samples are thermally more stable. Further, a systematic investigation on these glass-ceramic nanocomposites is desirable on applied functional materials e.g. Li^+ and Na^+ ion glasses. This systematic study may lead to development of thermally stable and highly ionic conducting glass-ceramics for devices. These glass-ceramic nanocomposites can also be prepared by external dispersion of nano particles and the effect of amount and size of these nano particles on these glasses can be studied for better understanding in future. Few more alternative techniques e.g. mechanochemical synthesis, microwave assisted synthesis may used for the preparation of glass-ceramics.
- In the present study, we have used conductivity - temperature cycles as a tool to study the thermal properties of the superionic glasses. Using σ - T cycles at various well controlled heating rates, we have calculated the activation energies of structural relaxation at T_g and crystallization. The study can be extended to calculate other thermal stability parameters such as enthalpy change (ΔH) and entropy change (ΔS) etc. by proper modification of conductivity set-up.

- These σ - T cycles can be used to understand the thermal properties of thin films as DSC is difficult for these thin film samples. Moreover, conductivity isotherm near crystallization can lead a better understanding of glasses.
- Since these glasses and glass-ceramics are highly ion conducting even at room temperature, it was not possible to study the relaxation dynamics by impedance spectroscopy (IS). The low temperature electrical transport (73-300K) using IS on glass-ceramic nano composites should be studied in future.
- In this study due to limitations of resources, we have performed XRD and SEM results on annealed samples to get a view of structural modifications with heat treatment. In-situ high temperature XRD and in-situ SEM measurements near the crystallization temperature can be especially useful in development of glass ceramic nano composites.

REFERENCES

- Adams S., Hariharan K., Maier J. (1995) Solid Stat. Ion. **75**, 193.
- Adams S., Hariharan K., Maier J. (1996) Solid Stat. Ion. **86-88**, 503
- Adnan S.B.R.S., Mohamed N.S., Norwati K.A. (2011) World Acad. Sci., Eng, Tech. **74**, 676.
- Agrawal R C, Verma M L, Gupta R K, Kumar R (2002) J. Phys. D: Appl. Phys. **35**, 810.
- Agrawal R.C., Kumar R., (1994) J. Phys. D: Appl. Phys. **27**, 2431.
- Agrawal R.C., Kumar R., Chandra A., (1996) Solid State Ionics, **84**, 51.
- Agrawal R.C., Mahipal Y.K., (2011) Int. J. Electrochem. Sci. **6**, 867.
- Armand M B, Chabango J M, and Duclot M (1978) Second International conference on solid electrolytes, St. Andrews, Scotland.
- Armand M B, Chabango J M, and Duclot M (1979) Fast ion transport in solids ed. Vashishta P, Mundy (1986) J N, North Holland, Amsterdam pp 131.
- Armand M, Deroo D, Pedone D,(1988) “*Solid State Ionic Devices*” (Singapore) 515.
- Arof A.K., (1994) J. Phys. III Appl. Phys. Mater. Sci. **4**, 849.
- Arof A.K., Seman K.C., Hashim A.N., Yahya R., Maah M.J., Radhakrishna S., (1995) Mater. Sci. Eng. **B31**, 249.
- Augis J A and Bennett J E (1978) J. Therm. Anal. **13**, 283
- Bannister D.J., Davies G.R., Ward I.M., Meintyre J.E. (1984) Polymers **25**, 1291.
- Bardley J.N., and Greenne P.D. (1967) Trans. Faraday Soc. **63**, 424.
- Baskaran N., Govindaraj G., Narayanasamy A., (1995) J. Power Sources, **55**, 153.
- Benasai P., Fontana A., Rodrigues P.A.M., (1991), Phys. Rev. B. **43**, 1756.
- Benz R (1975) Z. Phys. Chem. **95**, 25.
- Bhat M H, Chakravarthy B P, Ramakrishnan P A, Levasseur A, Rao K J (2000) Bull. Mater. Sci. **23**, 461.

- Bhattacharya S., Ghosh A. (2003) Solid State Ion. **161**, 61.
- Boukamp B.A. (2001) Solid State Ion. **143**, 47
- Boyce J.B., Hubberman (1979) Phys. Rep. **51**, 189.
- Brian E.F., Jones M.C., Lee S.H., Stoldt C.R., (2012) Appl. Phys. Lett. **100**, 103902.
- Chandra A., Agrawal R.C., Mahipal Y.K., (2009) J. Phys. D. Appl. Phys. **42**, 135107.
- Chitradevi R., Selvasekarapandian S., (2006) Ionics **6**, 203.
- Cho J., Kim G., Lim H., (1998) “*Batteries: conference on Appl. Adv.i*”, (Long Beach CA, USA) 381.
- Cullity B. D. (1978) Elements of X-ray Diffraction, 2nd Edition. Addison-Wesley Publishing Co. Menlo Park, CA.
- Dalvi A., Awasthi A. M., Bhardwaj S., (2008) Solid State ionics, in: “*Proceedings of 11th Assian Conference on Solid State Ionics*”, (Coimbatore, India) 555.
- Dalvi A., Awasthi A.M., Bharadwaj S., Shahi K. (2003) Mater. Sci. Engg. **B 103**, 162.
- Dalvi A., Shahi K., (2002) Solid State Ion. **148**, 431.
- Dalvi A., Shahi K., (2004) J. Non-Cryst Solids, **341**, 124.
- Damarawi G., (1999) J Phys: Conden Matter, **11**, 6385.
- Das S.S., Srivastava P.K., Singh N.P., Srivastava V., (2010), Indian J. Eng. Mater. Sci. **17**, 123.
- Deb B., Kabi S., Ghosh A., (2010) AIP Conf. Proceedings **1349**, 519.
- Delba G., Fontana A., Fornasini p., Mariotto G., Rocco F., (1983) Solid State Ionics, **9-10**, 597.
- Derrington C E, O’Keeffe M (1973) Nature Phys. Sci. **246**, 44.
- Deshpande V.K., (2009) “*IOP conf. proceedings: Mater. Sci. Eng.*”, **2**, 012011.
- Dworkin A.S., Bredig M.A. (1968) J. Phys. Chem. **72**, 1277.
- Echelmeyer T., Meyer H.W., Willen L.U. (2009) Chem. Mater. **21**, 2280.

- Faraday M. (1839) in “Experimental investigations in electricity” (Quaritch, London). 1340.
- Fenton D E, Parker J M, Wrigth P V(1973) Polymer, **14**, 589.
- Foltyn M., Wasiucionek M., Garbarczyk J., Nowinski J. L., (2005) Solid State Ion.**176**, 2137.
- Foltyn M., Wasiucionek M., Garbarczyk J.E., Nowinski J.L., Gierloyka S., Palosz B, (2008) Solid State Ionics, **179**, 38.
- Forland T., Krogh-Moe J., (1957) Acta. Chem. Scand. **11**, 565.
- Funke K. (1976) Prog. Solid. State. Chem. **11**, 345.
- Furusawa S., Miyaoka S., Ishibashi Y., (1991) J. Phys. Soc. Japan, **60**, 1666.
- Gao Y.X., Wang X.P., Wang W.G., Fang Q.F. (2010) Solid State Ionics **181**, 33.
- Garbarczyk J.E, Machowski P., Wasiucionek M., Tykarsi L., Bacewicz R., Alek Siejuk A. (2000) Solid State Ion. **136-137**, 1077.
- Geller S. (1967) Science **157**, 310.
- Geller S. (1977) in “ *Solid halogenide solid electrolytes*” (Verlag, Newyork,) 36.
- Gillan M J, (1986) J. Phys. C. Solid stat. Phys. **19**, 3391.
- Gillan M J and Richardson D D (1979) J. Phys. C: Solid State Phys. **12**, L61-5
- Goodman C.H.L., (1975) Nature, **257**, 370.
- Gorecki W, Andreani R, Berthier C, Armand M, Mail M, Roos J, Brinkmann D(1986) Solid Stat. Ion. **18-19**, 295.
- Grant R.J., Ingram M.D., Turner L.D.S., Vincent C.A. (1978) J. Phys. Chem. **82**, 2838.
- Greaves G.N., Catlow C.R.A., Vessal B., Charnock J., Henderson C.M.B., Zhu R., Qiao S., Wang Y., Gurman S.J., Walter S.H., (1990) Inst. Conf. Proc. Ser. **111**, 411.
- Gupta N., Dalvi A., (2010) J. Therm. Anal. Cal. **102**, 851.
- Gupta N., Dalvi A., Awasthi A. M., Bhardwaj S. (2008) Solid State ionics, in: “*Proceedings of 11th Assian Conference on Solid State Ionics*”, (Coimbatore, India), 550.
- Gupta N., Dalvi A., Awasthi A. M., Bhardwaj S., (2010) Solid State. Ion. **180**, 1607.

- Hariharan K., Sangamitra C, Sukeshini A.M., (1992) Solid State Ion. **53-56**, 1179.
- Hashmi S.A. and Chandra S. (1995) Mater. Sci. Eng. B **34**, 18.
- Hashmi S.A., (1996) “ *In extended abstracts: IInd National Conf. on Solid State Ionics*”, (Madras, India) C-15
- Hashmi S.A., Thakur A.K., Upadhyaya (1998) Eur. Polym. J., **34**, 1277.
- Hayashi A., Morishima H., Tadanaga K., Tatsumisago M., (2011) Solid State Ionics **192**, 126.
- Hayashi A., Tatsumisago M., Minami T., (2000) J. Non-Cryst solids, **276**, 27.
- Hruby A., Czech, (1972) J. Phys. **B22**, 1187.
- Hull S., (2004) Rep. Prog. Phys.,**67**, 1233.
- Indris S., Heitjans P., Roman H.E. and Bunde A., (2000) Phys. Rev. Lett, **84**, 2889.
- Ingram M.D., Mackenzie M.A, Muller W. and Torge M. (1988) Solid State Ion. **28-30**, 677.
- Jow T, Wagner Jr. J.B. (1979) J. Electrochem. Acta,**126**, **1963**
- Karmanov A., and Pelino M. (2001) J. Non-Cryst. Solids **290**, 173.
- Kaushik R., Hariharan K., (1988) Solid State Ionics **28-30**, 732.
- Kauzmann W, (1948) Chem. Rev. **43**, 2.
- Kissinger H., (1957) Anal. Chem.**29**, 1702.
- Krasowski K., Garbarczyk J. E., Wasiucionek M. (2000) Phys. Stat. Sol. (a) **181**, 157.
- Krasowski K., Garbarczyk J. E., Wasiucionek M. (2001) Phys. Stat. Sol. (a) **183**, 381.
- Krug J, Sieg L., (1952) Z. Naturforsch **70**, 369.
- Kumar A., Deka M, (2012) J. Solid State Electrochem. **16**, 35.
- Kumar B., Ro Drigues S.J., Scanlon L.G., (2001) **148**, A1191.
- Kumar B., Schaffer J.D., Nookala M., Scanlon L.G. Jr. (1994) J. Power Sources **47**, 63.
- Kumar S.R., Hariharan K., Dhanabalan M., Reddy K.V., (1996) Solid State Ionics **86-88**,

441.

Kunze D., (1973) "*Fast ion transport*" (North Holland, Amsterdam) 495.

Kushwaha S.S.S., Mishra J., (2005) Research Comm. **88**, 1159.

Lassegues J.C., (1992) "*Chemistry of Solid state materials*" (Cambridge) 311.

Liang C.C. (1973) J. Electrochem. Soc., **120**, 1289.

Lundberg M., Anderson S., (1964) Acta Chem. Scand. **18**, 817.

Magistris A., Chiodelli G., Vigano Campari G., (1976) Z. Natur- forsch. **31a**, 974.

Magistris A., Chiodelli G. and Duclot M. J., (1983) Solid State Ion. **9/10**, 611.

Magistris A., Ferloni P., Mustarelli P., Restelli M., Chiodelli G., (1994) "*Solid State Ionic Materials*" 361.

Magistris A., Chiodelli G., Schiraldi A. (1979) Electrochem. Acta, **24**, 203.

Maier J., (1986) Solid State Ionics **18-19**, 1141.

Malugani J. P. and Robert G., (1979) Mater. Res. Bull. **14**, 1075.

Malguni J.P., Robert G. (1980) Solid State Ionics **1**, 519.

Matsubara T., (1975) J. Phys. Soc. Japan **38**, 1076.

Matusita K., Sakka S., Matsui Y. (1975) J. Mater. Sci. **10**, 961.

Matusita K., Sakka S., (1979) Phys. Chem. Glasses **20**, 81.

Matusita K, Sakka S., (1980) J. Non-Cryst. Solids **38-39**, 741.

Minami T., Nambu H., Tanaka M., (1977) J. Am. Ceram. Soc. **60**, 283.

Minami T., and Tanaka M., (1980) J. Non-Cryst. Solids **38-39**, 289.

Minami T., (1987) J. Non-Cryst Sol. **95-96**, 107.

Minami T., Hayashi A., Tatsumisago M., (2006) Solid State Ionics, **177**, 2715.

Minami T., Shimizu T., Tanaka M. (1983) Sol. Stat. Ion. **9-10**, 577.

Minami T., Takuma Y., Tanaka M. (1988) J. Electrochem. Soc., **124**, 1659.

- Minami T., (1985) *J. Non-Cryst. Solids* **73**, 273.
- Mohan V.M., Raja V, Sharma A.K. and Rao V.V.R.N. (2006) *Ionics*,**12**, 219.
- Moricova E., Jona E., Plsko A., (2010) *J. Therm. Anal. Calor.*, **100**, 817.
- Morimoto H., Yamashita H., Tatsumisago M., Minami T. (1999) *J. Am. Ceram. Soc.* **82**, 1352.
- Moynihan T., Easteal A. J., Wilder J., (1974) *J. Phys. Chem.***78**, 2673.
- Mroczkowska M., Czeppe T., Nowinski J. L., Garbarczyk J. E., Wasiucioneck M. (2008) *Solid State Ionics* **179**, 202.
- Mundy J.N., Jin G.L. (1986) *MRS Proceedings*, **61**, 467.
- Murugesan S, Suthanthiraraj S.A., Maruthamuthu P., (2002) *Solid State Ion* **154-155**, 621.
- Mustarelli P., Quartarone E, Tomasi C, Magistris A., (1996) *Solid State Ionics* **86-88**, 347.
- Nagasubramanian G., Attia A.J., Halpert G., Peled E., (1993) *ibid* **67**, 51.
- Nakayama M., Watanabe K., Ikuta H., Uchimoto Y., Wakihara M., (2003) *Solid State Ion.* **164**, 35.
- Nowinski J.L., Kurek P, Jacubowski W., (1989) *Solid State Ionics* **36**, 213.
- Nowinski J.L., Mroczkowska M., Garbarczyk J.E., Wasiucioneck M., (2006) *Mater. Sci. – Poland*, **24**, 161.
- Nowinski J.L., Vadillo P.P., Garbarczyk J.E., Wasiucioneck M., Zukowska G.Z., Gierlotta S., (2008) *Rev. Adv. Mater. Sci.* **18**, 725.
- O'keeffe M. and Hyde B.G. (1976) *Phil. Mag.* **33**, 219.
- Owens B.B. and Argue G.R. (1967) *Science* **157**, 308.
- Ozawa T, (1970) *J Therm Anal*, **2**, 301.
- Padmasree K.P., Kanchan D.K., Panchal H.R., Hariharan K., Okram T., (2006) *J. Power Sources*, **159**, 742.
- Padmasree K.P., Kanchan D.K. (2009) *J. Solid Stat. Electrochem.* **12**, 1561.

- Pappenfus, T. M., Henderson, W. A., Owens, B. B., Mann, K. R., and Smyrl, W. H. (2004) *Solid Stat. Ionics*. **171**, 41.
- Patro L.N., Hariharan K., (2009) *Mater. Sci. Eng. B*. **162**, 173.
- Phillips J.C. (1981) *Phys. Today* **35**, 27.
- Phillips J.C. (1981) *Phys. Rev. B* **24**, 1744.
- Polu A.R., Kumar R., (2011) *Bull. Mater. Sci.* **34**, 1063.
- Prasad P. S. S., Rani A. N. D., Radhakrishna S. (1990) *Materials Chemistry and Physics* **25**, 487.
- Przyluski J., Florianczyk Z., Such K., Wycislik H. and Wieczorek W. (1989) *Synth. Metals* **35**, 241.
- Raghavan P., Zhao X., Kim J.K., Manuel J., Chauhan G.S., Ahun J.H., Nah C., (2008) *Electrochimica Acta*, **54**, 228.
- Rahlf's P. (1936) *Z. Physik. Chem.* **B 31**, 157.
- Rajendran S., Prabhu R.M., (2010) *J. Appl. Electrochem.*, **40**, 327.
- Rao K.J., Rao C.N.R., (1982) *Mate. Res. Bull.* **17**, 1337.
- Reynoso V.C.S., Yukimitu K, Nagami T., Carvalho C.L. Moraes J.C.S. Auaujo E.B., (2003) *J. Phys. Chem. Sol.*, **64**, 27.
- Rocca F., Delba G., Fornasini P., Tomasi A., (1992) *Solid State Ionics*, **53-56**, 1253.
- Rolling B., Ingram M.D., Lange M., Funke K. (1997) *Phys. Rev. B* **56**, 21.
- Rolling B., Ingram M.D., (2000) *J. Non-Cryst. Sol.* **265**, 113.
- Rouse G.B., Miller P.J., Risen W.M., (1978) *J. Non-Cryst. Sol.* **28**, 193.
- Saito T., Tatsunisago M., Minami T., (1993) *Solid State Ion.* **61**, 285.
- Sakuma T., Jida K., Honma K., Okazaki H. (1977) *J. Phys. Soc. Japan* **43**, 538.
- Sekhon S.S., Singh G., Agnihotry S.A., Chandra S., (1995), *Solid Stat. Ion.* **80**, 37.
- Sekhon S. S., Chandra S. (1999) *J. Mater. Sci. Lett.* **18**, 635.

- Sekhon S.S., Sandhar G.S., Agnihotri S.A., Chandra S., (1996) Bull. Electrochem. **12**,415.
- Selvaraj U, Rao K.J., (1984) Spectrochem Acta **A**, **40**, 1081.
- Shahi K. Wagner J.B. Jr. (1981) *ibid* **128**, 6.
- Shahi K., Wagner J.B. Jr., (1982) J. Solid State Chem, **42**, 107.
- Shaju K.M., Chandra S., (1995) J. Mater. Sci. **30**, 3457.
- Sharma P., Kanchan D.K., Godaliya N., Kandpal M., Jayswal M., (2011) New J. Glass and Ceramics, **1**, 125.
- Shastry M.C.R., Rao K.J., (1992) Solid State Ionics **51**, 311.
- Sinclair D.C., West A.R., (1989) AIP: J. Applied Phys **66**, 3850.
- J., Wu F., Chen S., Zhang C., (2006) J. Power Sources, **152**, 592.
- Shimizu Y., Azuma Y., Michishita S. (1997) J. Mater. Chem. **7**, 1487.
- Shukla N. Thakur A.K. (2009) Ionics **15**, 357.
- Sinha M., Maitra M., Mal D., Midya T.R., Tarafdar S., De U, Chaudhuri S.K., Das D., (2008) Ionics **14**, 323.
- Song X., Jia M., Chen R, (2002) J. Mater. Proc. Tech. **120**, 21.
- Souquet J. L., (1981) Ann. Rev. Mater. Sci. **11**, 211.
- Sreekanth T., Reddy M.J., Ramalingaiah S., Subba rao U.V. (1999) J. Power Sources **79**, 105.
- Stroock L.W. (1934) Z. Phys. Chem. **B 25**, 411.
- Stroock L.W. (1936) Z. Phys. Chem. **B 31**, 132
- Suresh Kumar R., Hariharan K., Dhanabalan M., Reddy K.V. (1996) Solid State Ion. **86-88**, 441.
- Suthanthiraraj S. A., Murugesan S., Maruthamuthu P., (2000) Solid Stat. Ion. **130**, 299.
- Suthanthiraraj A., Kumar S., Paul J., (2010) Ionics **16**, 145.

- Suthanthiraraj S. A., Murugesan S., Maruthamuthu P., (2002) *Mat. Res. Bull.* **37**, 2145.
- Swenson J., Börjesson L., McGreevy R.L., Howells W.S. (1997) *Phy. Rev. B, Conden. Matt.* **234**, 231.
- Tachez M., Mercier R., Malguni J.P., (1986) *Solid State Ionics* **18-19**, 372.
- Takahashi T., and Yamamoto O. (1964) *Denki Kagaku* **32**, 610.
- Takahashi T., and Yamamoto O. (1966) *Electrochim. Acta* **11**, 779.
- Taniguchi A., Tatsumisago M., Minami T., (1995) *J. Am. Ceram. Soc.* **78**, 460.
- Tarafdar S., De S.K. Manna S., De U, Nanda P. (2010) *J. Physics* **74**, 271.
- Tatsumisago M., Shinkuma Y., and Minami T., (1991) *Lett. Nat.* **354**, 217.
- Tatsumisago M., Saito T., Minami T. (2001) *Chem. Lett.* **30**, 790.
- Tatsumisago M., Shinkuma Y., Minami T. (1991) *Nature* **354**, 217.
- Tubandt C. (1932) *Handbuch Der Experimental Physik* **12**, 383.
- Tubandt C. (1921) *Z. Anorg. Allgem. Chem.* **115**, 105.
- Tuller H. L., Button D. P., Uhlmann D. R., (1980) *J. Non-Cryst Solids* **40**, 93.
- Uvarov N.F., Shrivastava O.P., Hairetdinov E.F., (1989) *Solid Stat. Ion.* **36**, 39.
- Uvarov N.F. Bokhonov E.F., Isupov V.P. and Hairetdinov E.F., (1994) *Solid Stat. Ion.* **74**, 15.
- Vaidyanathan B., Ganguli M., Rao K.J. (1994) *J. Solid State Chem.* **113**, 448.
- Venkateswarlu M., Satyanarayan N., (1998) *J. Power Sources* **73**, 257.
- Watanabe M., Togo M., Sanui K., Ogata N., Kobayashi T., Ohtaki Z. (1984) *Macromolecules* **17**, 2908.
- Whittingham M.S., Huggins R.A., (1972) *“Fast ion transport in solids”* (North Holland, Amsterdam) 165.
- Willis B.T.M. (1965) *Acta Cryst.* **18**, 75.

Woo H.J., Majid S.R., Arof A.K., (2011) *Solid State ionics* **14**, 199.

Wu X, Wen Z., Xu X., Wang X., Lin J., (2009) *J. Nucl. Mater.*, **85**, 222.

Yao F.Y., Kummer J.T., (1967) *Inorg. Nucl. Chem.* **29**, 2453.

Yun Z., Wang C. and Jian Y. (1987) in *Extended Abstracts:Sixth International Conference on Solid State Ionics*, Garmisch-Partenkirchen, Germany, 6–11 Sept. p. 357.

Zachariasen W.H., (1932) *J. Chem. Soc.* **54**, 3841.

Zhang X.W., Wang C., Appleby A.J., Little F.E., (2002) *J. Power Sources* **112**, 209.

LIST OF PUBLICATIONS

1. **N. Gupta**, A. Dalvi, "Electrical, Structural and Thermal characterization of Cu_2O substituted $\text{AgI}-(\text{Cu}_2\text{O})_x(\text{Ag}_2\text{O})_{1-x}-\text{V}_2\text{O}_5$ glassy superionic system" (2012) (accepted) *Solid State Ionics*.
2. **N. Gupta**, A. Dalvi, S. Bharadwaj, A.M. Awasthi, "Crystallization and glass transition kinetics in Cu^+ ion substituted $\text{Cu}_x\text{Ag}_{1-x}\text{I}-\text{Ag}_2\text{O}-\text{V}_2\text{O}_5$ " *J. Non-Cryst. Sol.*, **357**:1811-1815, 2011.
3. **N. Gupta**, A. Dalvi, "Effect of mixed glass formers on the crystallization kinetics in $\text{AgI}-\text{Ag}_2\text{O}-\text{V}_2\text{O}_5-\text{MoO}_3$ glassy superionic system" *Ionics* **17**: 315-322, 2011.
4. **N. Gupta**, A. Dalvi, "Thermal stability and crystallization kinetics in superionic glasses using electrical conductivity- temperature cycles" *J. Therm Anal Calorim* **102**:851-855, 2010.
5. **N. Gupta**, A. Dalvi, S. Bharadwaj, A.M. Awasthi, "Electrical transport and crystallization in Cu^+ ion substituted $\text{AgI}-\text{Ag}_2\text{O}-\text{V}_2\text{O}_5$ glassy superionic system" *Sol. Stat. Ion.***180**: 1607-1612, 2010.
6. **N. Gupta**, A. Dalvi, Effect of Cu_2O substitution on glass transition and crystallization kinetics in $50\text{AgI}-33.33 [(\text{Cu}_2\text{O})_x-(\text{Ag}_2\text{O})_{1-x}]-16.67\text{V}_2\text{O}_5$ glassy solid electrolytes (Communicated in JTAC)

LIST OF PRESENTATIONS

International conferences

1. **Neha Gupta**, A Dalvi, A M Awasthi, S Bharadwaj, "*Synthesis of glassy superionic composite by microwave treatment*" International conference on condensed matter Physics, Jaipur Nov 25-28, 2007"
2. **Neha Gupta**, A Dalvi, S Bhardwaj, A M Awasthi and N P Lalla "*Characterization of glassy superionic composites prepared by microwave treatment*" published in Solid State Ionics Ed B V R Chowdari et al (2008) P355-361 proceedings of 11th Asian conference on solid state ionics.
3. **Neha Gupta**, A. Dalvi. "*Effect of Cu₂O substitution on glass transition and crystallization kinetics in 50AgI-33.33 [(Cu₂O)_x-(Ag₂O)_{1-x}]-16.67V₂O₅ glassy solid electrolyte*" International Conference on Materials for advanced technologies, Singapore June 26- July 1, 2011.

National conferences

1. **Neha Gupta**, Munesh Rathore, Sukriti kumara, Manupriya Veerman, Anshuman Dalvi, "Electrical transport and impedance spectroscopy investigations in PEO: MgCl₂ solid polymer electrolyte" presented in National conference on condensed matter physics 23-24 February 2012, Birla Institute of Technology and Science, Pilani.
2. **Neha Gupta**, Anshuman Dalvi, Barkha Awasthi, D Deva, "*Electrical Transport and structural investigations in Cu₂O substituted AgI-Ag₂O-V₂O₅ glass ceramic nanocomposites*" presented in DAE solid state Physics Symposium, 19-23 December 2011, SRM university, Chennai.
3. **Neha Gupta**, Anshuman Dalvi, "*Characterization of AgI and CuI based glass ceramic nanocomposites*" (2011) presented in NCSSI 15-17 December 2011, Jaypee

University, Noida.

4. **Neha Gupta**, Anshuman Dalvi, D Phase, A M Awasthi “*Electrical transport in superionic thin films deposited by pulsed laser deposition*” presented in DAE- solid state Physics Symposium 2010 AIP Conf. Proc. 1349, 535-536 (2011).
5. **Neha Gupta**, Munesh Rathore and A Dalvi “*Electrical and electrochemical characterization of PEO-Ag₂SO₄ composite polymer electrolytes*” presented in DAE solid state Physics Symposium 2010 AIP Conf. Proc. 1349, 174-175 (2011).
6. **Neha Gupta** and Anshuman Dalvi “*Thermal investigations on superionic glasses using electrical conductivity temperature cycles*” DAE solid state Physics Symposium M S University Baroda December 11-15 2009 published in Solid State Physics 54 (2009) P 511-512.
7. **Neha Gupta** and Anshuman Dalvi “*Investigations of thermal properties of AgI-Ag₂O-MoO₃-V₂O₅ superionic glasses using electrical conductivity – temperature cycles*”. 8th National Conference on solid state ionics Sagar central University December 7-10 2009.
8. **Neha Gupta**, Srikanth Y and Anshuman Dalvi “*Preparation of, mixed cation effect in KI-AgI-Ag₂O-V₂O₅ superionic glasses*” presented by N Gupta in National symposium for Materials Research Scholar at IIT Bombay May 7-8, 2009.

BIOGRAPHY OF THE SUPERVISOR

Dr. Anshuman Dalvi obtained his doctoral degree at Indian Institute of Technology, Kanpur under the supervision of Professor K. Shahi in the field of solid state ionics. Subsequently he did his postdoctoral work under the guidance of Professor S. C. Agarwal on some aspects of amorphous semiconductors.

Dr. Anshuman Dalvi joined the Physics department BITS, Pilani in June 2004 as a lecturer and since January 2006 working as an Assistant Professor. He is an experimental solid state physicist-cum-material scientist, whose chief interest lies in Superionic Conductors and their applications in electrochemical devices, especially high density batteries. Currently he is working on issues like; thermal stability of superionic glasses, Lithium ion conducting glass-ceramic nanocomposites, ionic liquid-glass composites and Mg^{++} ion conducting polymers and mechanochemical synthesis. He has executed one DST project successfully, developed materials physics laboratory in Pilani, and published ~ 30 papers of which eighteen papers in international journals. He is executive member of Indian Solid State Ionics Society and a regular reviewer of reputed international journals like Solid State Ionics, International Journal of Ionics and Materials Science and Engineering B.

BIOGRAPHY OF THE CANDIDATE

Ms. Neha Gupta is a full time research scholar in Department of Physics, BITS, Pilani since August 2006. She holds B.Sc. (Physics, Chemistry and Mathematics) from Kalidas College, Ujjain affiliated with Vikram University Ujjain (M.P.), in the year 2004 and her Masters degree in Physics with specialization in Materials science which she graduated in the year 2006 from Devi Ahilya Vishwavidyalaya, Indore (M.P.). Later she got her M.Phil Applied from Devi Ahilya Vishwavidyalaya, Indore (M.P.) in 2007. Her research interests are Superionic glassy materials for solid state button type cells. She is currently pursuing Ph.D. from BITS, Pilani in Experimental physics as Thermal stability investigations on Ag^+ ion conducting superionic glasses and glass-ceramic nano composites. She published five papers in international journals and presents her work in twelve national or international conferences in India or abroad.